

Exploring Plasmonic Refractive Index Nanosensors with Different Applications

by

Infiter Tathfif (**160021158**)
Kazi Sharmeen Rashid (**160021044**)
Ahmad Azuad Yaseer (**160021036**)

**BACHELOR OF SCIENCE
IN
ELECTRICAL AND ELECTRONIC ENGINEERING**



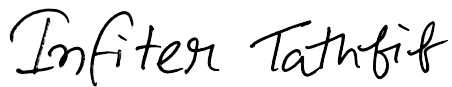
Department of Electrical and Electronic Engineering
Islamic University of Technology (IUT)
Board Bazar, Gazipur-1704, Bangladesh.
June, 2021.

Declaration of Authorship

We, Infiter Tathfif (**160021158**), Kazi Sharmeen Rashid (**160021044**) and Ahmad Azuad Yaseer (**160021036**), declare that this thesis titled, '**Exploring Plasmonic Refractive Index Nanosensors with Different Applications**' and the works presented in it are our own. We confirm that:

- This work has been done for the partial fulfillment of the Bachelor of Science in Electrical and Electronic Engineering degree at this university.
- Any part of this thesis has not been submitted anywhere else for obtaining any degree.
- Where we have consulted the published work of others, we have always clearly attributed the sources.

Submitted by:



Infiter Tathfif (**160021158**)



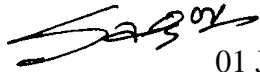
Kazi Sharmeen Rashid (**160021044**)



Ahmad Azuad Yaseer (**160021036**)

Exploring Plasmonic Refractive Index Nanosensors with Different Applications

Approved by:



01 June 2021

Dr. Rakibul Hasan Sagor (Supervisor)
Associate Professor,
Electrical and Electronic Engineering Department,
Islamic University of Technology (IUT), Gazipur.

Table of Contents

Declaration of Authorship	i
List of Figures	vi
List of Tables	x
List of Abbreviations	xi
List of Symbols	xii
Acknowledgment	xiii
Abstract	xiv
1 Introduction and Background	1
1.1 Surface Plasmon Polariton	1
1.2 Plasmonic Devices	2
1.2.1 Plasmonic Splitters	2
1.2.2 Plasmonic Couplers	3
1.2.3 Plasmonic Filters	3
1.2.4 Plasmonic Sensors	4
1.3 Plasmonic Waveguides	5
1.3.1 Metal-Insulator-Metal (MIM) Waveguide	5
1.3.2 Insulator-Metal-Insulator (IMI) Waveguide	6
1.3.3 Hybrid Waveguide	7
1.4 Literature Review	8
1.5 Thesis Objectives	13
1.6 Thesis Layout	13
2 Wave Theory	15
2.1 Maxwell's and Wave Equations	15
2.1.1 Maxwell's Equations	15
2.1.2 Constitutive Equation	16

2.1.3	Generalized Constitutive Equations	17
2.1.4	Wave Equation	17
2.2	Simulation Modeling	18
2.2.1	Finite-Difference Time Domain (FDTD)	18
2.2.2	Finite Integration Technique (FIT)	22
2.2.3	Finite Element Method (FEM)	23
3	Plasmonic Materials	30
3.1	Refractive Index and Complex Permittivity	30
3.2	Material Modeling	31
3.2.1	Drude Model	31
3.2.2	Lorentz Model	31
3.2.3	Lorentz-Drude Model	31
3.3	Ag Modeling	32
3.4	Au modeling	33
3.5	Cu Modeling	34
3.6	Al Modeling	35
3.7	Comparison among Plasmonic Materials	36
4	Performance Metrics of an RI Sensor	37
4.1	Ring and Cavity Resonator	37
4.2	Concentric Double-Ring Resonator (CDRR)	39
4.3	Performance Metrics	40
4.3.1	Sensitivity (S)	40
4.3.2	Figure of Merit (FOM)	41
4.3.3	Quality-factor (Q -factor)	42
4.3.4	Detection Limit (DL)	43
4.4	Re-Simulation with COMSOL Multiphysics	43
4.4.1	Chen <i>et al.</i>	43
4.4.2	Zhang <i>et al.</i>	47
4.4.3	Butt <i>et al.</i>	49
5	Modeling, Optimization and Numerical Analysis of the Proposed Sensors	51
5.1	Sensor Design with CDRR	51
5.1.1	Sensor Layout and Theoretical Analysis	51
5.1.2	Sensing Technique and Performance Criteria of an RI Sensor	52
5.1.3	Initial Simulation Results and Discussion	53
5.1.4	Maximizing Sensitivity through Optimization	55

5.1.5	Fabrication	58
5.1.6	Detection of Cancer Cells	59
5.1.7	Chemical Sensing	60
5.1.8	Bandpass filter	61
5.2	Sensor Design with Multiple Rings	62
5.2.1	Sensor Geometry and Theoretical Background	62
5.2.2	Simulation Results and Discussion	63
5.2.3	Fabrication	66
5.2.4	Fabrication Error Tolerance	67
5.2.5	Detection of Biomolecules	68
5.2.6	DNA Hybridization	69
5.3	Sensor Design with Rectangular Cavities	70
5.3.1	Schematic Design and Methodological Study	70
5.3.2	Sensing Procedure	72
5.3.3	Result Analysis for Initial Framework	73
5.3.4	Optimization of Parameter $D2$ and $D1$	74
5.3.5	Fabrication	78
6	Conclusion and Future Work	79
6.1	Conclusion	79
6.2	Future Work	81
	References	82
	List of Publications	95

List of Figures

1.1	a) Evolution of device technologies (adapted from [1]). b) Formation and propagation of Surface Plasmon Polaritons (SPPs) (redrawn from [2]).	1
1.2	Plasmonic splitter proposed by [7].	2
1.3	Plasmonic coupler proposed by [11].	3
1.4	Plasmonic filter proposed by [19].	4
1.5	Plasmonic sensor proposed by [24].	4
1.6	(a) MIM schematic. (b) Dispersion plot of MIM structure, adapted from [28].	5
1.7	a) Antisymmetric and b) symmetric propagation modes [29].	6
1.8	IMI schematic.	6
1.9	IMI field profile [31].	7
1.10	a) Hybrid waveguide proposed by [32]. b) Hybrid mode profile.	7
1.11	Some recent plasmonic sensors by (a) Yang <i>et al.</i> [43], (b) Xie <i>et al.</i> [45], (c) Wang <i>et al.</i> [46], (d) Zhang <i>et al.</i> [47], (e) Zhang <i>et al.</i> [53], and (f) Butt <i>et al.</i> [52].	9
2.1	Yee's spatial grid [84].	19
2.2	Temporal scheme of FDTD [85].	20
2.3	Uniform 1D grid [89].	22
2.4	Finite element discretization.	24
2.5	Single triangular element.	25
3.1	a) Real part of complex permittivity, b) Imaginary part of complex permittivity, c) Real part of complex refractive index, and d) Imaginary part of complex refractive index for Ag.	32
3.2	a) Real part of complex permittivity, b) Imaginary part of complex permittivity, c) Real part of complex refractive index, and d) Imaginary part of complex refractive index for Au.	33
3.3	a) Real part of complex permittivity, b) Imaginary part of complex permittivity, c) Real part of complex refractive index, and d) Imaginary part of complex refractive index for Cu.	34

3.4	a) Real part of complex permittivity, b) Imaginary part of complex permittivity, c) Real part of complex refractive index, and d) Imaginary part of complex refractive index for Al.	35
3.5	Performance of Au and Cu in the wavelength range of 600 nm to 750 nm [93].	36
4.1	Schematic of a plasmonic waveguide coupled with a ring structure. . .	37
4.2	Schematic of a plasmonic waveguide coupled with a cavity resonator.	39
4.3	Schematic of a plasmonic waveguide coupled with a concentric double-ring resonator.	39
4.4	Effect of rings on CDRR structure [97].	40
4.5	Sensitivity calculation.	40
4.6	Figure of Merit calculation.	41
4.7	Q-factor calculation.	42
4.8	(a) High Q -factor and (b) low Q -factor representation.	42
4.9	Schematic of Chen <i>et al.</i> [101]	43
4.10	Block diagram representation of the simulation procedure.	44
4.11	(a) 2D view. (b) Mesh view.	45
4.12	(a) Results by Chen <i>et al.</i> [101]. (b) Re-simulated results.	45
4.13	$ H_z ^2$ with and without the groove at the resonance wavelength $\lambda = 1392$ nm (a) – (b) by Chen <i>et al.</i> [101] and (c) – (d) re-simulated work.	46
4.14	Transmission profile (a) by Chen <i>et al.</i> [101], (b) re-simulated work. .	46
4.15	Schematic of Zhang <i>et al.</i> [102]	47
4.16	(a) 2D view. (b) Mesh view.	47
4.17	Forward and backward transmission profiles for $d = 450$ nm.	48
4.18	H_z field (a) by Zhang <i>et al.</i> [102] and (b) resimulation.	48
4.19	Schematic diagram of plasmonic filter proposed by Butt <i>et al.</i> [52] . .	49
4.20	(a) 2D view of the resimulated filter. (b) Triangular mesh view of the resimulated filter.	50
4.21	E -field confinement in MIM waveguide μ -ring cavities (a) depicted by Butt <i>et al.</i> [52] and (b) for the resimulated sensor.	50
5.1	Two-dimensional model of the proposed sensor.	51
5.2	a) Initial transmittance spectrum. b) Formation of Fano peaks.	53
5.3	$ H_z ^2$ field distribution for the presented MIM sensor.	54
5.4	Transmittance spectra for variation of refractive index, η	54
5.5	a) Transmittance spectra for varying GI . b) – e) Resonant wavelength vs. Refractive index graphs for different values of GI	55

5.6	a) – d) Transmittance spectra for varying R_{in} . e) – h) Resonant wavelength vs. Refractive index graphs for various values of R_{in}	56
5.7	a) Transmittance spectra for varying R_{out} . b) Resonant wavelength vs. R_{out} graph. c) – f) Resonant wavelength vs. Refractive index graphs for different values of R_{out}	56
5.8	a) Transmittance spectra for varying $D2$. b) – e) Resonant wavelength vs. Refractive index graphs for different values of $D2$	57
5.9	a) Transmittance spectra for optimized structural parameters. b) FOM^* of the proposed sensor.	58
5.10	Fabrication of the suggested sensor using nanoimprint lithography. . .	59
5.11	a) Transmittance spectra for cancer detection. b) Resonant wavelength vs. Refractive index graphs for different cancer cells.	60
5.12	a) Transmittance spectra for chemical sensing. b) Resonant wavelength vs. Refractive index graphs for different solutions.	61
5.13	Schematic diagram of the proposed nanosensor.	62
5.14	(a) Transmission spectrum at $n = 1.00$. (b) The E-field distribution at the corresponding resonant wavelength.	63
5.15	(a) Transmission spectra at varying refractive index (n). (b) Relationship between resonant wavelength and refractive index.	64
5.16	(a) Transmission spectra of the waveguide with changing width of the waveguide (w). (b) Transmission spectra at varying coupling distance (g).	64
5.17	(a) Transmission spectra of the waveguide with changing outer radius (r). (b) Relationship between resonant wavelength and outer radius of the rings.	65
5.18	(a) Transmission spectra of the waveguide with changing width of the ring (w_2). (b) Relationship between resonant wavelength and width of the rings.	65
5.19	(a) Transmittance profile of the structure with final parameters. (b) Relationship between resonant wavelength and refractive index. . . .	66
5.20	NIL fabrication process of the proposed structure.	67
5.21	Proposed nanosensor with slits on the rings.	67
5.22	Transmission spectra at slit width of (a) 5 nm and (b) 10 nm.	67
5.23	Transmission spectra for different blood components.	68
5.24	Transmission spectra for DNA hybridization.	69
5.25	Two-dimensional schematic design of the proposed sensor.	70
5.26	E-field confinement in rectangular cavities of length (a) L_1 , (b) L_2 , (c) L_3 , (d) L_4 , (e) L_5 , and (f) L_6 at initial parameters.	72

5.27	Transmittance spectrum of the proposed sensor at initial parameters. . .	73
5.28	(a) Transmittance vs. wavelength curve for different values of refractive index, η . (b) Resonance wavelength vs. refractive index curve for initial framework.	73
5.29	(a) Transmittance vs. wavelength curve for different values of $D2$. Resonance wavelength vs. refractive index curve for (b) $D2 = 300$ nm. (c) $D2 = 250$ nm, and (d) $D2 = 200$ nm.	74
5.30	(a) Transmittance vs. wavelength curve for different values of $D1$. Resonance wavelength vs. refractive index curve for (b) $D1 = 40$ nm and (c) $D1 = 50$ nm.	75
5.31	Transmittance spectrum of the proposed sensor at optimized parameters.	76
5.32	E -field confinement in rectangular cavities of length (a) L_1 , (b) L_2 , (c) L_3 , (d) L_4 , (e) L_5 , and (f) L_6 at optimized parameters.	76
5.33	FOM* at optimized parameters.	77
5.34	Fabrication technique of the proposed sensor.	78

List of Tables

1.1	Comparison between recent RI sensors.	10
3.1	Lorentz-Drude Parameters for Ag [92].	32
3.2	Lorentz-Drude Parameters for Au [92].	33
3.3	Lorentz-Drude Parameters for Cu [92].	34
3.4	Lorentz-Drude Parameters for Al [92].	35
4.1	Geometric parameters of the structure [101].	44
4.2	Geometric parameters of the structure [102].	47
4.3	Geometric parameters of the structure [52].	49
5.1	Preliminary 2D modeling parameters.	52
5.2	The synopsis of the optimization process.	58
5.3	Performance of the proposed optimized sensor as a cancer cell detector [107], [108], [109].	60
5.4	Performance of the proposed optimized device as a chemical sensor [110].	61
5.5	Initial simulation parameters.	62
5.6	The most sensitive structural parameters of the proposed sensor.	66
5.7	Sensitivity analysis for slit width b	68
5.8	Sensitivity analysis for different blood components.	69
5.9	Values of each schematic parameter of the proposed structure.	70
5.10	The wavelength range for six visible basic colors.	73
5.11	Summary of the optimization process.	77
6.1	Performance comparison of the proposed works with recent literature.	80

List of Abbreviations

SPP	Surface Plasmon Polariton
EM	Electromagnetic
TM	Transverse-Magnetic
TE	Transverse-Electric
PBS	Polarization Beam Splitter
MDM	Metal-Dielectric-Metal
WDM	Wavelength Division Multiplexing
RI	Refractive Index
MIM	Metal-Insulator-Metal
IMI	Insulator-Metal-Insulator
LR-SPP	Long-Range SPP
FOM	Figure of Merit
FEM	Finite Element Method
FDTD	Finite-Difference Time Domain
FIT	Finite Integration Technique
ABC	Absorbing Boundary Condition
SBC	Scattering Boundary Condition
PML	Perfectly Matched Layer
PDE	Partial Differential Equation
MoM	Method of Moments
CDRR	Concentric Double-Ring Resonator
FWHM	Full Width at Half Maximum
Q-factor	Quality Factor
DL	Detection Limit
MUS	Material Under Sensing
NIL	Nanoimprint Lithography
EBL	Electron Beam Lithography
FIB	Focused Ion Beam
NIR	Near-Infrared Region
OSA	Optical Spectrum Analyzer

List of Symbols

k_0	Wave vector
ω	Angular frequency
c	Speed of light
ε_d	Relative permittivity of dielectric
ε_m	Relative permittivity of metal
η	Refractive index
λ	Wavelength
μ_0	Absolute permeability
ε_0	Absolute permittivity
P	Polarization
χ_e	Electric susceptibility
$\hbar\omega_p$	Plasma frequency
Γ_0	Collision frequency
γ_i	Oscillator strength
Γ_i	Damping frequency
ω_i	Resonant frequency
η_{eff}	Effective refractive index
β	Propagation constant

Acknowledgment

At first, we would like to express our gratitude to Allah (SWT), the most merciful and compassionate.

We would like to offer our heartiest gratitude to our thesis supervisor Dr. Rakibul Hasan Sagor, Associate professor, Department of Electrical and Electronic Engineering, Islamic University of Technology (IUT), for his invaluable advice, support, and guidelines throughout our studies and research work. He created ample research opportunities and motivated us to explore out of the box. We are thankful for all his lessons and knowledge.

We would also like to thank Md. Farhad Hassan, Lecturer, Department of Electrical and Electronic Engineering, Islamic University of Technology (IUT), for his continuous support and teachings throughout our research journey. We are grateful to him for letting us participate in his projects, which helped us gain knowledge about the basics of researching.

We are also grateful to all the faculty members of the Electrical and Electronic Engineering Department, Islamic University of Technology (IUT), for their inspiration and support.

Finally, we are thankful to our families for their continuous mental support during the entire writing of this thesis throughout the pandemic.

Infiter Tathfif
Kazi Sharmeen Rashid
Ahmad Azuad Yaseer
June, 2021

Abstract

In this thesis, three high-yielding plasmonic refractive index sensors based on Metal-Insulator-Metal waveguide are proposed to satisfy the current sensing demands in different sectors, for example, medical, forensic, and industrial. The proposed works employ a straight waveguide and different resonators, such as ring resonator, concentric double-ring resonator, and cavity resonator in the two-dimensional form to expedite the simulations. COMSOL Multiphysics is chosen as the wave-solver, which inherently deploys the Finite Element Method. The re-simulations of existing structures corroborate the computational accuracy of COMSOL Multiphysics. Furthermore, all three designed sensors fabricated through nanoimprint lithography technique exhibit linear correlation with the refractive index and the resonant wavelength. This linear relationship is exploited to sense the unknown materials. Moreover, the structural parameters of the plasmonic sensors are sensitive to variations. Thus, the suggested sensors undergo extensive simulations and optimization processes to maximize their performance. The proposed first work with the concentric double-ring resonator exhibit an initial sensitivity of 1804.23 nm/RIU. A maximum sensitivity of 3522.44 nm/RIU is obtained after optimization. Additionally, the optimized FOM , FOM^* , Q -factor, detection limit of the illustrated sensor with CDRR are 80.07, 0.73×10^6 , 83.65, 2.37×10^{-7} RIU, respectively. This proposed work is deployed to detect cancerous cells, sense chemical concentrations, perform plasmonic filtering, and display superior performance in all three cases. The proposed second work with ring resonator initially displays a sensitivity of 2763.75 nm/RIU. After extensive simulations, a final sensitivity of 3573.3 nm/RIU is obtained. The tolerance capability of the structure is studied by introducing nano slits on the rings and demonstrates 0.63% and 1.12% reduction in sensitivity. The device has also been exploited for the label-free detection of DNA hybridization and other biomolecules, such as plasma and hemoglobin with high accuracy and reliability. The proposed third work with six cavity resonators can detect six primary colors in the visible wavelength. An initial sensitivity of 648.41 nm/RIU and FOM of 141.29 are found based on the transmittance profile. The structural parameters are optimized to maximize the performance of the modeled device both as a color filter and a refractive index sensor. The optimized FOM , FOM^* and sensitivity are recorded as 218.80, 4.771×10^4 , and 865.31 nm/RIU, respectively. Therefore, the multi-purpose functionalities of the proposed nanosensors make them emerging contenders for state-of-the-art lab-on-a-chip tasks.

Chapter 1

Introduction and Background

1.1 Surface Plasmon Polariton

Back in time, the optical devices operated at GHz speed with μm dimension. The evolution of semiconductor technology has further reduced the size of the components to nm with the same operating speed but is limited by heat loss and time delays. Later on, the growing demand for a high-speed optical system resulted in the birth of dielectric photonics, incorporating PHz operating speed and μm device dimension. However, the bulky size of the dielectric photonics inhibits the high-density packaging of optical instruments due to the diffraction limit of light. Therefore, in a quest to integrate optical devices in chip-scale, the concept of Surface Plasmon Polaritons (SPPs) emerged, linking the gap between dielectric photonics and semiconductor technologies (fig. 1.1a) [1].

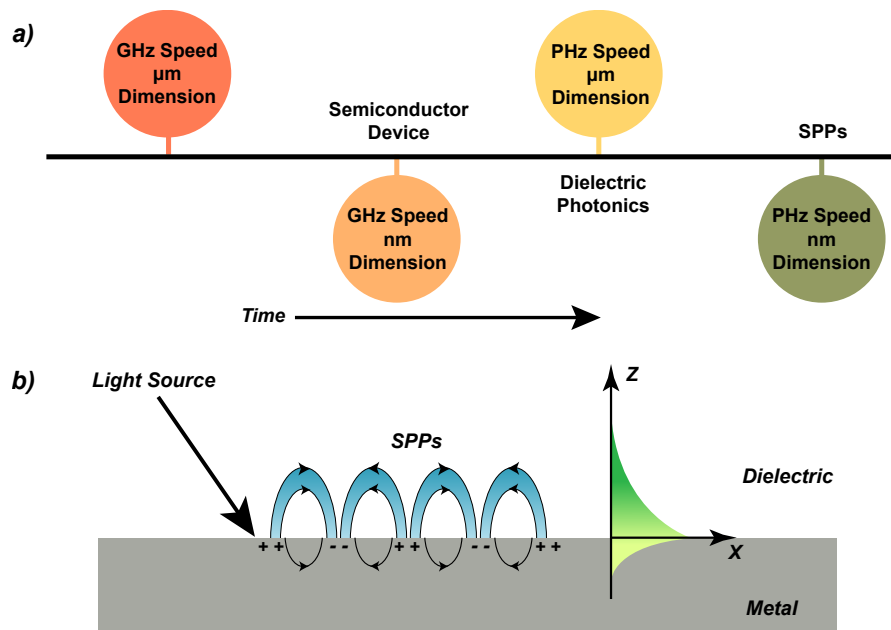


Figure 1.1: a) Evolution of device technologies (adapted from [1]). b) Formation and propagation of Surface Plasmon Polaritons (SPPs) (redrawn from [2]).

SPPs are electromagnetic (EM) waves generated due to the collective coupling of photons and oscillating electrons along a metal-dielectric interface at the resonant frequency (fig. 1.1b) [2]. The waves magnify light-metal interactions through the strong coupling of light to the interface. Such interactions break the diffraction limit barrier, enable nanoscale miniaturization of photonic circuits, and generate a high-magnitude local EM field [3], [4]. Furthermore, SPPs are transverse-magnetic (TM) in nature and decay exponentially at a direction normal to the interface (fig. 1.1b). If x -axis is the direction of propagation and z -axis is normal to the interface, the dispersion relation of the wave vector SPP_{k_x} is expressed as [2],

$$k_x = k_0 \times \sqrt{\frac{\epsilon_d \cdot \epsilon_m}{\epsilon_d + \epsilon_m}}, \quad (1.1)$$

where, $k_0 = \omega/c$ refers to the free-space wave vector. This decaying property is highly susceptible to changes in the surrounding environment, leading to the development of SPP based devices, for example, splitters, couplers, filters, sensors [5], [6].

1.2 Plasmonic Devices

1.2.1 Plasmonic Splitters

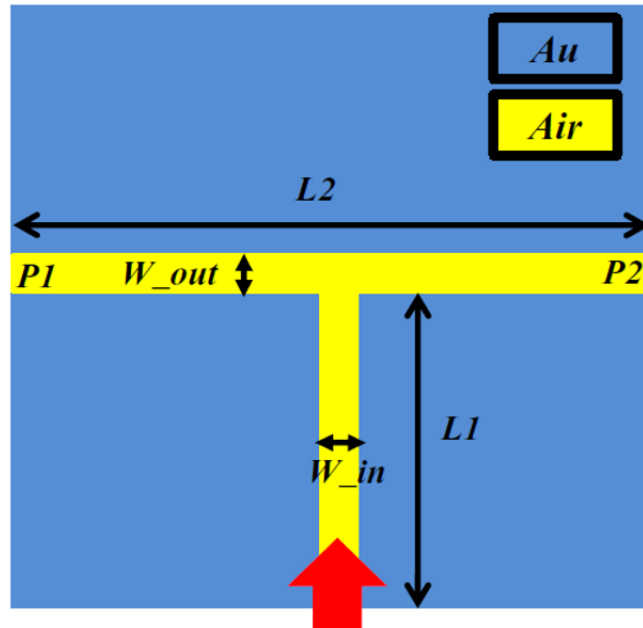


Figure 1.2: Plasmonic splitter proposed by [7].

Controlling the direction and the magnitude of the SPP in nano-scaled structure is vital to nano-photonic-related applications. Plasmonic splitters are devices used to control and split plasmonic waves between multiple output ports from a single input port. Splitters have various functions: power splitters are designed to regulate the flow

of power in specific directions; equal-power splitters distribute the input power equally to several output ports, and the polarization beam splitters (PBSs) handle polarization. These are essential elements for multi-way PIC systems. However, one fundamental issue that needs to be addressed is to ensure that the generated SPPs propagate in the desired direction and be split with a certain proportion. Several groups have suggested various methods for controlling and splitting plasmonic waves, such as splitters based on slot cavity, T and Y-shaped waveguide, and hybrid waveguide [7–10]. One of the proposed splitters is shown in fig. 1.2.

1.2.2 Plasmonic Couplers

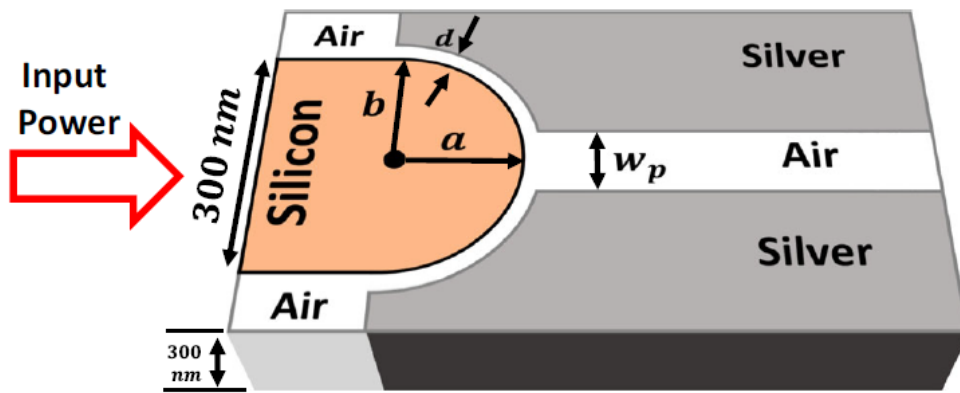


Figure 1.3: Plasmonic coupler proposed by [11].

On deep sub-wavelength scales, plasmonic structures formed by metal-dielectric-metal (MDM) waveguides can firmly confine light in the dielectric domain, which is not possible using traditional dielectric waveguides due to diffraction limit [12]. However, in the MDM region, SPPs have a smaller propagation length due to their high propagation loss at the surface. The drawback between mode confinement and propagation loss can be resolved by combining dielectric and plasmonic waveguides in the same configuration. Several distinct coupling methods have been suggested to enhance the coupling efficiency from a dielectric waveguide to a plasmonic waveguide. Such methods include tapered coupler, adiabatic tapered coupler, nonadiabatic tapered coupler, $\lambda/4$ coupler, direct coupling, and multi-section taper [13–18]. One of the proposed couplers is shown in fig. 1.3.

1.2.3 Plasmonic Filters

Plasmonic filters have drawn increasing attention recently in the field of signal processing. Plasmonic waveguides can create a series of filters that transmit light in various visible to near-infrared wavelength bands. There are two types of plasmonic filters,

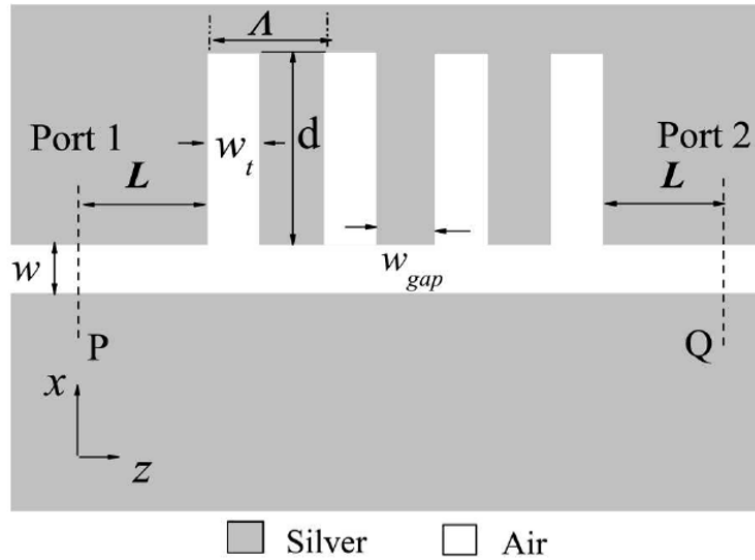


Figure 1.4: Plasmonic filter proposed by [19].

i.e., bandpass and band-stop filters. The band-stop filter prevents light with a specific frequency from propagating through the waveguide structures, and the bandpass filter allows the transmission of some frequency of light. Devices such as SPP reflectors require broad bandgaps, and wavelength division multiplexing (WDM) systems need narrow bandwidths. Recently, some plasmonic waveguide filters have been researched, such as tooth-shaped plasmonic waveguide filters, filters with disk resonators, rectangular-shaped resonators, and ring resonators [20–23]. Among all these applications mentioned above, color filters are of particular importance because of their excellent display and imaging potential. One of the proposed filters is shown in fig. 1.4.

1.2.4 Plasmonic Sensors

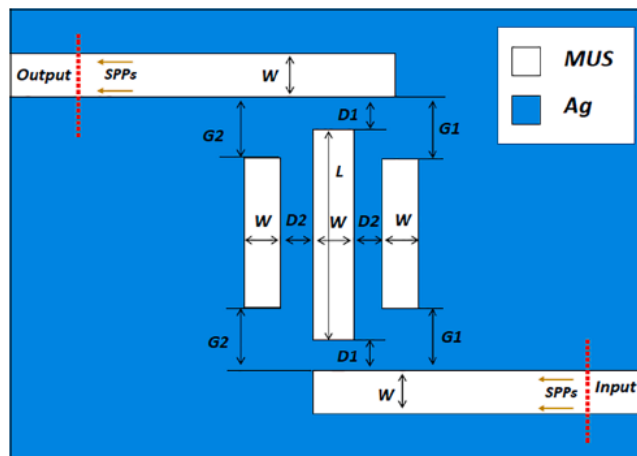


Figure 1.5: Plasmonic sensor proposed by [24].

Among the devices mentioned earlier, plasmonic sensors function utilizing the re-

fractive index (RI) change in the neighboring medium, making them highly sensitive to minor changes. Therefore, RI sensors and their sensing performance are continuously researched in different applications, such as temperature sensing [25], gas sensing [26], biological and chemical sensing [27]. One of the proposed sensors is shown in fig. 1.5. To date, numerous RI sensors are reported incorporating various kinds of waveguides, for example, Metal-Insulator-Metal (MIM) waveguide, Insulator-Metal-Insulator (IMI) waveguide, Hybrid waveguide. The next section elaborates on the schematics and the pros and cons of each waveguide system for plasmonic refractive index sensing.

1.3 Plasmonic Waveguides

1.3.1 Metal-Insulator-Metal (MIM) Waveguide

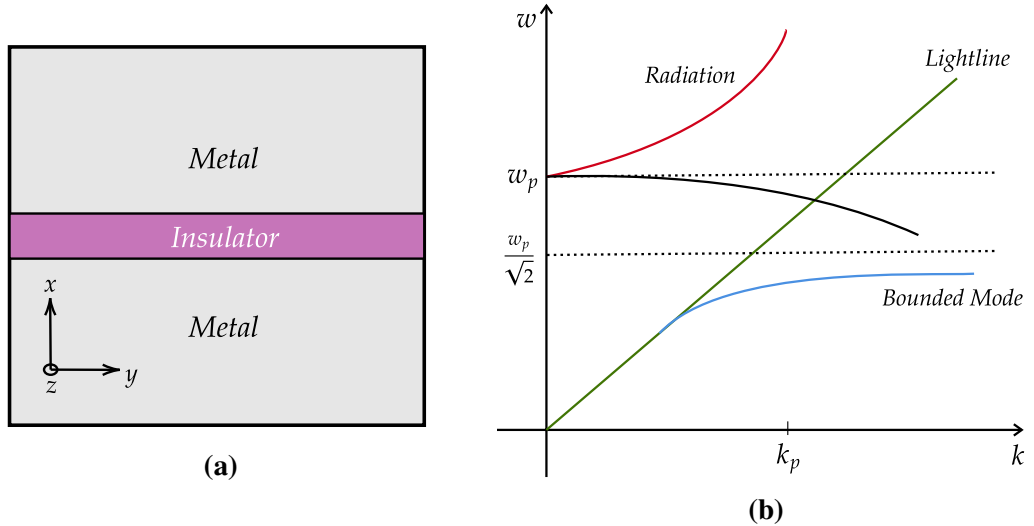


Figure 1.6: (a) MIM schematic. (b) Dispersion plot of MIM structure, adapted from [28].

Figure 1.6a exhibits the schematic of a MIM waveguide system, which consists of three parts: one insulating layer sandwiched between two metallic layers. The dispersion relation of a MIM waveguide is shown in fig. 1.6b, which has been analytically solved in [28]. Furthermore, fig. 1.7 displays the E -field profiles of the MIM arrangement considering the antisymmetric and symmetric propagation modes [29].

The MIM scheme offers numerous advantages, for example, strong confining of light at the subwavelength level, fabrication ease, acceptable propagation length (the length for which the strength of SPPs reduces to $1/e$ of the initial value). Therefore, researchers have performed further detailed analyses to explore different aspects of the MIM waveguide [29].

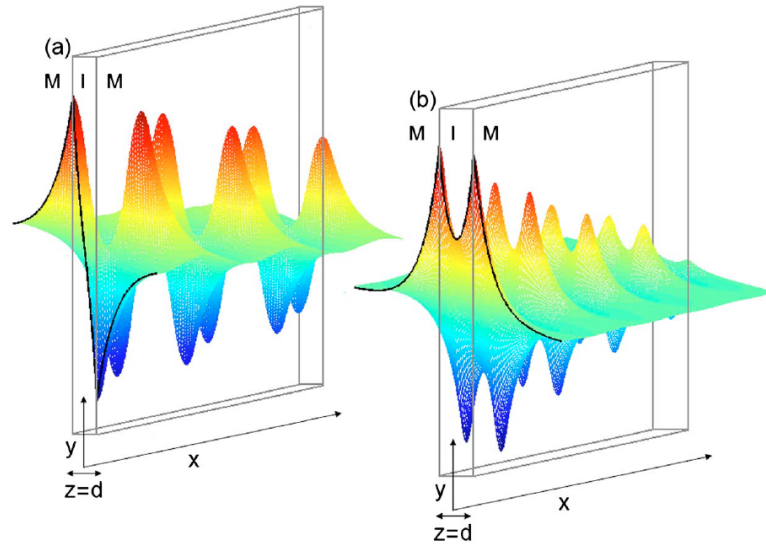


Figure 1.7: a) Antisymmetric and b) symmetric propagation modes [29].

1.3.2 Insulator-Metal-Insulator (IMI) Waveguide

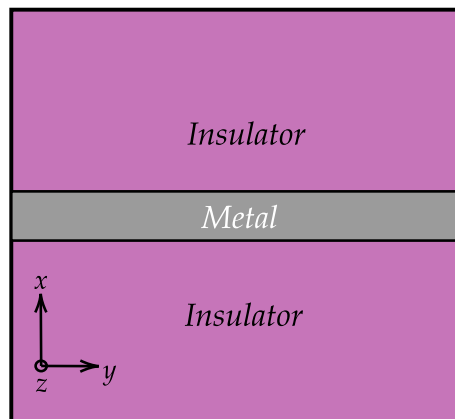


Figure 1.8: IMI schematic.

Conversely, in the IMI system, the metal part is sandwiched between two insulators (fig. 1.8). Figure 1.9 displays the magnetic field distribution of the IMI waveguide. The field distribution is strong at the interface, whereas the field lines are negligible at the center of the metal. As a result, the symmetric mode of the IMI scheme suffers from less attenuation and displays an increased propagation length than the MIM system. Hence, IMI systems are labeled as long-range SPP (LR-SPP) devices [30].

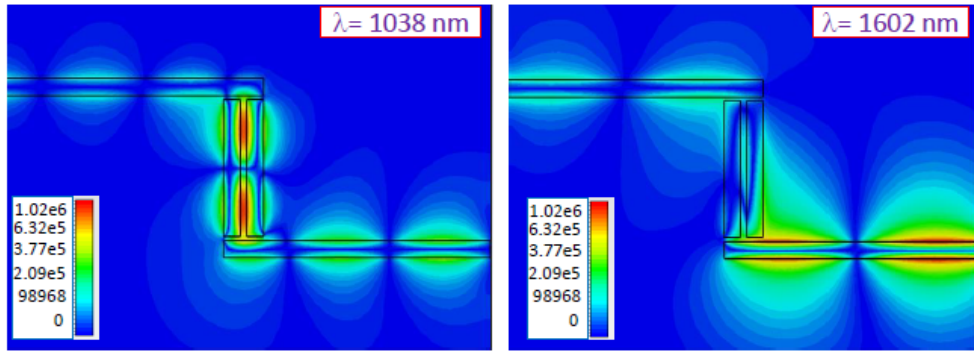


Figure 1.9: IMI field profile [31].

However, due to the weak confinement of the mode, the IMI waveguide is not suitable for subwavelength RI sensing. Therefore, extensive research has been conducted focusing MIM RI sensors.

1.3.3 Hybrid Waveguide

The concept of the hybrid waveguide is proposed to overcome the propagation loss associated with the conventional waveguides. Hybrid waveguide offers strong mode confinement and lower propagation loss simultaneously.

The setup of the hybrid waveguide consists of three sections: a dielectric of a low refractive index sandwiched between a metal and a dielectric of high refractive index.

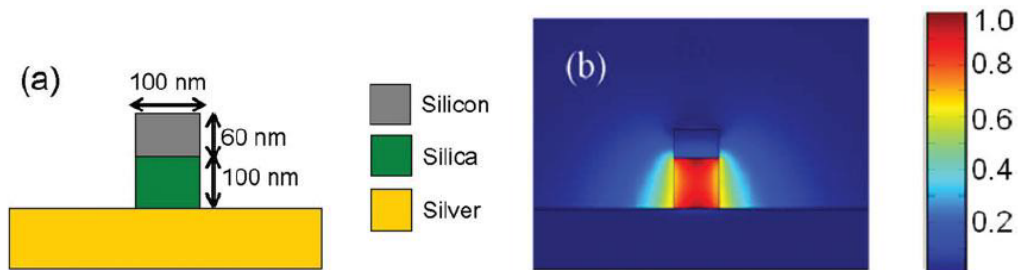


Figure 1.10: a) Hybrid waveguide proposed by [32]. b) Hybrid mode profile.

Figure 1.10 displays the first ever structure based on the hybrid waveguide system [32]. The setup consists of silica, which is sandwiched between silicon and silver. Silica acts as a buffer layer and enables the strong coupling of modes between silicon and silver. As a result, power is strongly confined at the silica layer, reducing leakage loss.

Butt *et al.* demonstrated an RI sensor incorporating a hybrid waveguide [33]. The setup exhibited high confinement of power at the buffer layer and displayed a high Q -factor of 969. Similarly, another RI sensor with a hybrid plasmonic ring resonator reported a maximum sensitivity of 800 nm/RIU [34]. Therefore, the hybrid waveguide

is gradually becoming an attractive choice in the field of plasmonic refractive index sensors due to its exciting features.

1.4 Literature Review

ENIAC (Electronic Numerical Integrator and Computer) was the first-ever digital system intended for electronic use in the 1940s. The *ENIAC* weighed around 30 tons and had a length of approximately 50 feet, consisting of 18000 vacuum tubes that functioned as electronic switches [35]. Nevertheless, the massive device lacked high processing speed and computational power than a modern computing machine [36]. The pre-requisite for an ultra-modern computer requires a compact, lightweight, and speedy system. The microprocessor system satisfies such conditions utilizing rapid transistors of 50 nm dimension rather than the vacuum tubes. However, a problem arises while transmitting digital information to the receiving end of the microprocessor [37]. A copper wire did not satisfy the necessary conditions entailed by the transistors [38]. An alternative solution was to employ optical fibers. Nevertheless, the fibers were 1000 times bigger than the electronic modules, and merging the two imbalanced systems in a single circuit was quite impractical [39]. Therefore, transmitting information on a nanometer scale became an urgent need. SPP emerged as the effective solution for the problem mentioned above [40].

Numerous plasmonic sensors utilizing the characteristics of SPPs have been published over the years. Zhao *et al.* [41] demonstrated a MIM RI sensor made of Fabry-Perot and ring cavities, with a sensitivity of 718 nm/RIU. A MIM waveguide structure with a triangular resonator reported a sensitivity of 986 nm/RIU [42]. Yang *et al.* [43] developed a refractive index sensor with a baffle and cross-shaped cavity, which exhibited a sensitivity of 1100 nm/RIU. Another MIM structure with a dual concentric double square-resonator displayed a sensitivity of 1380 nm/RIU [44]. Hexagonal cavity side-coupled with a straight MIM waveguide reported a sensitivity of 1562.5 nm/RIU [45]. A T-shaped MIM structure-based refractive index sensor with a sensitivity of 680 nm/RIU [46]. Zhang *et al.* [47] established a MIM waveguide, coupled with two stubs and a ring resonator, with 1268 nm/RIU sensitivity. A plasmonic square ring resonator based on MIM waveguide stated sensitivity of 1367 nm/RIU [48]. Su *et al.* [49] demonstrated a MIM waveguide coupled with an elliptical ring resonant cavity with a 1550 nm/RIU sensitivity. Umbrella resonator coupled with metal baffle provides a sensitivity of 1600 nm/RIU [50]. Diest *et al.* [51] placed two slits into the waveguide and distinguished three colors - red, green, and blue. Butt *et al.* [52] reported filtering white colors into six colors incorporating six unequal square cavities and found 700 nm/RIU sensitivity. Zhang *et al.* [53] demonstrated a multi-band four-

mode color filter possessing an ellipse resonator and recorded the highest sensitivity of 608 nm/RIU and figure of merit (FOM) of 105.02. Figure 1.11 (a–f) display some of the above-mentioned plasmonic sensors.

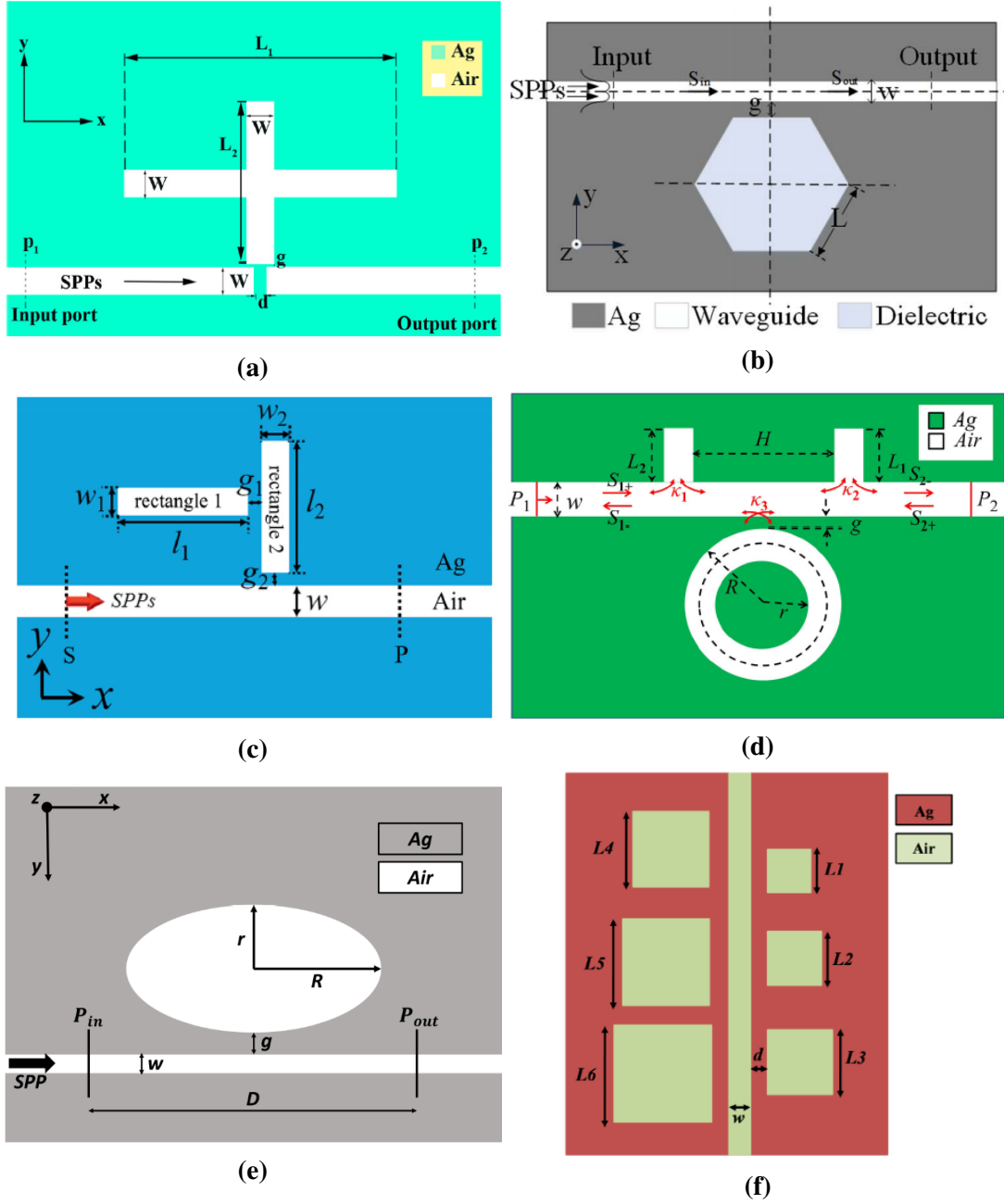


Figure 1.11: Some recent plasmonic sensors by (a) Yang *et al.* [43], (b) Xie *et al.* [45], (c) Wang *et al.* [46], (d) Zhang *et al.* [47], (e) Zhang *et al.* [53], and (f) Butt *et al.* [52].

Table 1.1 compares the recently proposed plasmonic sensors in terms of performance indicators, for example, sensitivity and FOM .

Table 1.1: Comparison between recent RI sensors.

Ref.	Year	Setup	Topology	Plasmonic Material	Model	S (nm/RIU)	FOM
[54]	2018	MIM	Double side-coupled square ring resonators	Ag	Drude	806	66
[55]	2018	MIM	Octagonal ring cavity	Ag	Drude-Lorentz	1540	-
[56]	2018	Periodic surface	Nano-rods	In tin oxide	-	1587	6.1
[57]	2018	MIM	Square type split ring resonator	Ag	Drude	1700	60.7
[58]	2018	MIM	Ring resonator	Ag	Drude	1383	93.1
[59]	2018	MIM	U-shaped resonator	Ag	Drude	917	180
[60]	2018	MIM	Elliptical ring resonator	Ag	Drude	1100	224
[61]	2019	Stacked graphene sheets	Asymmetric double graphene layers	Graphene	Drude	1900	-
[62]	2019	-	Nanocubes	Au	Drude	1002	417
[63]	2019	Array film	Y-shaped arrays	Ag	-	900	-
[64]	2019	Grating	Racetrack resonator	Si	-	1550	2000
[65]	2019	MIM	Two horizontal cavity	Ag	-	1382	35.3
[66]	2019	MIM	Triangular and circular cavity	Ag	Debye-Drude	1500	65.2

Table 1.1 continued from previous page

Ref.	Year	Setup	Topology	Plasmonic Material	Model	S (nm/RIU)	FOM
[67]	2019	MIM	Tooth cavity-coupled ring splitting cavity	Ag	Debye-Drude	1200	-
[68]	2020	Grating	Nano-array with rhombus particles	Au	Drude	1006	305.7
[69]	2020	MIM	Dual rectangular cavity system	Ag	Drude	701	-
[70]	2020	MIM	Elliptical cavity resonator	Ag	Drude	540	101.3
[71]	2020	MIM	Square ring resonator with nanodots	Ag	Lorentz-Drude	907	50.4
[72]	2020	MIM	Dual-band tunable absorber	Ag	Drude	1240.8	44.5
[73]	2020	MIM	Square ring resonator with nanodots	Ag	Debye-Drude	1240	20
[74]	2020	MIM	Semicircular resonant cavity coupled with a key-shaped resonant cavity	Ag	Drude	1261.67	-
[75]	2020	MIM	Disk resonator	Ag	Drude	1500	242.66
[76]	2020	MIM	Dual channel	Ag	-	1940	2235

Table 1.1 continued from previous page

Ref.	Year	Setup	Topology	Plasmonic Material	Model	S (nm/RIU)	FOM
[77]	2020	MIM	Double concentric square ring resonator and stubs	Ag	Drude	1270	58
[78]	2021	MIM	Triangular resonator	Ag	Lorentz-Drude	2713	35.1
[79]	2021	Grating	Complementary grating	Au/Si	Drude	1642	409
[80]	2021	MIM	U-shaped cavity	Ag	Debye-Drude	825	21.54
[81]	2021	MIM	Unequal vertical rectangular cavities	Ag	Lorentz-Drude	2625.87	26.04
[82]	2021	MIM	Asymmetric ring cavity	Au	-	440.2	52.6
[83]	2021	MIM	Pentagonal ring resonator	Ag	Lorentz-Drude	2325	46

However, the sensors mentioned in table 1.1 lack the high sensitivity needed for different RI sensing applications.

1.5 Thesis Objectives

The objectives of this thesis are:

- To propose state-of-the-art plasmonic refractive index sensors with MIM configuration.
- To optimize structural parameters to enhance various performance metrics such as sensitivity and *FOM*.
- To investigate the capability of the proposed sensors in biological applications, for example, detection of cancer cells and blood components.
- To exploit the sensitivity of the proposed sensors in chemical applications, such as determining glucose and ethanol concentration.
- To detect specific colors in various sectors, such as medical, industrial, and forensic, where the light of a particular wavelength is mandatory.

1.6 Thesis Layout

Chapter 1 presents a concise discussion of Surface Plasmon Polaritons (SPPs) and their importance in nanotechnology. Devices based on SPPs and different waveguide schemes are elaborately discussed. A detailed literature review on refractive index sensors to date and the thesis layout are also conferred.

Chapter 2 includes Maxwell's equations and generalized constitutive relations. The chapter also discusses the features of different EM wave solving algorithms, for example, FDTD, FIT, and FEM. The chapter concludes with the theoretical analysis of boundary conditions and fundamental mode.

Chapter 3 establishes the relationship between complex refractive index and complex relative permittivity. Notable plasmonic materials are designed using the Lorentz-Drude model. The chapter ends with the performance comparison of those materials.

Chapter 4 details the theories of different resonators, for example, ring resonator, cavity resonator, and concentric double-ring resonator. Various performance indicators of RI sensors, such as sensitivity, *FOM*, *Q-factor*, and detection limit are defined. Re-simulations of previously published works are also presented to justify the simulation environment.

Chapter 5 discusses three new schematics of the plasmonic RI sensor along with their fabrication technique. Extensive simulation and optimization are performed to capitalize on the performance of the sensors. The sensors are then deployed in different applications, for example, biosensing, chemical sensing, and color filtering.

Chapter 6 concludes by summarizing and comparing all the findings with recent works. Future approaches for potential improvement are also mentioned.

Chapter 2

Wave Theory

2.1 Maxwell's and Wave Equations

2.1.1 Maxwell's Equations

Maxwell's equations are a series of differential or integral expressions that describe the relationships between fundamental electromagnetic quantities. Solving Maxwell's equations is needed for electromagnetic analysis. Since the Finite Element Method (FEM) will accommodate this form, the equations are written in differential form. For general time-varying fields, Maxwell's equations can be expressed as,

$$\nabla \times H = J + \frac{\partial D}{\partial t}, \quad (2.1)$$

$$\nabla \times E = -\frac{\partial B}{\partial t}, \quad (2.2)$$

$$\nabla \cdot D = \rho, \quad (2.3)$$

$$\nabla \cdot B = 0, \quad (2.4)$$

where,

E = Electric field intensity,

D = Electric flux density/ displacement,

H = Magnetic field intensity,

B = Magnetic flux density,

J = Current density,

ρ = Electric charge density.

These equations are also known as *Maxwell-Ampere's Law*, *Faraday's Law*, *Gauss's Law of electric and magnetic form*, respectively. The *equation of continuity* is another

fundamental equation for Electromagnetic Wave (EM) wave expressed as,

$$\nabla \cdot J = -\frac{\partial \rho}{\partial t}. \quad (2.5)$$

2.1.2 Constitutive Equation

The macroscopic properties of the medium in a closed system can be described through the *constitutive equations* expressed as,

$$D = \varepsilon_0 E + P, \quad (2.6)$$

$$B = \mu_0(H + M), \quad (2.7)$$

$$J = \sigma E, \quad (2.8)$$

where, ε_0 , μ_0 , and σ denote the permittivity of vacuum, the permeability of vacuum, and the electric conductivity, respectively. ε_0 and μ_0 have the following values,

$$\mu_0 = 4\pi \times 10^{-7} H/m, \quad (2.9)$$

$$\varepsilon_0 = \frac{1}{c_0^2 \mu_0^2} = 8.854 \times 10^{-12} F/m, \quad (2.10)$$

where, c_0 denotes the velocity of EM waves in vacuum equal to the velocity of light. Here, the volume density of *electric dipole moment* is represented as the *electric polarization vector*, P which describes the polarization of a material due to the presence of an electric field (E). This polarization P is directly proportional to the electric field for the linear materials,

$$P = \varepsilon_0 \chi_e E, \quad (2.11)$$

where, χ_e denotes the *electric susceptibility*.

Similarly, the volume density of *magnetic dipole moment* is represented as the *magnetization vector*, M which describes the magnetization of a material due to the presence of a magnetic field (H). This magnetization M is directly proportional to the magnetic field for the linear materials,

$$M = \mu_0 \chi_m H, \quad (2.12)$$

where, χ_m denotes the *magnetic susceptibility*.

So, eq. (2.6) and eq. (2.7) become,

$$D = \varepsilon_0(1 + \chi_e)E = \varepsilon_0\varepsilon_r E = \varepsilon E, \quad (2.13)$$

$$B = \mu_0(1 + \chi_m)H = \mu_0\mu_r H = \mu H, \quad (2.14)$$

where,

$$\varepsilon_r = (1 + \chi_e), \quad (2.15)$$

$$\mu_r = (1 + \chi_m). \quad (2.16)$$

2.1.3 Generalized Constitutive Equations

When there is no electric field present, certain materials can have non-zero polarization. For more general cases, constitutive equations for these non-linear materials can be expressed as,

$$D = \varepsilon_0\varepsilon_r E + D_r, \quad (2.17)$$

where, D_r denotes the electric flux density in the absence of the electric field defined as *remanent electric flux density*.

Similarly, when there is no magnetic field present, certain materials can have non-zero magnetization. For more general cases, constitutive equations for these non-linear materials can be expressed as,

$$B = \mu_0\mu_r H + B_r, \quad (2.18)$$

where, B_r denotes the magnetic flux density in the absence of the magnetic field defined as *remanent magnetic flux density*.

Now, the current density expressed in eq. (2.8) can be generalized by adding an externally generated current J^e to the constitutive equation. This relation is expressed as,

$$J = \sigma E + J^e. \quad (2.19)$$

2.1.4 Wave Equation

In the propagation of EM waves, the wave equation is the most important feature and governing equation. The derivation of the wave equation (electric) of the EM wave from Maxwell's equations has been demonstrated. Equation (2.2) is multiplied with ∇ and expressed as,

$$\nabla \times (\nabla \times E) = \nabla \times \left(-\frac{\partial B}{\partial t} \right) = -\frac{\partial}{\partial t} (\nabla \times B). \quad (2.20)$$

Now, the evaluation of eq. (2.1), eq. (2.13), and eq. (2.14) result in,

$$\nabla \times (\nabla \times E) = -\mu\varepsilon \frac{\partial^2 E}{\partial t^2}. \quad (2.21)$$

Furthermore, considering $\frac{\partial}{\partial t} = j\omega$, $\varepsilon = \varepsilon_0\varepsilon_r$, and $\mu = \mu_0\mu_r$, this equation becomes,

$$\nabla \times (\mu_r^{-1} \nabla \times E) - k_0^2 \varepsilon_r E = 0, \quad (2.22)$$

where, k_0 denotes the wave number of free space defined as,

$$k_0 = \omega \sqrt{\mu_0 \varepsilon_0} = \frac{\omega}{c_0}. \quad (2.23)$$

Now, using the relation $\varepsilon_r = \eta^2$ for the linear materials where η is the refractive index and assuming $\mu_r = 1$, the equation can be re-written as,

$$\nabla \times (\nabla \times E) - k_0^2 \eta^2 E = 0. \quad (2.24)$$

2.2 Simulation Modeling

2.2.1 Finite-Difference Time Domain (FDTD)

The Yee Algorithm

The finite-difference time-domain (FDTD) incorporates the Yee algorithm for solving the EM wave problems. The essence of the FDTD technique is the sequential update of the electric and magnetic field values from the computational grid, enabling the user to loop around a magnetic field component with an electric field and vice-versa. Such a scheme significantly reduces the complexity of curl rotations in Maxwell's equations. Furthermore, only the values of neighbor cells are needed for updating the corresponding equations, facilitating the use of parallelization. To sum up, the basic two-step computation process of FDTD are:

1. Updating the magnetic field components from the electric field components of the previous iteration,
2. Updating the electric field components from the magnetic field components.

FDTD technique starts with the eq. (2.1) and eq. (2.2). The fields are three-dimensional vectors. Each equation can be expanded into three coupled scalar first-order differential equations, where the derivatives exist both in the time and space domains. Now, curl

of eq. (2.1) and eq. (2.2) yields into,

$$\begin{aligned}
 \partial H_x / \partial t &= 1/\mu \times \left[\partial E_y / \partial z - \partial E_z / \partial y \right], \\
 \partial H_y / \partial t &= 1/\mu \times \left[\partial E_z / \partial x - \partial E_x / \partial z \right], \\
 \partial H_z / \partial t &= 1/\mu \times \left[\partial E_x / \partial y - \partial E_y / \partial x \right], \\
 \partial E_x / \partial t &= 1/\varepsilon \times \left[\partial H_z / \partial y - \partial H_y / \partial z \right], \\
 \partial E_y / \partial t &= 1/\varepsilon \times \left[\partial H_x / \partial z - \partial H_z / \partial x \right], \\
 \partial E_z / \partial t &= 1/\varepsilon \times \left[\partial H_y / \partial x - \partial H_x / \partial y \right].
 \end{aligned} \tag{2.25}$$

The scalar equations are then converted to difference equations. The pre-requisites to generate difference equations are space and time discretization. Yee discretized the space by arranging the field components within a unit cell. The cell edges contain the electric field components, whereas the cell centers contain the magnetic field components. The corresponding setup thus places an electric field surrounded by four magnetic field components and vice-versa (fig. 2.2).

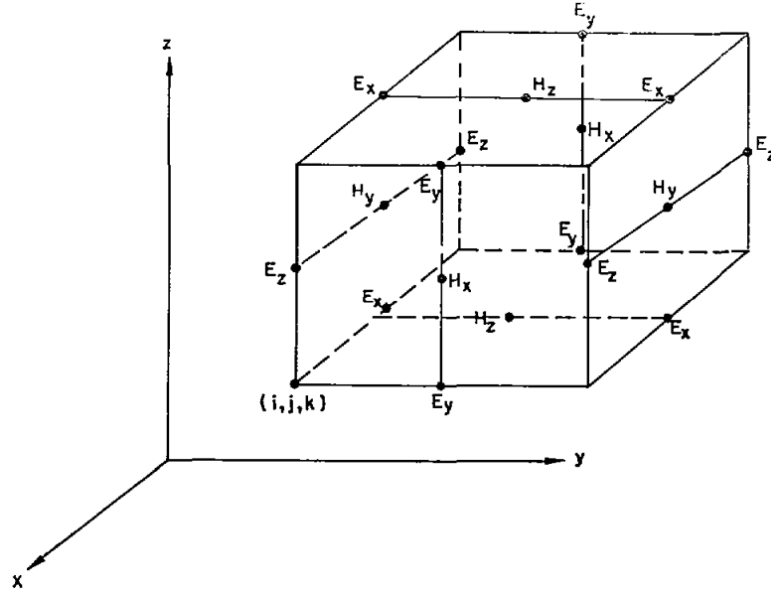


Figure 2.1: Yee's spatial grid [84].

Considering TE_z mode of propagation, the valid equations are:

$$\begin{aligned}\partial H_z / \partial t &= 1/\mu \times \left[\partial E_x / \partial y - \partial E_y / \partial x \right], \\ \partial E_x / \partial t &= 1/\varepsilon \times \partial H_z / \partial y, \\ \partial E_y / \partial t &= -1/\varepsilon \times \partial H_z / \partial x.\end{aligned}\tag{2.26}$$

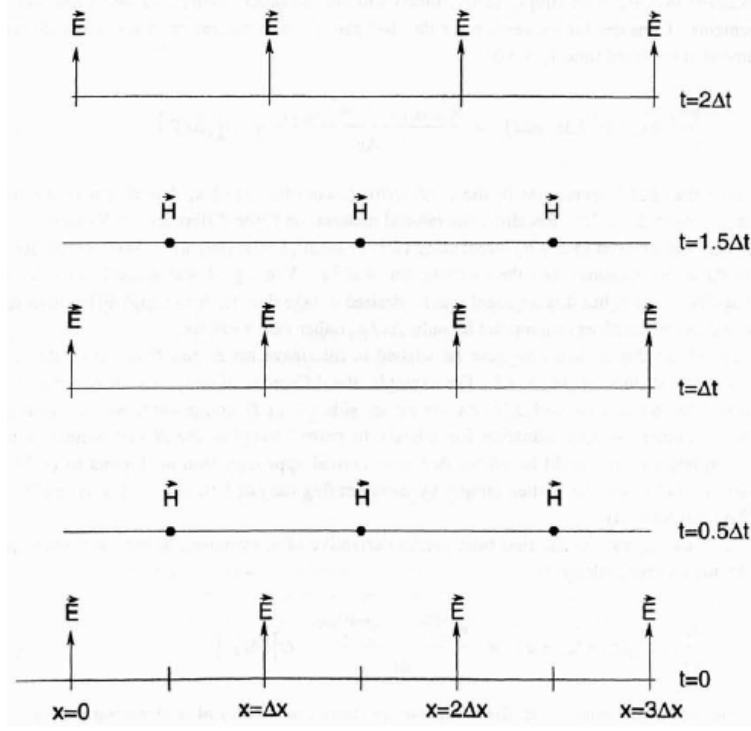


Figure 2.2: Temporal scheme of FDTD [85].

Now, applying the central difference theorem,

$$\begin{aligned}H_z \left(i + 1/2, j + 1/2, n + 1/2 \right) &= H_z \left(i + 1/2, j + 1/2, n - 1/2 \right) \\ &+ \Delta t / \Delta y \mu \left[E_x \left(i + 1/2, j + 1, n \right) - E_x \left(i + 1/2, j, n \right) \right] \\ &- \Delta t / \Delta x \mu \left[E_y \left(i + 1, j + 1/2, n \right) - E_y \left(i, j + 1/2, n \right) \right],\end{aligned}\tag{2.27}$$

$$\begin{aligned}E_x \left(i + 1/2, j, n + 1 \right) &= E_x \left(i + 1/2, j, n \right) \\ &+ \Delta t / \Delta y \varepsilon \left[\begin{aligned} &H_z \left(i + 1/2, j + 1/2 + 1, n + 1/2 \right) \\ &- H_z \left(i + 1/2, j - 1/2 + 1, n + 1/2 \right) \end{aligned} \right],\end{aligned}\tag{2.28}$$

$$E_y \left(i, j + 1/2, n + 1 \right) = E_y \left(i, j + 1/2, n \right) - \Delta t / \Delta x \varepsilon \begin{bmatrix} H_z \left(i + 1/2, j + 1/2, n + 1/2 \right) \\ -H_z \left(i - 1/2, j + 1/2, n + 1/2 \right) \end{bmatrix}. \quad (2.29)$$

The Yee algorithm must be stable during the numerical calculations; otherwise, the values of the electric and magnetic fields will increase exponentially and give erroneous results. The stability criterion is defined by the Courant–Friedrichs–Lewy condition:

$$\Delta t \leq 1 / c \sqrt{\left(1/\Delta x\right)^2 + \left(1/\Delta y\right)^2 + \left(1/\Delta z\right)^2}, \quad (2.30)$$

where, Δt = time step, Δx , Δy , Δz are spatial grid increments.

For 2D,

$$\Delta t \leq 1 / c \sqrt{\left(1/\Delta x\right)^2 + \left(1/\Delta y\right)^2}, \quad (2.31)$$

Let, $\Delta x = \Delta y$. Now,

$$\Delta t \leq 1 / c \sqrt{\left(1/\Delta x\right)^2 + \left(1/\Delta x\right)^2}, \quad (2.32)$$

$$\therefore \Delta t \simeq \Delta x / \sqrt{2}c.$$

Similarly, for 3D, let $\Delta x = \Delta y = \Delta z$. Now,

$$\Delta t \leq 1 / c \sqrt{\left(1/\Delta x\right)^2 + \left(1/\Delta x\right)^2 + \left(1/\Delta x\right)^2}, \quad (2.33)$$

$$\therefore \Delta t \simeq \Delta x / \sqrt{3}c.$$

Absorbing Boundary Condition (ABC)

Due to the limitation of computational power, in the FDTD simulations, a finite computational cell is simulated, which theoretically extends to infinity. The said boundary is an ideal absorber and guarantees zero reflection in the area of interest, ensuring correct output. Such a mechanism can be done by padding the exits of the computational domain with artificial absorbing materials, for example, Berenger's perfectly matched layer (PML) [86]. PML attenuates the fields till their values are zero and ensures zero reflections.

2.2.2 Finite Integration Technique (FIT)

Weiland *et al.* [87] first introduced the concept of the finite integration technique (FIT). FIT deals with the integral forms of Maxwell's equations eq. (2.1) – eq. (2.4). Furthermore, the technique utilizes all the vector components of the E and H-field located in a double-grid system. Weiland [88] later reformed the FIT equations and arranged them in a matrix format, which enabled the use of irregular and non-orthogonal grids for computation. Furthermore, another advantage of FIT is the use of fewer computational memories than FDTD [89].

A one-dimensional staggered grid is proposed to formulate the computational domain of FIT. Let the grid has an interval of $[0, K]$, where $0 = x_0 < x_1, \dots, x_n = K$ is a finite sequence of n grid points.

For a uniform 1D grid, let $x_i = i \times K/n, i = 0, \dots, m$ is the uniform grid with a mesh size of $S = K/n$. Thus, the corresponding staggered grid is $s_i = (i - 1/2) \times K/n, i = 1, \dots, m$ (fig. 2.3).

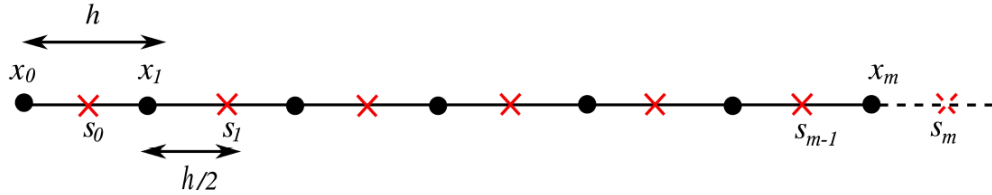


Figure 2.3: Uniform 1D grid [89].

Now, a set of corner points is defined as,

$$\xi_c := \{x_0, x_1, \dots, x_n\}. \quad (2.34)$$

Therefore, the corresponding staggered grid points are formulated as,

$$s_i = 0.5 \times (x_i + x_{i+1}), i = 0, \dots, n - 1, \quad (2.35)$$

denoting a grid increment of $h/2$. Therefore, the dual grid corresponding to ξ_c is,

$$\xi_s := \{s_0, s_1, \dots, s_{n-1}\}. \quad (2.36)$$

For a 3D staggered grid, a rectangular domain of the following expression is considered:

$$\xi = [0, K_x] * [0, K_y] * [0, K_z]. \quad (2.37)$$

Moreover, it is assumed that the 1D intervals $[0, K_x]$, $[0, K_y]$, and $[0, K_z]$ are discretized

by the following 1D grids,

$$\begin{aligned}\xi_c^x &:= \{x_0, x_1, \dots, x_n\}, \\ \xi_c^y &:= \{y_0, y_1, \dots, y_n\}, \\ \xi_c^z &:= \{z_0, z_1, \dots, z_n\},\end{aligned}\tag{2.38}$$

which are sets of grid points in x, y, and z-direction. Thus, eight possible grids can be formed utilizing these 1D grids, which are described as,

$$\xi_{t_x, t_y, t_z} = \xi_{t_x}^x * \xi_{t_y}^y * \xi_{t_z}^z,\tag{2.39}$$

where, $t_x, t_y, t_z = \{c, s\}^3$, c refers to the corner points and s refers to the staggered points. The grids mentioned above are incorporated in the numerical analysis of FIT.

2.2.3 Finite Element Method (FEM)

Partial differential equations (PDEs) are primarily used to describe the phenomena of fluid dynamics, electromagnetics, and thermal analysis. However, these phenomena involve inhomogeneous media and complicated geometry. Hence, the analytical solutions of the PDEs become complex. Such issues can be better handled by using the finite element method (FEM). The FEM can design EM wave problems with accurate material interfacing, accelerated convergence, adaptive meshing, and high numerical resolution than the conventional easier-to-code algorithms, for example, FDTD, Method of Moments (MoM). Pseudo-code of the FEM can be built for a particular field of interest and can be applied to other fields with little to no modification [90].

The four-step process to analyze any problem using the FEM are [91]:

1. Discretizing the computational domain into a finite number of elements,
2. Deriving the governing equations for a particular element,
3. Assembling all the elements in the solution region,
4. Solving the formulated equations.

A generalized wave equation can be expressed as,

$$\nabla^2 \varphi + k^2 \varphi = g,\tag{2.40}$$

where g is the source, k is the wavenumber, and φ is the unknown field potential. To simplify the problem, let $k = g = 0$. Thus, the Laplacian equation $\nabla^2 \varphi = 0$ is satisfied, and the mechanism of FEM can be illustrated.

Discretizing the Computational Domain

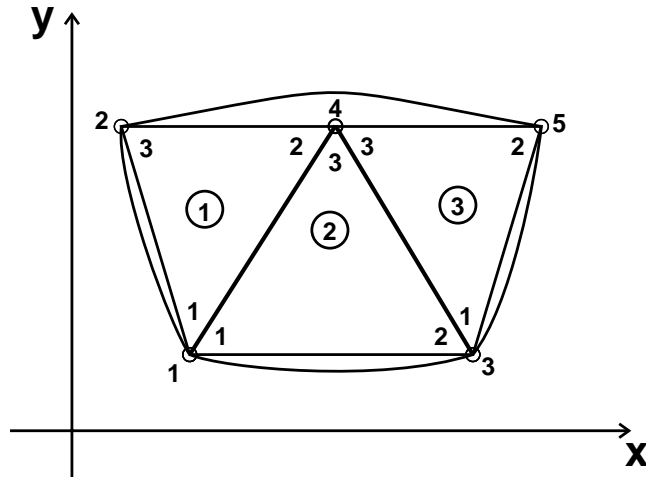


Figure 2.4: Finite element discretization.

A 2D region with three triangular elements is taken to explain the step-by-step process of the FEM (fig. 2.4). The estimated solution of the computational domain can be expressed as,

$$V(x, y) \approx \sum_{m=1}^L V_m(x, y), \quad (2.41)$$

where, $L = 3$ signifies the total number of elements.

The following polynomial function can be used to represent V_m considering triangular element,

$$V_m(x, y) = a + bx + cy, \quad (2.42)$$

where, a, b, c are unknown constants to be ascertained. Equation (2.42) approximates a linear association of V_m within the element. Thus, the E -field is also assumed to be uniform considering an element,

$$E_m = -\nabla V_m. \quad (2.43)$$

Governing Equations

Figure 2.5 depicts a single triangular element. The potential at different nodes can be defined in the matrix form,

$$[V_m] = \begin{bmatrix} V_{m1} \\ V_{m2} \\ V_{m3} \end{bmatrix} = \begin{bmatrix} 1 & x_1 & y_1 \\ 1 & x_2 & y_2 \\ 1 & x_3 & y_3 \end{bmatrix} \begin{bmatrix} a \\ b \\ c \end{bmatrix}. \quad (2.44)$$

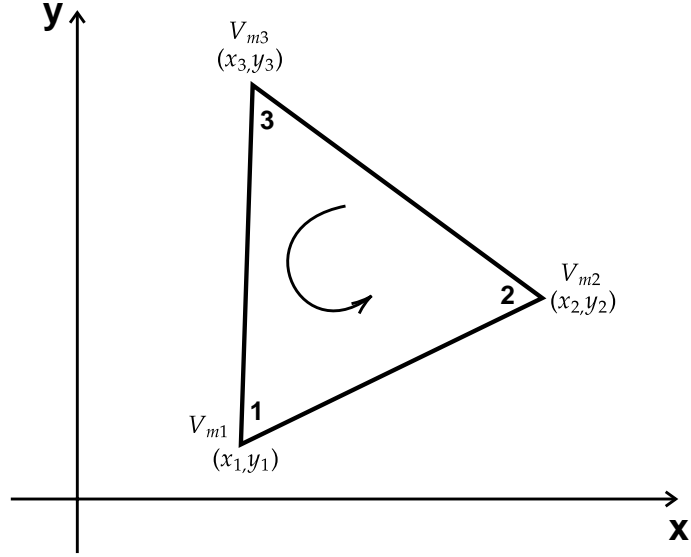


Figure 2.5: Single triangular element.

The unknown constants a , b and c can be determined as,

$$\begin{bmatrix} a \\ b \\ c \end{bmatrix} = \begin{bmatrix} 1 & x_1 & y_1 \\ 1 & x_2 & y_2 \\ 1 & x_3 & y_3 \end{bmatrix}^{-1} \begin{bmatrix} V_{m1} \\ V_{m2} \\ V_{m3} \end{bmatrix}. \quad (2.45)$$

Plugging the values in eq. (2.42),

$$V_m = \sum_{m=1}^3 \beta_m(x, y) V_{mi}, \quad (2.46)$$

where,

$$\begin{aligned} \beta_1 &= 1/2A \times [(x_2y_3 - x_3y_2) + (y_2 - y_3)x + (x_3 - x_2)y], \\ \beta_2 &= 1/2A \times [(x_3y_1 - x_1y_3) + (y_3 - y_1)x + (x_1 - x_3)y], \\ \beta_3 &= 1/2A \times [(x_1y_2 - x_2y_1) + (y_1 - y_2)x + (x_2 - x_1)y], \\ A &= 1/2 \times [(x_2 - x_1)(y_3 - y_1) - (x_3 - x_1)(y_2 - y_1)], \end{aligned} \quad (2.47)$$

where, A is the element area, and beta is labeled as the element shape function. Furthermore, the energy per unit length related to the element m employing the Laplace equation is,

$$W_m = 1/2 \int \varepsilon |E_m|^2 dS = 1/2 \int \varepsilon |\nabla V_m|^2 dS, \quad (2.48)$$

where, from eq. (2.46),

$$\nabla V_m = \sum_{m=1}^3 V_{mi} \nabla \beta_m. \quad (2.49)$$

Plugging eq. (2.49) into eq. (2.48),

$$W_m = 1/2 \times \varepsilon [V_m]^t [C^{(m)}] [V_e], \quad (2.50)$$

where, t denotes the transposed form and,

$$C_{ij}^{(m)} = \int \nabla \beta_i \cdot \nabla \beta_j dS, \quad (2.51)$$

$$[C^{(m)}] = \begin{bmatrix} C_{11}^{(m)} & C_{12}^{(m)} & C_{13}^{(m)} \\ C_{21}^{(m)} & C_{22}^{(m)} & C_{23}^{(m)} \\ C_{31}^{(m)} & C_{32}^{(m)} & C_{33}^{(m)} \end{bmatrix},$$

where, $[C^{(m)}]$ refers to the element coefficient matrix.

Assembling of the Elements

Let, total L number of elements are assembled to form the complete solution region.

The total energy of the assembled elements can be expressed as,

$$W_{total} = \sum_{m=1}^L W_m = 1/2 \varepsilon [V]^t [C] [V], \quad (2.52)$$

where,

$$[V] = \begin{bmatrix} V_1 \\ V_2 \\ \vdots \\ V_k \end{bmatrix}, \quad (2.53)$$

where, k is the total nodes present in a single element. A 5×5 global coefficient considering the global numbering can be expressed as,

$$[C] = \begin{bmatrix} C_{11} & C_{12} & C_{13} & C_{14} & C_{15} \\ C_{21} & C_{22} & C_{23} & C_{24} & C_{25} \\ C_{31} & C_{32} & C_{33} & C_{34} & C_{35} \\ C_{41} & C_{42} & C_{43} & C_{44} & C_{45} \\ C_{51} & C_{52} & C_{53} & C_{54} & C_{55} \end{bmatrix}. \quad (2.54)$$

Equation Solving

Minimum total energy ensures the satisfaction of the Laplace equation. Therefore,

$$\frac{\partial W}{\partial V_\phi} = 0, \phi = 1, 2, \dots, k. \quad (2.55)$$

Now, from eq. (2.52) and eq. (2.54),

$$\frac{\partial W}{\partial V_\phi} = 0 = V_1 C_{11} + V_2 C_{12} + V_3 C_{13} + V_4 C_{14} + V_5 C_{15}. \quad (2.56)$$

Thus, the general expression is,

$$\frac{\partial W}{\partial V_\phi} = 0 = \sum_{m=1}^k V_m C_{mk}. \quad (2.57)$$

Considering the 1st node as independent,

$$V_1 = -1/C_{11} \sum_{m=2}^5 V_m C_{mk}. \quad (2.58)$$

Therefore, the general form of expression is,

$$V_\phi = -1/C_{\phi\phi} \sum_{m=1, m \neq \phi}^k V_m C_{mk}. \quad (2.59)$$

Scattering Boundary Condition (SBC)

Scattering boundary condition (SBC) ensures a transparent simulation window for the incoming and outgoing/scattered waves. The scattered waves can be expressed as,

1. Plane scattered wave:

$$E = E_{sc} e^{-jk(n \cdot r)} + E_0 e^{-jk(K \cdot r)}. \quad (2.60)$$

2. Cylindrical scattered wave:

$$E = E_{sc} e^{-jk(n \cdot r)} / \sqrt{r} + E_0 e^{-jk(K \cdot r)}. \quad (2.61)$$

3. Spherical scattered wave:

$$E = E_{sc} e^{-jk(n \cdot r)} / r_s + E_0 e^{-jk(K \cdot r)}. \quad (2.62)$$

Scattering Parameters

Scattering parameters (S-parameters) are complex quantities used to describe the different characteristics, for example, transmittance, reflectance, absorbance for an N-port EM device. Defining voltage through the electric field is convenient in high-frequency operations. Furthermore, superposing the excited and reflected fields at the port generates the computed electric field, which can be expressed as,

$$E_{cm} = E_1 + \sum_{j=1} S_{j1} E_j. \quad (2.63)$$

The other ports with no excitation can be expressed as,

$$E_{cm} = \sum_{j=1} S_{j1} E_j. \quad (2.64)$$

Therefore, the S-parameters can be defined, considering various orthogonal modes, as,

$$\begin{aligned} S_{11} &= \int_{port1} ((E_{cm} - E_1) \cdot E_1) dA_1 / \int_{port1} (E_1 \cdot E_1^*) dA_1, \\ S_{21} &= \int_{port2} ((E_{cm} - E_2) \cdot E_2) dA_2 / \int_{port2} (E_2 \cdot E_2^*) dA_2, \\ S_{31} &= \int_{port3} ((E_{cm} - E_3) \cdot E_3) dA_3 / \int_{port3} (E_3 \cdot E_3^*) dA_3, \end{aligned} \quad (2.65)$$

and so on. Excitation of port two similarly generates S_{22} and S_{12} .

Thus, S-parameters for an N -port device are formulated as,

$$S = \begin{bmatrix} S_{11} & S_{12} & \cdots & S_{1N} \\ S_{21} & S_{22} & \cdots & S_{2N} \\ \vdots & \vdots & \ddots & \vdots \\ S_{N1} & S_{N2} & \cdots & S_{NN} \end{bmatrix}. \quad (2.66)$$

Transmittance can be defined as,

$$T = |S_{ji}|^2. \quad (2.67)$$

S-parameters for a two-port device carries the following meanings:

S_{11} = voltage reflection coefficient at the input port,

S_{21} = voltage transmission coefficient from port one to port two,

S_{12} = reverse voltage gain,

S_{22} = voltage reflection coefficient at the output port.

In decibels, S-parameters can be expressed as,

$$S_{ji}(dB) = 20 * \log_{10} (|S_{ji}|) . \quad (2.68)$$

Port Analysis

Ports are boundary conditions deployed to indicate the input and output sides. S-parameters are associated with the port analysis. Let E_1, E_2, E_3 be the normalized fields. Thus, the power is equal in corresponding ports. *Poynting* vector defines this power flow and can be expressed as,

$$S_{avg} = 1/2 \text{Re} (E \times H^*) . \quad (2.69)$$

Moreover, the amount of power flowing out is defined by the normal component of the *Poynting* vector,

$$n \cdot S_{avg} = n \cdot 1/2 \text{Re} (E \times H^*) . \quad (2.70)$$

Mode Analysis

Mode analysis calculates the lowest fundamental mode that propagates within the waveguide and can solve the propagation constant. A complex parameter is present in the phase term of the time-harmonic representation of the *E-field*,

$$E(r, t) = \text{Re} \left(\tilde{E}(r) e^{j\omega t - \gamma z} \right) , \quad (2.71)$$

and

$$\gamma = \psi_z + j\beta = -\lambda, \quad (2.72)$$

where, ψ_z is the damping along the propagating direction and β is the propagation constant.

Chapter 3

Plasmonic Materials

3.1 Refractive Index and Complex Permittivity

Analysts are continuously exploring about different properties of plasmonic materials. A plasmonic material is primarily characterized by its complex dielectric function: permittivity and permeability. Due to the weak impact of the magnetic field upon metals, μ is considered unity.

Thus, the complex permittivity of a plasmonic material can be expressed as,

$$\varepsilon(\omega) = \varepsilon_1(\omega) - i\varepsilon_2(\omega), \quad (3.1)$$

where,

$\varepsilon_1(\omega)$ = real part of $\varepsilon(\omega)$, responsible for polarization. A negative $\varepsilon_1(\omega)$ reflects a better plasmonic nature, and

$\varepsilon_2(\omega)$ = imaginary part of $\varepsilon(\omega)$, responsible for the propagation loss of the SPPs. An increasing $\varepsilon_2(\omega)$ represents a lossy system.

Now, the complex refractive index can be expressed as,

$$\eta = \eta_1 - i\kappa, \quad (3.2)$$

where, η_1 = refractive index, and κ = extinction coefficient. Moreover, refractive index and permittivity are interrelated. Thus,

$$\begin{aligned} \eta_1 &= 1/\sqrt{2} \times \sqrt{(\sqrt{(\varepsilon_1^2 + \varepsilon_2^2)} + \varepsilon_1)}, \\ \kappa &= 1/\sqrt{2} \times \sqrt{(\sqrt{(\varepsilon_1^2 + \varepsilon_2^2)} - \varepsilon_1)}. \end{aligned} \quad (3.3)$$

3.2 Material Modeling

In 1998, Rakic *et al.* performed experiments on eleven potential plasmonic materials and computed the values needed to fit the two famous models used extensively for material modeling at high optical frequencies: Drude and Lorentz-Drude [92].

3.2.1 Drude Model

Various studies have found that two factors mainly influence the complex permittivity equation: the free-electron effects/intraband effects and the bound-electron effects/interband effects. The intraband effects can be defined using the Drude model in the following form:

$$\varepsilon_{free}(\omega) = 1 - \frac{\omega_p^2}{(\omega^2 - i\omega\Gamma_0)}, \quad (3.4)$$

where, ω_p and Γ_0 refer to the plasma frequency and collision frequency, respectively.

3.2.2 Lorentz Model

Similarly, the interband effects can be expressed using the Lorentz model in the following way,

$$\varepsilon_{bound}(\omega) = \sum_{i=1}^m \frac{\gamma_i \omega_i^2}{(\omega_i^2 - \omega^2 + i\omega\Gamma_i)}, \quad (3.5)$$

where, ω_i , γ_i , and Γ_i refer to the resonant frequency, oscillator strength and damping frequency, respectively.

3.2.3 Lorentz-Drude Model

The summation of eq. (3.4) and eq. (3.5), therefore, constitutes eq. (3.6), the Lorentz-Drude Model.

$$\underbrace{\varepsilon(\omega)}_{\text{Lorentz-Drude}} = \underbrace{\varepsilon_{free}(\omega)}_{\text{Drude}} + \underbrace{\varepsilon_{bound}(\omega)}_{\text{Lorentz}}. \quad (3.6)$$

In the next section, the real and imaginary parts of complex permittivity and complex refractive index of four materials (Ag, Au, Cu, Al) are numerically calculated and then plotted using the Lorentz-Drude model.

3.3 Ag Modeling

Table 3.1 lists the Lorentz-Drude Parameters for Ag.

Table 3.1: Lorentz-Drude Parameters for Ag [92].

Parameters	Values (eV)
Plasma frequency ($\hbar\omega_p$)	9.01
Collision frequency (Γ_0)	0.048
Oscillator strength (γ_i)	[0.845; 0.065; 0.124; 0.011; 0.840; 5.646]
Damping frequency (Γ_i)	[0.048; 3.886; 0.452; 0.065; 0.916; 2.419]
Resonant frequency (ω_i)	[0; 0.816; 4.481; 8.185; 9.083; 20.29]

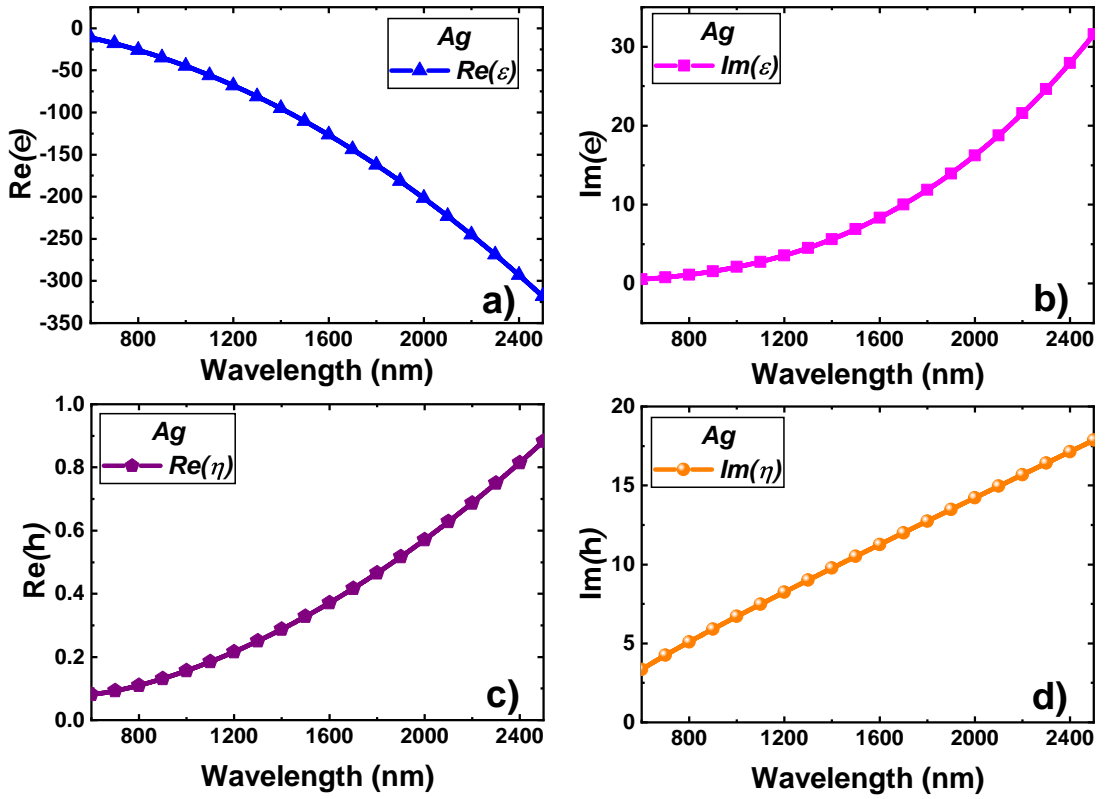


Figure 3.1: a) Real part of complex permittivity, b) Imaginary part of complex permittivity, c) Real part of complex refractive index, and d) Imaginary part of complex refractive index for Ag.

3.4 Au modeling

Table 3.2 lists the Lorentz-Drude Parameters for Au.

Table 3.2: Lorentz-Drude Parameters for Au [92].

Parameters	Values (eV)
Plasma frequency ($\hbar\omega_p$)	9.03
Collision frequency (Γ_0)	0.053
Oscillator strength (γ_i)	[0.760; 0.024; 0.010; 0.071; 0.601; 4.384]
Damping frequency (Γ_i)	[0.053; 0.241; 0.345; 0.870; 2.494; 2.214]
Resonant frequency (ω_i)	[0; 0.415; 0.830; 2.969; 4.304; 13.32]

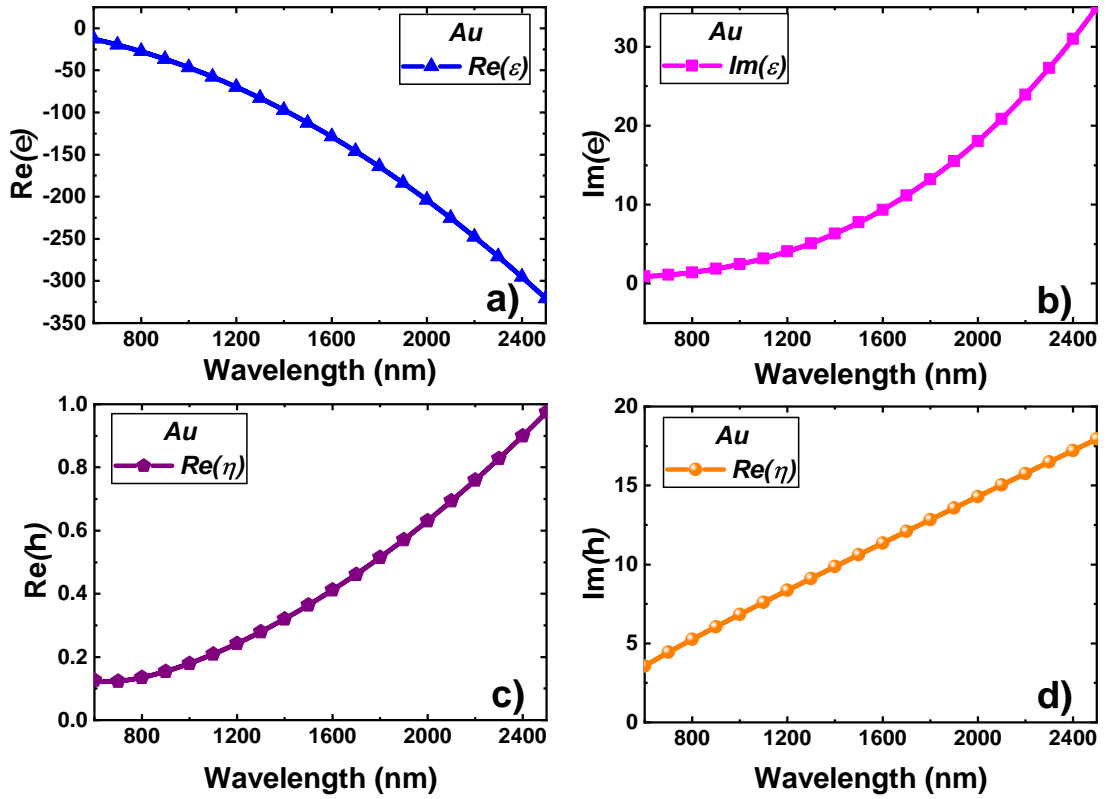


Figure 3.2: a) Real part of complex permittivity, b) Imaginary part of complex permittivity, c) Real part of complex refractive index, and d) Imaginary part of complex refractive index for Au.

3.5 Cu Modeling

Table 3.3 lists the Lorentz-Drude Parameters for Au.

Table 3.3: Lorentz-Drude Parameters for Cu [92].

Parameters	Values (eV)
Plasma frequency ($\hbar\omega_p$)	10.83
Collision frequency (Γ_0)	0.030
Oscillator strength (γ_i)	[0.575; 0.061; 0.104; 0.723; 0.638; 0]
Damping frequency (Γ_i)	[0.030; 0.378; 1.056; 3.213; 4.305; 0]
Resonant frequency (ω_i)	[0; 0.291; 2.957; 5.300; 11.18; 0]

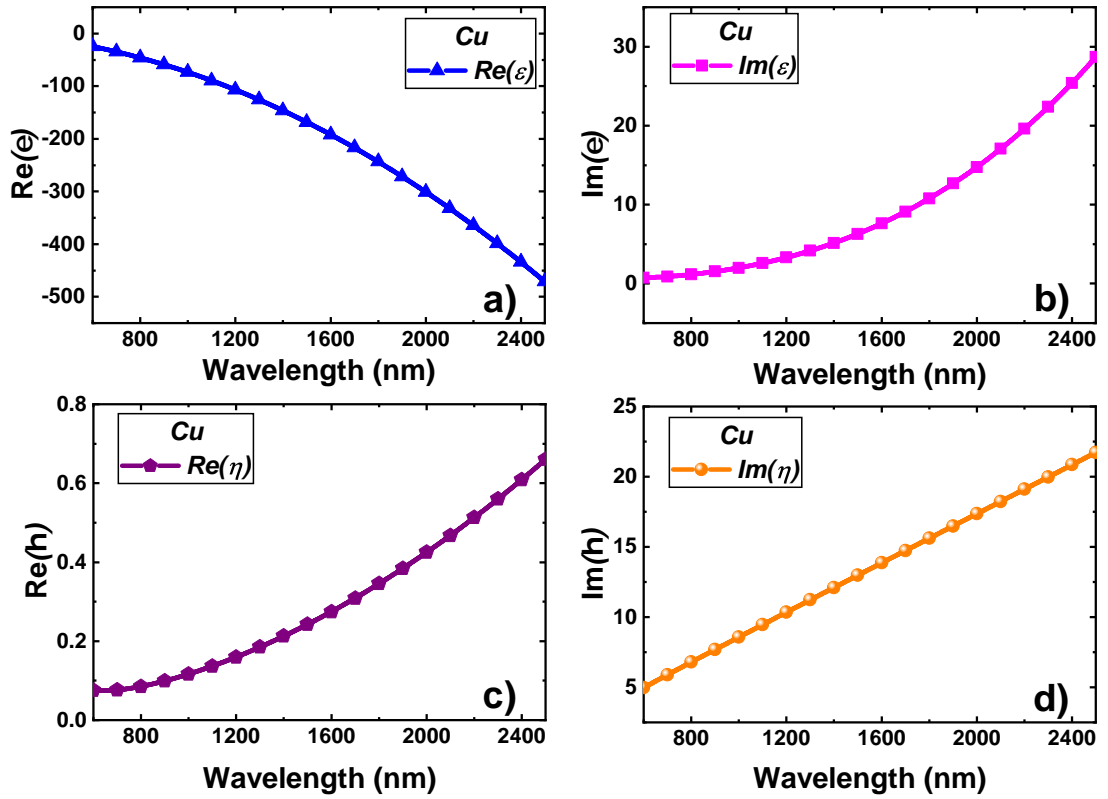


Figure 3.3: a) Real part of complex permittivity, b) Imaginary part of complex permittivity, c) Real part of complex refractive index, and d) Imaginary part of complex refractive index for Cu.

3.6 Al Modeling

Table 3.4 lists the Lorentz-Drude Parameters for Al.

Table 3.4: Lorentz-Drude Parameters for Al [92].

Parameters	Values (eV)
Plasma frequency ($\hbar\omega_p$)	14.98
Collision frequency (Γ_0)	0.047
Oscillator strength (γ_i)	[0.523; 0.227; 0.050; 0.166; 0.030; 0]
Damping frequency (Γ_i)	[0.047; 0.333; 0.312; 1.351; 3.382; 0]
Resonant frequency (ω_i)	[0; 0.162; 1.544; 1.808; 3.473; 0]

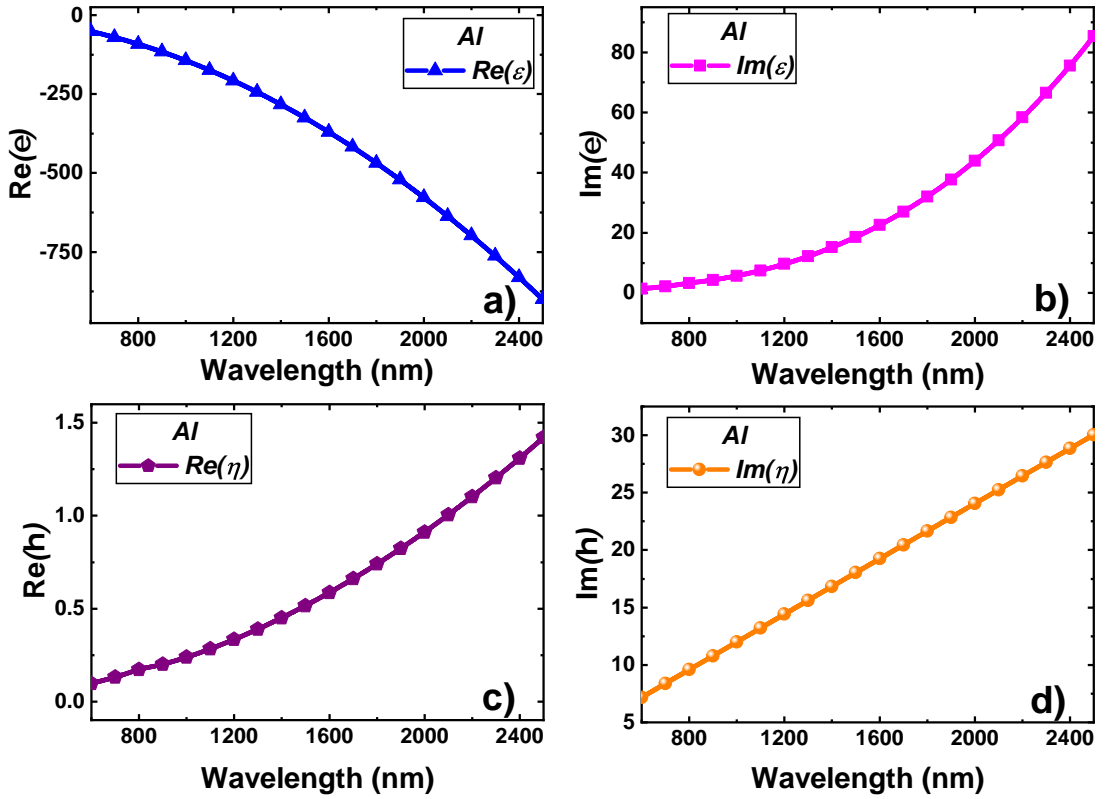


Figure 3.4: a) Real part of complex permittivity, b) Imaginary part of complex permittivity, c) Real part of complex refractive index, and d) Imaginary part of complex refractive index for Al.

3.7 Comparison among Plasmonic Materials

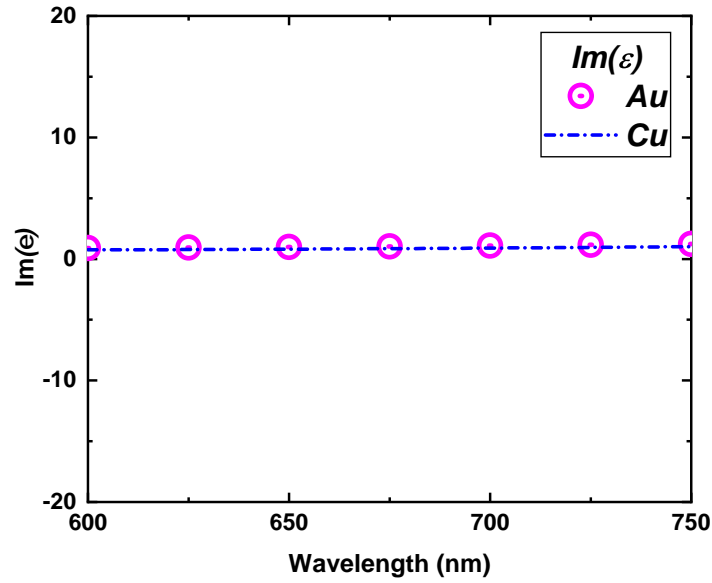


Figure 3.5: Performance of Au and Cu in the wavelength range of 600 nm to 750 nm [93].

Cu has the next best conductivity after Ag. Thus, Cu is expected to display promising plasmonic performance. From the wavelength range 600 nm to 750 nm, the performance of Cu and Au are comparable (fig. 3.5). Additionally, Cu is cheaper than Ag and Au. Therefore, Cu emerges as a promising alternative for Ag and Au. However, for plasmonic applications, Cu is primarily disregarded due to fabrication challenges: being easily oxidized and forming Cu_2O and CuO [93].

Al displays the highest loss among the materials. Al also suffers from an oxidation problem like Cu, rapidly forming a 3 nm thick layer of Al_2O_3 under the ambient situation. Therefore, the fabrication of optical devices utilizing Al is quite complicated [93].

Therefore, Ag and Au are the most suitable candidate for different plasmonic applications. However, silver has the least Drude damping and exhibits higher sensitivity and better detectability than gold. Furthermore, gold adheres poorly with the substrate and suffers from percolation when fabricated in nanoscale [94], [95]. Hence, the suggested sensor deploys silver as the plasmonic material.

Chapter 4

Performance Metrics of an RI Sensor

4.1 Ring and Cavity Resonator

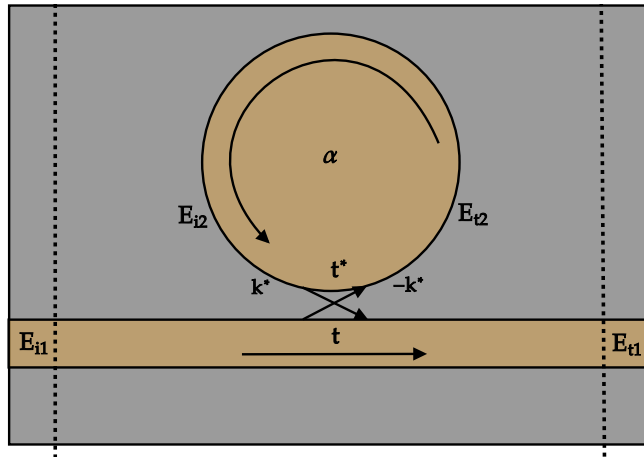


Figure 4.1: Schematic of a plasmonic waveguide coupled with a ring structure.

A circular ring structure based simple MIM waveguide with a radius R is shown in fig. 4.1. Presuming lossless; single polarized coupling between the straight waveguide and ring, the input-output relation can be formulated by the matrix [96],

$$\begin{bmatrix} E_{t1} \\ E_{t2} \end{bmatrix} = \begin{bmatrix} t & k \\ -k^* & t^* \end{bmatrix} \begin{bmatrix} E_{i1} \\ E_{i2} \end{bmatrix}. \quad (4.1)$$

Where,

- E_{i1} = Complex mode amplitude of the input signal,
- E_{i2} = Complex mode amplitude transmitted from the ring,
- E_{t1} = Complex mode amplitude of the output signal,
- E_{t2} = Coupled complex mode amplitude of the ring,
- k, t = coupling parameters.

The attenuation constant includes various losses that exist during wave propagation in the ring. According to the reciprocal essence of the network, the symmetric matrix results in,

$$|k^2| + |t^2| = 1. \quad (4.2)$$

For simplicity, E is inferred as a unity, Hence,

$$E_{i2} = \alpha \cdot e^{j\theta} E_{t2}. \quad (4.3)$$

Here, α is the loss coefficient of the ring and θ can be stated as,

$$\theta = \frac{\omega L}{c} = \frac{2\pi c_0 L}{\lambda_c} = k \cdot n_{eff} \cdot L = \beta \cdot L, \quad (4.4)$$

where, $c = c_0/n_{eff}$ is the phase velocity of the ring, n_{eff} is the effective refractive index, $L = 2\pi r$ is the circumference of the ring, r is the radius of the ring and $k = 2\pi/\lambda$ is the propagation constant.

From eq. (4.1) and eq. (4.3) the following terms E_{t2} , E_{t1} and E_{i2} can be represented as,

$$E_{t2} = -k^* + t^*(\alpha e^{j\theta} E_{t2}),$$

$$E_{t2}(1 - t^* \alpha e^{j\theta}) = -k^*,$$

$$E_{t2} = \frac{-k^*}{1 - t^* \alpha e^{j\theta}}, \quad (4.5)$$

$$E_{t1} = \frac{-\alpha + t e^{-j\theta}}{-\alpha t^* + e^{-j\theta}}, \quad (4.6)$$

$$E_{i2} = \frac{-\alpha k^*}{-\alpha t^* + e^{-j\theta}}. \quad (4.7)$$

The modal power can be obtained as the square of the complex mode amplitude E . Transmitted power P_{t1} at the output waveguide and the circulating power in the ring P_{i2} can be exhibited on resonance in the following form, having $\theta + \varphi_t = 2\pi m$, where $t = |t| e^{j\varphi_t}$ is the coupling loss, φ_t denotes the coupling phase, and m is an integer,

$$P_{t1} = |E_{t1}|^2 = \frac{\alpha^2 + |t|^2 - 2\alpha |t| \cos(\theta + \varphi_t)}{1 + \alpha^2 |t|^2 - 2\alpha |t| \cos(\theta + \varphi_t)} = \frac{(\alpha - |t|)^2}{(1 - \alpha |t|)^2}, \quad (4.8)$$

$$P_{i2} = |E_{i2}|^2 = \frac{\alpha^2(1 - |t|^2)}{(1 - \alpha |t|)^2}. \quad (4.9)$$

From eq. (4.4), the resonant wavelength λ_m can be obtained as,

$$\frac{2\pi}{\lambda_m} \cdot n_{eff} \cdot L = 2\pi \left(m - \frac{\varphi_t}{2\pi} \right), \quad (4.10)$$

$$\lambda_m = \frac{n_{eff} \cdot L}{m - (\varphi_t/2\pi)}. \quad (4.11)$$

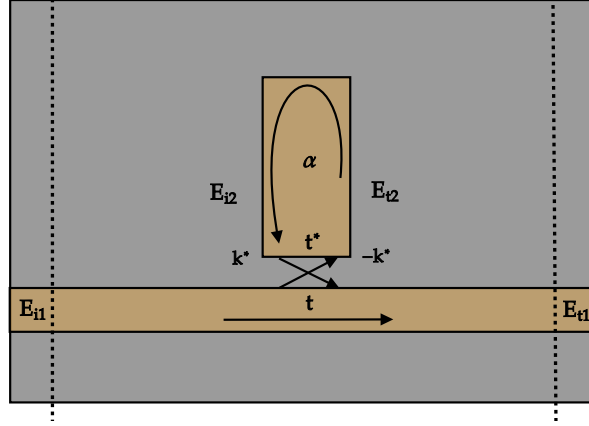


Figure 4.2: Schematic of a plasmonic waveguide coupled with a cavity resonator.

Correspondingly, the cavity resonator follows the same eq. (4.1) – eq. (4.11).

4.2 Concentric Double-Ring Resonator (CDRR)

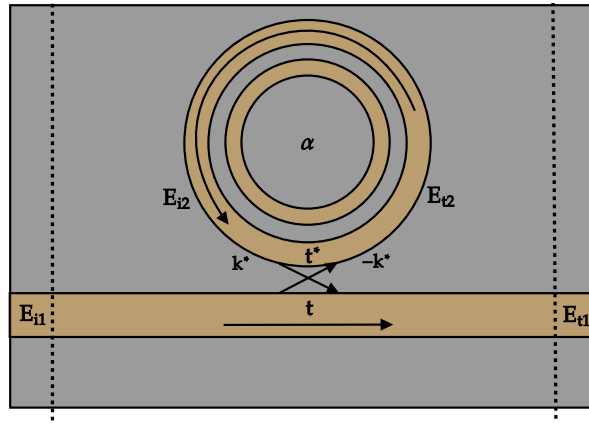


Figure 4.3: Schematic of a plasmonic waveguide coupled with a concentric double-ring resonator.

Similarly, fig. 4.3 displays MIM waveguide based concentric double-ring resonator (CDRR) structure. The resonance condition of a CDRR is derived by superpositioning the resonance of single rings [eq. (4.11)]. Figure 4.4 displays the effect of rings. The transmittance spectrum of CDRR is an approximate superposition of inner and

outer ring spectra with minor shifts, validating the resonance condition. According to eq. (4.11), the minor shifts of the resonant wavelengths occur as the interactivity between the two rings changes the η_{eff} of individual rings [97].

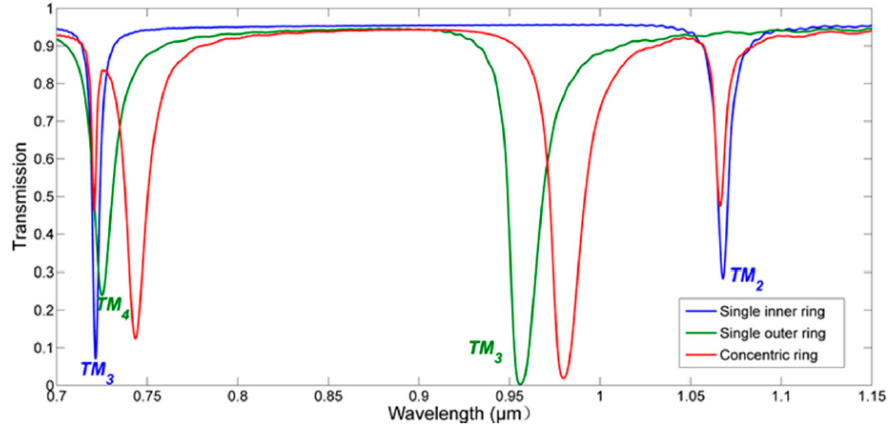


Figure 4.4: Effect of rings on CDRR structure [97].

4.3 Performance Metrics

Four performance parameters (e.g., Sensitivity, Figure of Merit, Quality-factor, and Detection Limit) of an RI sensor are comprehensively studied in this section. Improvements in these parameters are essential for various applications of RI sensors in nanoplasmonic technology.

4.3.1 Sensitivity (S)

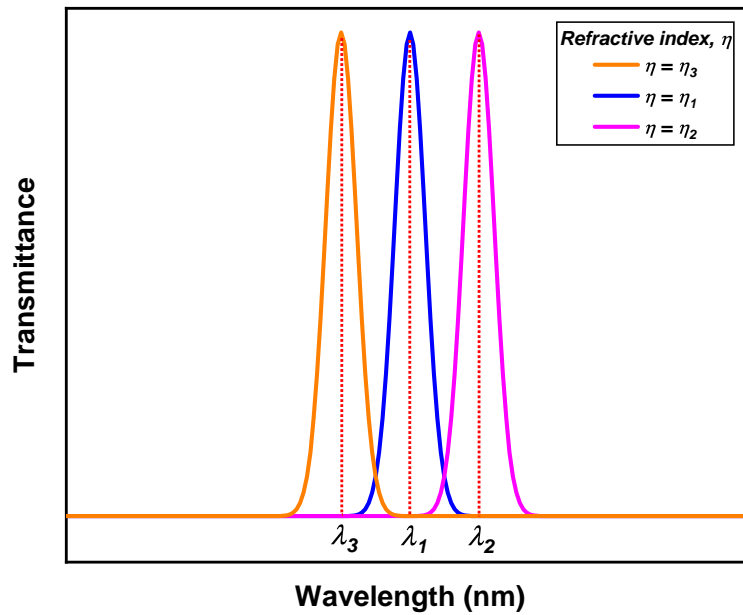


Figure 4.5: Sensitivity calculation.

The most critical performance criterion of an RI sensor is its sensitivity. Sensitivity (S) is obtained from the change in resonant wavelength position and the corresponding change in refractive index by the following equation [98],

$$S = \Delta\lambda/\Delta\eta, \quad (4.12)$$

where, $\Delta\lambda$ = change in resonant wavelength, and $\Delta\eta$ = change in refractive index.

The change in resonant wavelength can be either in the form of redshift or blueshift. In fig. 4.5, the pink curve is redshifted, whereas the orange curve is blueshifted from the center blue curve. By taking the difference between corresponding η and λ , S can be calculated.

4.3.2 Figure of Merit (FOM)

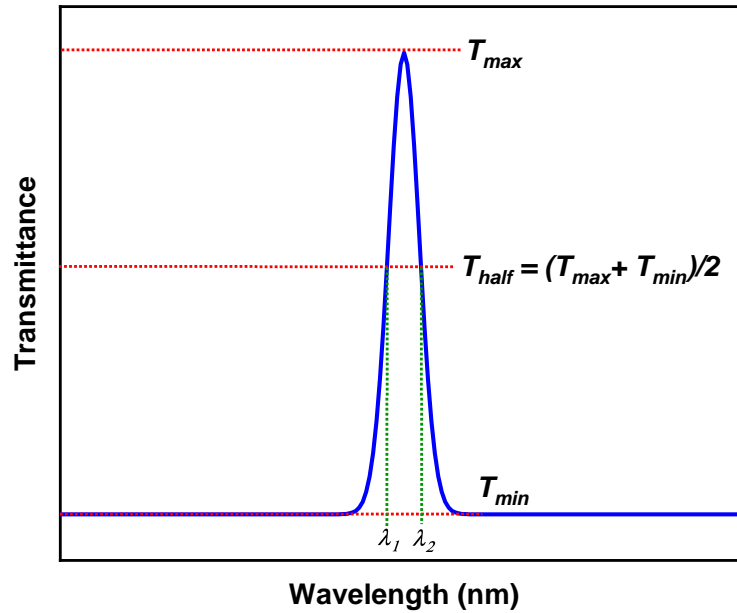


Figure 4.6: Figure of Merit calculation.

Figure of merit (FOM/FOM^*) is another benchmark to evaluate the performance of the RI sensor. A higher value of FOM/FOM^* enables the RI sensor to detect the resonant peaks readily and can be calculated as [99],

$$FOM = S/FWHM, \quad (4.13)$$

$$FOM^* = \Delta T/T\Delta\eta, \quad (4.14)$$

where, $FWHM$ means the Full Width At Half Maximum, T refers to the transmittance of the suggested sensor, $\Delta T/\Delta\eta$ is the transmittance change (ΔT) at a specific wave-

length due to a change in refractive index (Δn).

From fig. 4.6, the *FWHM* can be calculated by taking the average of maximum and minimum transmittance, T_{half} . T_{half} then intersects the transmittance curve into λ_1 and λ_2 . The difference between these two wavelengths is *FWHM*.

4.3.3 Quality-factor (*Q-factor*)

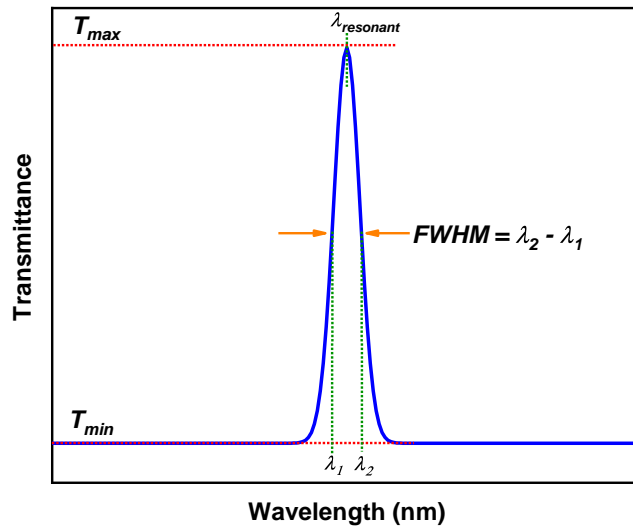


Figure 4.7: Q-factor calculation.

Quality-factor (*Q-factor*) is a performance criterion for filtering purposes, and can be defined as [31],

$$Q - factor = \lambda_{resonant} / FWHM, \quad (4.15)$$

where, $\lambda_{resonant}$ is the resonant wavelength, and *FWHM* is the Full Width at Half Maximum.

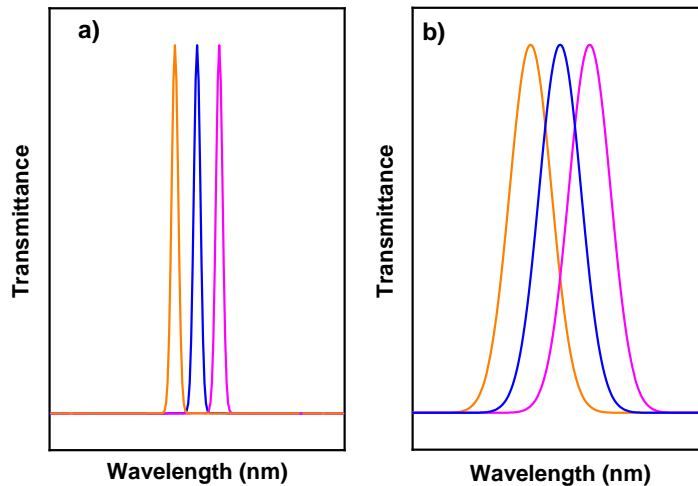


Figure 4.8: (a) High *Q-factor* and (b) low *Q-factor* representation.

Figure 4.8a denotes a sharp/high Q-factor response which is highly suitable for plasmonic filtering. Figure 4.8b displays low Q-factor response and is inefficient in filtering tasks.

4.3.4 Detection Limit (DL)

The detection limit is an important performance indicator for bio-sensors, specifying the minimum refractive index change of the bio-samples that can be accurately measured. Detection limit (DL) can be defined as [100],

$$DL = \Delta\lambda_{\min}/S, \quad (4.16)$$

where, $\Delta\lambda_{\min} = 0.001$ nm is the minimum resolution of a state-of-the-art spectrum analyzer, and S is the sensitivity value.

4.4 Re-Simulation with COMSOL Multiphysics

It is essential to re-simulate some published works to ensure proper simulation setup for the proposed devices. In this section three such works are re-evaluated using the commercial EM software, COMSOL Multiphysics.

4.4.1 Chen *et al.*

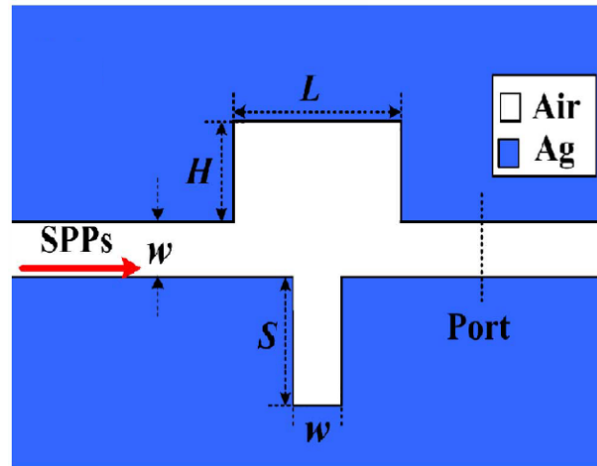


Figure 4.9: Schematic of Chen *et al.* [101]

A MIM-based RI sensor of Chen *et al.*, titled "A Refractive Index Nanosensor Based on Fano Resonance in the Plasmonic Waveguide System," published in *IEEE Photonics Technology Letter*, is opted for the re-simulation [101]. Figure 4.9 exhibits the

schematic structure of the sensor. The geometric parameters of the structure are presented in table 4.1.

Table 4.1: Geometric parameters of the structure [101].

Parameters	Denoted symbol	Value	Unit
Length of groove	L	200	nm
Height of groove	H	225	nm
Length of stub	S	225	nm
Width of stub and waveguide	W	50	nm

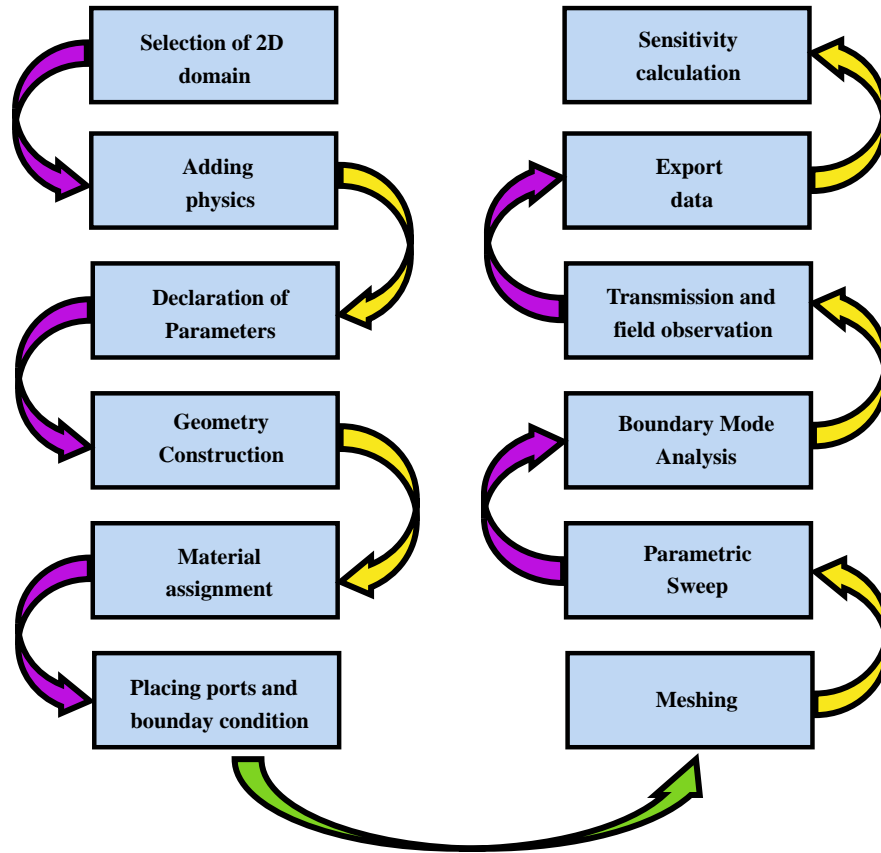


Figure 4.10: Block diagram representation of the simulation procedure.

A sequential process to re-simulate the structures in COMSOL Multiphysics is presented in fig. 4.10. Firstly, a 2D domain and proper physics are chosen. Appropriate parameters are then selected, and the sensor geometry is constructed to rebuild the sensor layouts. Subsequently, plasmonic materials, ports, and boundary conditions are assigned to the structure. Afterward, a suitable meshing option is selected to discretize the structure to obtain accurate results. The parametric sweep option enables the user to simulate the structure with different refractive index values and other various parameters. Thenceforward, the boundary mode analysis is used to assess the transmission

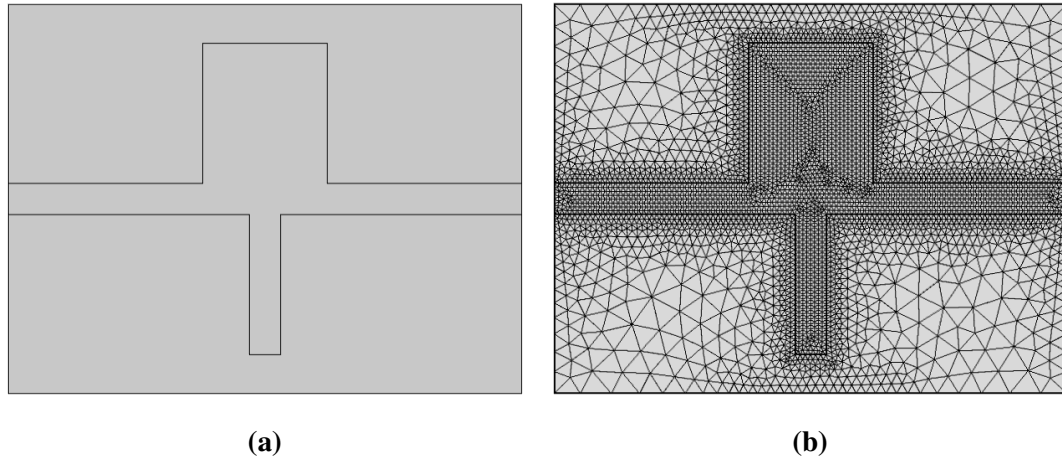


Figure 4.11: (a) 2D view. (b) Mesh view.

spectra and field distribution of the sensor. The data is then exported to numerical software, for example, *MATLAB*, and sensitivity is calculated.

Figure 4.11a and fig. 4.11b show the re-simulated geometry and the triangular mesh structure in COMSOL Multiphysics software. The transmission spectrum at a refractive index $n = 1.00$ for the original simulation by Chen *et al.* is presented in fig. 4.12a. The re-simulated spectrum for the same wavelength range is shown in fig. 4.12b. The magnetic field distribution $|H_z|^2$ for both the original and re-simulated works are illustrated in fig. 4.13a – fig. 4.13d, and the results are almost similar in range.

The final transmission profile at varying refractive index demonstrated by Chen *et al.* is re-evaluated and presented in fig. 4.14. Both the transmittance peaks display redshift with increasing refractive index. The sensitivity of the original work is 1260 nm/RIU, and the re-simulated work is 1290 nm/RIU, calculated using eq. (4.12). The maximum difference (2.38 %) in sensitivity is insignificant to consider. Hence, the

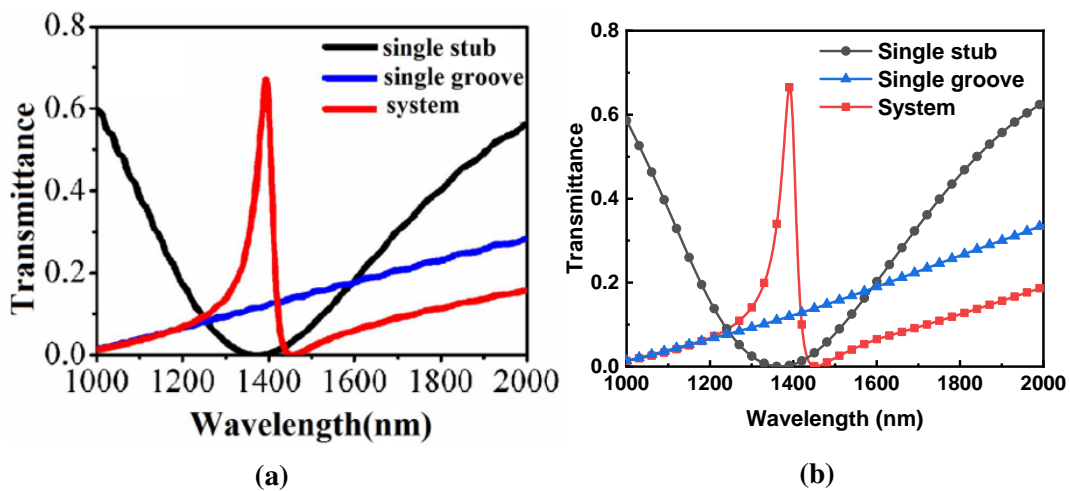


Figure 4.12: (a) Results by Chen *et al.* [101]. (b) Re-simulated results.

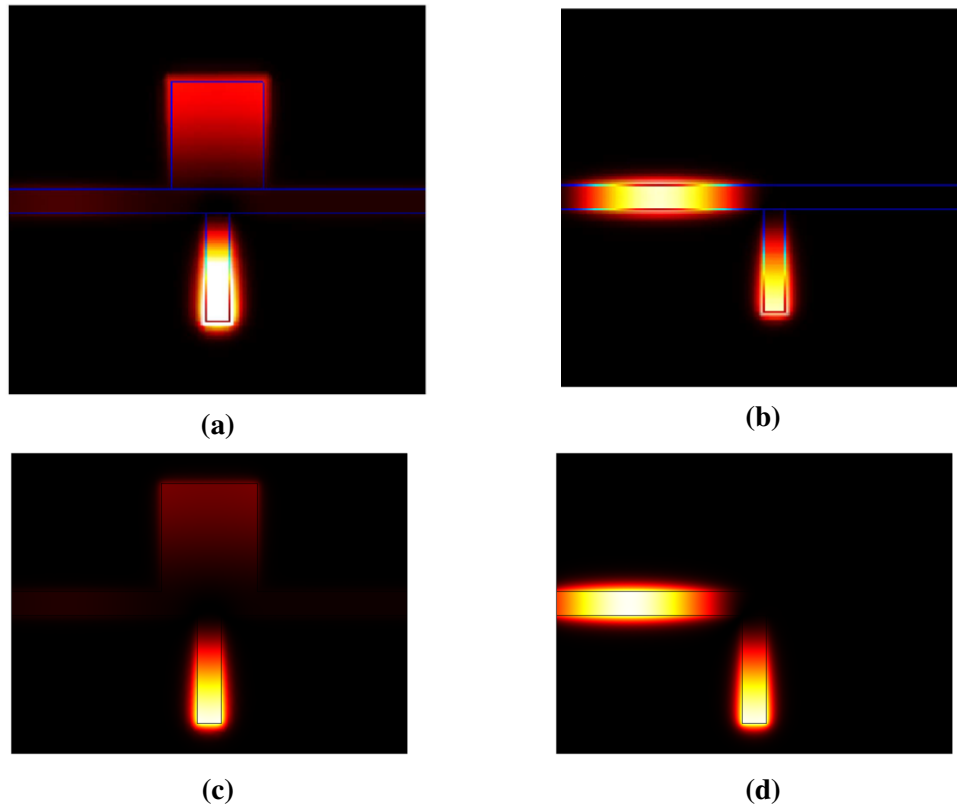


Figure 4.13: $|H_z|^2$ with and without the groove at the resonance wavelength $\lambda = 1392$ nm (a) – (b) by Chen *et al.* [101] and (c) – (d) re-simulated work.

re-simulated numerical results were successfully verified by the simulation procedures and are proficient for the proposed sensors.

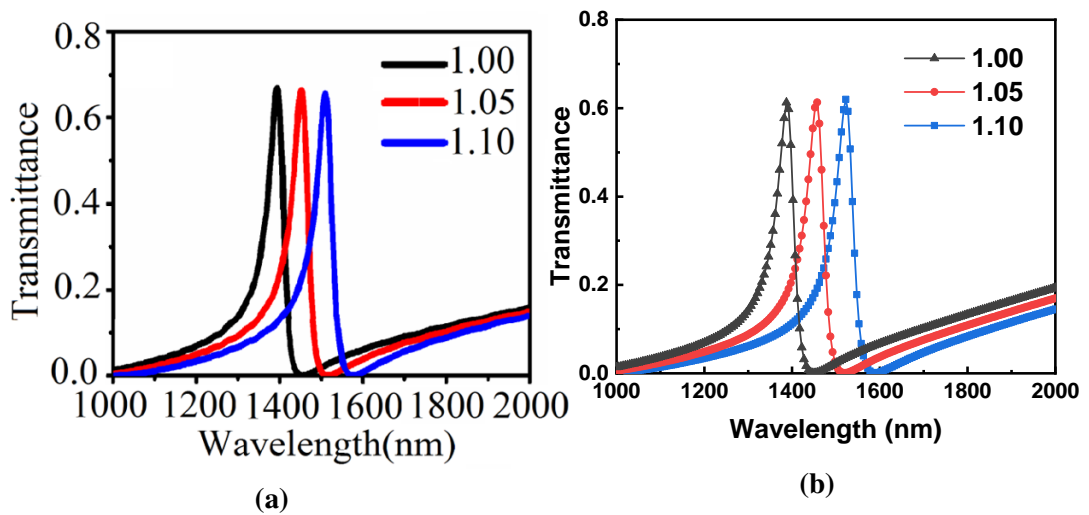


Figure 4.14: Transmission profile (a) by Chen *et al.* [101], (b) re-simulated work.

4.4.2 Zhang *et al.*

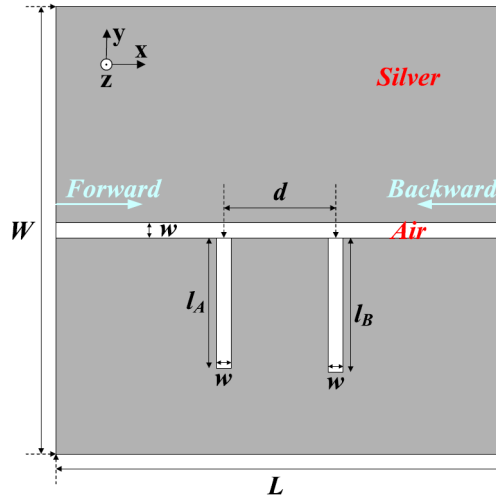


Figure 4.15: Schematic of Zhang *et al.* [102]

Table 4.2: Geometric parameters of the structure [102].

Parameters	Denoted symbol	Value	Unit
Length of first stub	L_A	625	nm
Length of second stub	L_B	660	nm
Distance between two stubs	d	450	nm
Width of the system	w	50	nm

Figure 4.15 represents a MIM based plasmonic waveguide system with dual stub resonators of Zhang *et al.*, titled "**Unidirectional Reflectionless Propagation in Plasmonic Waveguide System Based on Phase Coupling Between Two Stub Resonators**," published in *IEEE Photonics Journal* [102]. Table 4.2 displays the values of the structural parameters.

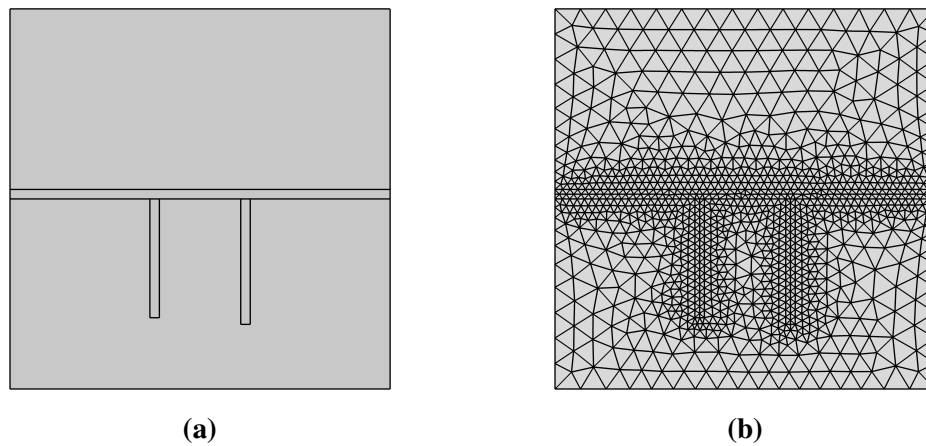


Figure 4.16: (a) 2D view. (b) Mesh view.

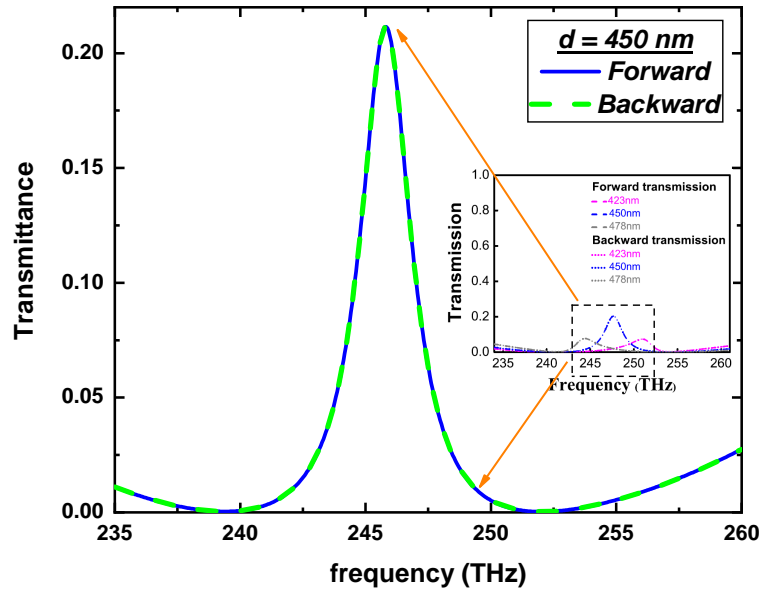


Figure 4.17: Forward and backward transmission profiles for $d = 450$ nm.

Figure 4.16a and fig. 4.16b exhibit the 2D and mesh views, respectively. To validate the precision of COMSOL Multiphysics, for $d = 450$ nm, forward and backward transmittance profiles of the structure in fig. 4.17 are plotted. The reproduced figure matches with the inset figure, which is the transmittance profile obtained by Zhang *et al.* [102]

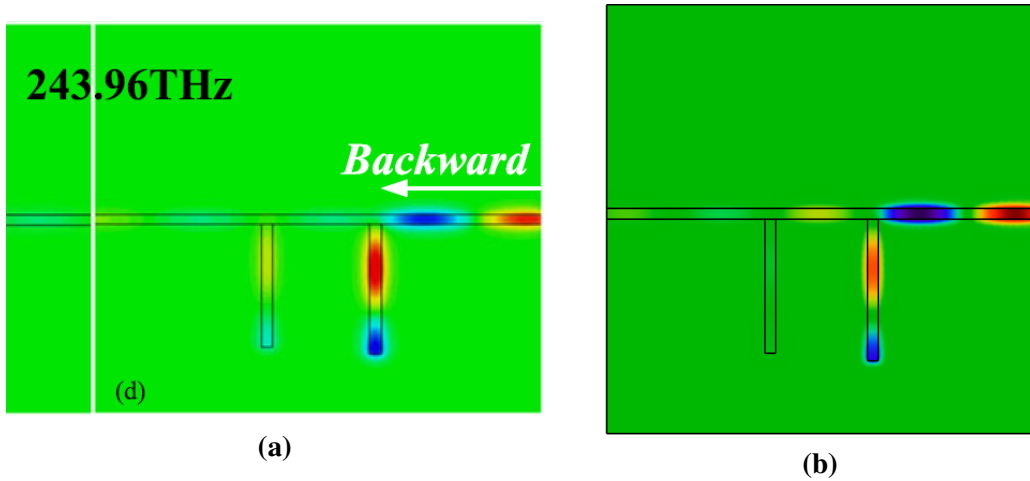


Figure 4.18: H_z field (a) by Zhang *et al.* [102] and (b) resimulation.

For further validation, the H_z field of the re-simulated structure for backward transmission is obtained fig. 4.18b at 243.96 THz. The obtained profile replicates the original work fig. 4.18a and corroborates the computational accuracy of COMSOL Multiphysics.

4.4.3 Butt *et al.*

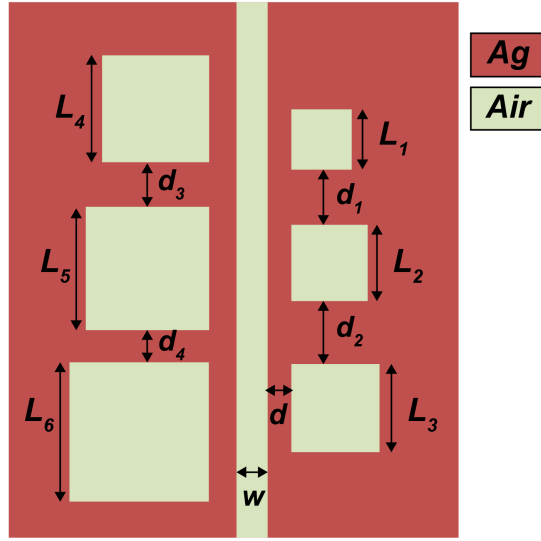


Figure 4.19: Schematic diagram of plasmonic filter proposed by Butt *et al.* [52]

Figure 4.19 represents a MIM based plasmonic filter with multiple cavities of Butt *et al.*, titled "A plasmonic colour filter based on metal-insulator-metal square micro-ring cavities for visible spectrum," published in *Proceedings of SPIE*. Figure 4.19 represents the schematic design proposed by Butt *et al.* Table 4.3 presents the values of the parameters [52]. However, the values of the distance between each cavity, d_1 , d_2 , d_3 , and d_4 are unknown. Therefore, these four values have been arbitrarily chosen.

Table 4.3: Geometric parameters of the structure [52].

Parameters	Denoted symbol	Value	Unit
Length of first cavity	$L1$	125	nm
Length of second cavity	$L2$	150	nm
Length of third cavity	$L3$	165	nm
Length of fourth cavity	$L4$	200	nm
Length of fifth cavity	$L5$	210	nm
Length of sixth cavity	$L6$	225	nm
Distance	d	50	nm
Width of waveguide	w	100	nm

The 2D view and triangular mesh view of the re-simulated sensor are illustrated in fig. 4.20a and fig. 4.20b, respectively.

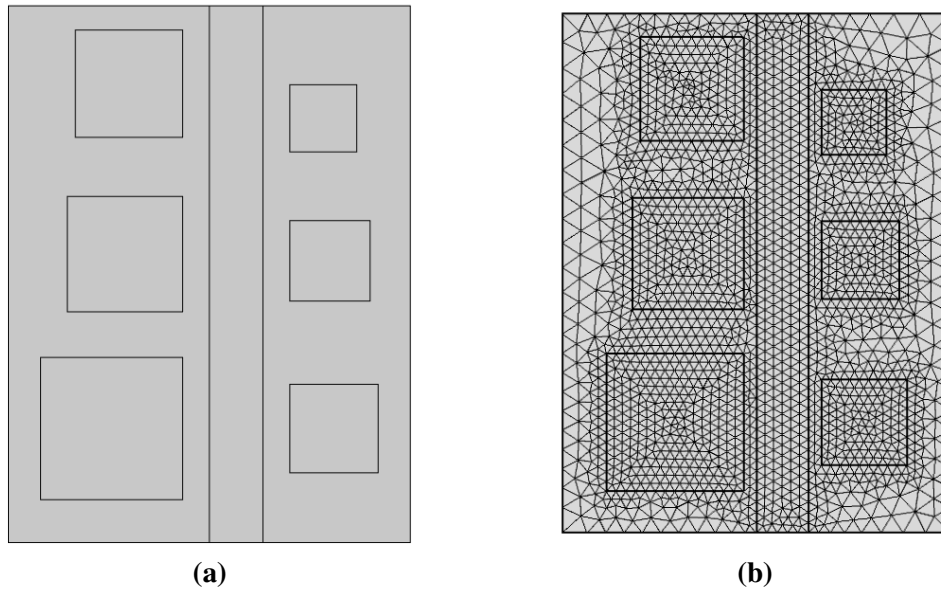


Figure 4.20: (a) 2D view of the resimulated filter. (b) Triangular mesh view of the resimulated filter.

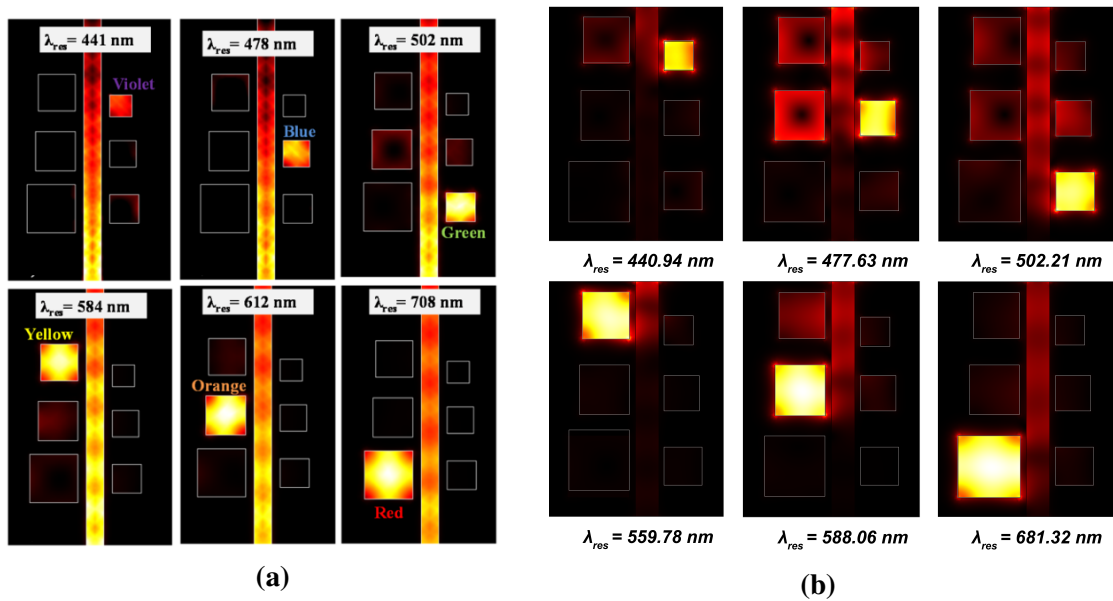


Figure 4.21: *E*-field confinement in MIM waveguide μ -ring cavities (a) depicted by Butt *et al.* [52] and (b) for the resimulated sensor.

Figure 4.21a and fig. 4.21b represent the *E*-field confinement in MIM waveguide μ -ring cavities by Butt *et al.* and in re-simulation. Comparing the resonance wavelengths stated in fig. 4.21a and fig. 4.21b, it is evident that the re-simulation can replicate three resonance wavelengths and demonstrates the accuracy of COMSOL Multiphysics. If the values of $d_1 - d_4$ are known, this paper can be completely replicated.

Chapter 5

Modeling, Optimization and Numerical Analysis of the Proposed Sensors

This section illustrates the designing, optimization, fabrication, and applications of three refractive index sensors. The proposed sensors aim to fulfill the need for high sensitivity and FOM required for various plasmonic applications.

5.1 Sensor Design with CDRR

5.1.1 Sensor Layout and Theoretical Analysis

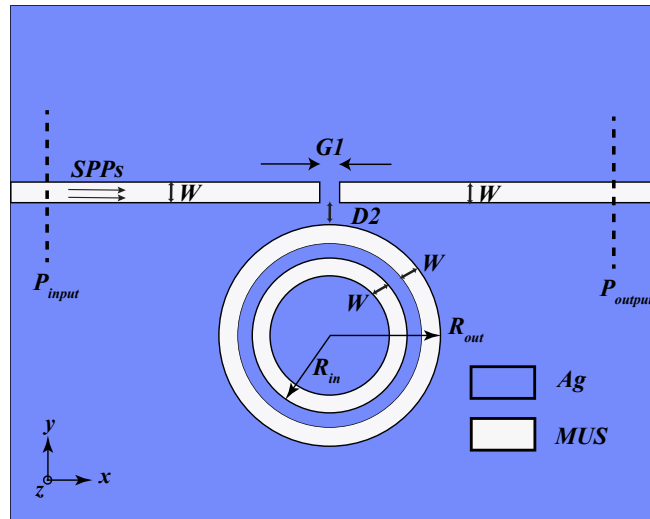


Figure 5.1: Two-dimensional model of the proposed sensor.

The 2D configuration of the proposed sensor is given in fig. 5.1. The nanosensor setup consists of a MIM waveguide with a baffle in the middle and a vertically coupled concentric double-ring resonator (CDRR). Table 5.1 lists the preliminary parameters used in the 2D modeling of the proposed schematic. The white color in fig. 5.1 represents the material under sensing (MUS), which is filled within the cavities and cores of the waveguide. Similarly, the blue color in the schematic denotes silver.

Table 5.1: Preliminary 2D modeling parameters.

Parameter	Symbol	Value (nm)
Width of the setup	W	20
Baffle	$G1$	25
Distance between outer ring and baffle	$D2$	20
Outer radius	R_{out}	150
Inner radius	R_{in}	110

The width of the waveguide is set to 20 nm to fundamental ensure TM polarized SPPs [41]. The dispersion relation of the fundamental TM mode in a MIM system can be expressed as [103],

$$\varepsilon_{ins} \times \alpha = (\varepsilon_{met} \times \kappa) \times (1 - e^{\kappa W} / 1 + e^{\kappa W}), \quad (5.1)$$

$$\alpha = \kappa_0 \times \sqrt{(\beta_p / \kappa_0)^2 - \varepsilon_{met}}, \kappa = \kappa_0 \times \sqrt{(\beta_p / \kappa_0)^2 - \varepsilon_{ins}}, \quad (5.2)$$

$$\beta_p = \eta_{eff} \times \kappa_0 = \eta_{eff} \times 2\pi / \lambda, \quad (5.3)$$

where, W indicates the width of the waveguide, ε_{ins} and ε_{met} are the relative permittivity of insulator and metal, respectively, λ is the wavelength of incident light, κ_0 is the wavenumber, β_p is the propagation constant, and η_{eff} is the effective refractive index.

Commercial EM simulator COMSOL Multiphysics is used to simulate the proposed sensor, which utilizes the Finite Element Method (FEM). The FEM can design EM wave problems with accurate material interfacing, accelerated convergence, adaptive meshing, and high numerical resolution [104]. During the simulation, two monitors named P_{input} and P_{output} are placed at the input and output side to measure SPP power flows and calculate transmittance (T), defined by $T = P_{output} / P_{input}$ [97].

5.1.2 Sensing Technique and Performance Criteria of an RI Sensor

Mathematically, refractive index (η) can be expressed as [98],

$$\eta = c / c_1, \quad (5.4)$$

where, c = speed of light in vacuum, and c_1 = speed of light in a sensing medium. Now,

$$c = f\lambda_0, c_1 = f\lambda_1, \quad (5.5)$$

where, λ_0 and λ_1 are the related wavelengths for c and c_1 while f being the frequency. Therefore,

$$\eta = c/c_1 = f\lambda_0/f\lambda_1 = \lambda_0/\lambda_1, \quad (5.6)$$

$$\therefore \eta \propto 1/\lambda_1 [\because \lambda_0 = \text{constant}]. \quad (5.7)$$

Thus, a change in the refractive index shifts the resonant wavelength to a new position. Inserting MUS within the proposed RI nanosensor similarly moves the location of the resonant wavelength of the system. Different materials have distinct resonant wavelengths. Hence, the MUS can easily be identified by observing the shifted wavelength.

5.1.3 Initial Simulation Results and Discussion

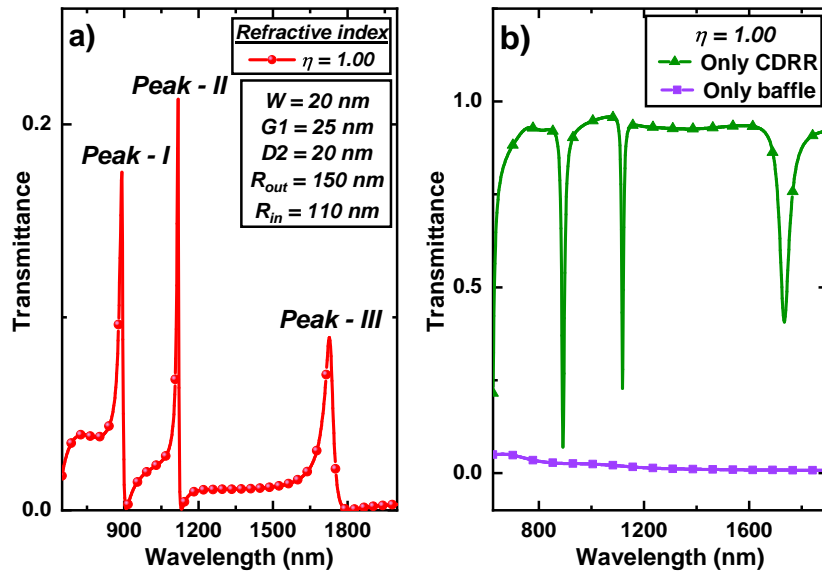


Figure 5.2: a) Initial transmittance spectrum. b) Formation of Fano peaks.

Considering $\eta = 1.00$ as the MUS, the nanosensor setup is simulated with the following initial structural parameters (table 5.1). Figure 5.2a illustrates the transmittance spectrum of the initial simulation. Three resonant peaks occur at 890.9 nm (*Peak-I*), 1117.31 nm (*Peak-II*), and 1727.81 nm (*Peak-III*). Furthermore, the sharp, asymmetrical profile of the peaks indicates the presence of Fano resonance.

The Fano resonance in the structure can be understood from fig. 5.2b, which plots the transmittance profiles of the modeled sensor considering the presence of CDRR and baffle, one at a time. When the structure contains only baffle and no CDRR, a reflection phenomenon (broadband resonance) occurs in the device. Similarly, when the sensor arrangement contains only CDRR, SPPs flow freely from the input to the output (narrowband resonance). Thus, in the presence of both CDRR and baffle, narrowband resonance interferes with the broadband resonance and hinders the flow of SPPs to the

output by disturbing the phase and the amplitude. The interaction between these two different resonances generates the Fano peaks in fig. 5.2a [106].

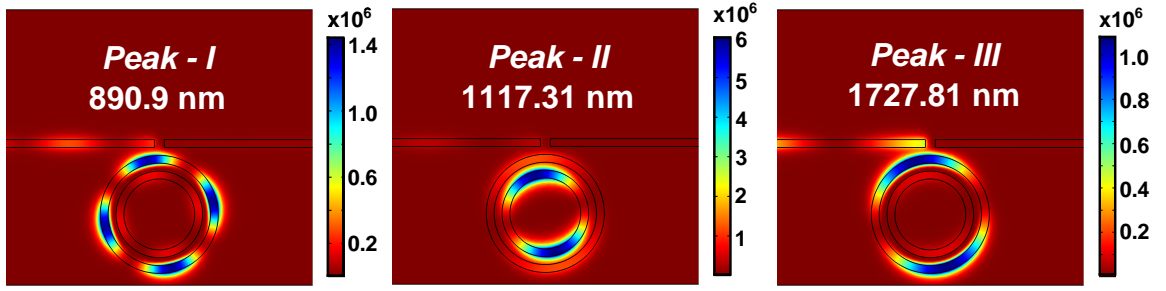


Figure 5.3: $|H_z|^2$ field distribution for the presented MIM sensor.

The Fano resonance phenomenon can also be explained by the $|H_z|^2$ field distribution of the proposed sensor given in fig. 5.3. Figure 5.3 displays that the majority of the resonance energy is trapped within the inner and outer ring. The field distributions exhibit reduced transmission of SPPs to the output port. Thus, the peaks in fig. 5.2a have considerably low transmittance. Moreover, the trapped resonance energy causes the transmittance value to drop suddenly from crest to trough, resulting in sharp, asymmetric Fano profiles [101].

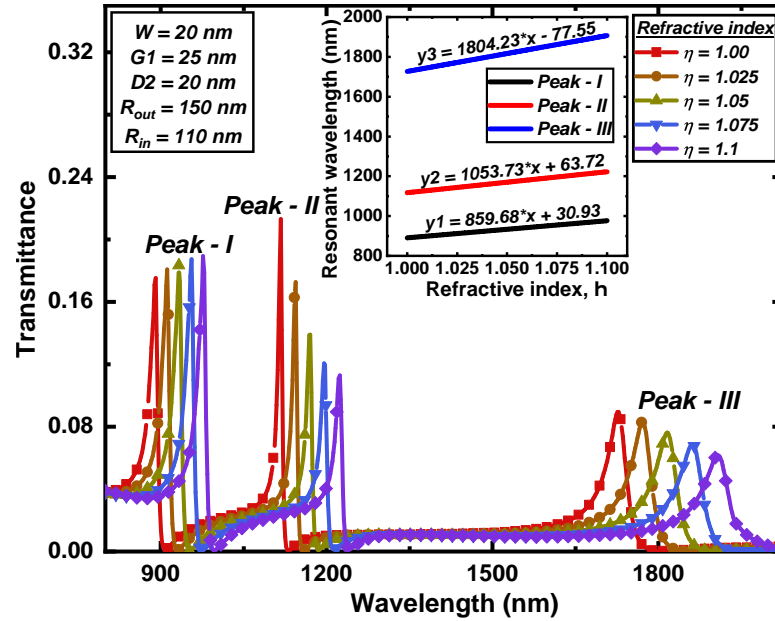


Figure 5.4: Transmittance spectra for variation of refractive index, η .

The refractive index (η) of the MUS is then varied from 1.00 to 1.10, with a step-size of 0.025 to obtain the sensitivity of the proposed scheme. With increasing η , all three peaks experience redshift (fig. 5.4), and *Peak-I*, *Peak-II*, and *Peak-III* attain sensitivity of 859.68 nm/RIU, 1053.73 nm/RIU, and 1804.23 nm/RIU, respectively. Thus, *Peak-III* is the most suitable peak for sensing tasks. Inset of fig. 5.4 plots the

sensitivity of the peaks as slopes and demonstrates a linear relationship between the resonant wavelength and η .

5.1.4 Maximizing Sensitivity through Optimization

The structural parameters of an RI sensor can be varied and fine-tuned to extract the optimal sensitivity. Optimization of structural parameters enables researchers to discover the most sensitive geometry and maximize the sensing capacity of an RI sensor. Therefore, optimization is performed on the suggested nanosensor.

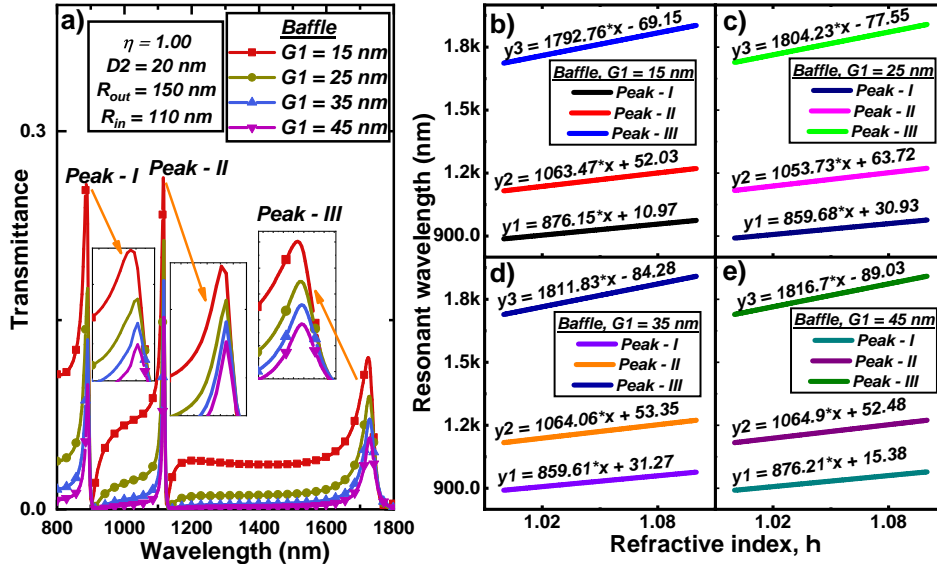


Figure 5.5: a) Transmittance spectra for varying $G1$. b) – e) Resonant wavelength vs. Refractive index graphs for different values of $G1$.

The baffle $G1$ is first varied from 15 nm to 45 nm, with a 10 nm step-size while keeping the other parameters fixed at initial values. Figure 5.5a demonstrates that the variation of $G1$ causes a minute shift of the three peaks towards longer wavelengths. Figure 5.5b to fig. 5.5e plot the resonant wavelength vs. refractive index graphs for different values of $G1$. Figure 5.5e exhibits that for $G1 = 45$ nm, all three peaks have maximum sensitivity ($Peak-I = 876.21$ nm/RIU, $Peak-II = 1064.9$ nm/RIU, $Peak-III = 1816.7$ nm/RIU). Thus, the optimized value of $G1$ is 45 nm.

Inner radius R_{in} is next varied for optimization from 104 nm—113 nm with a step-size of 3 nm. Figure 5.6a to fig. 5.6d show that a prominent redshift occurs for all the peaks for increasing values of R_{in} . Therefore, R_{in} is a vital tuning parameter of the designed sensor. For $R_{in} = 113$ nm, $Peak-I$, $Peak-II$, $Peak-III$ have the highest sensitivity of 911.706 nm/RIU, 1105.67 nm/RIU, and 2818.49 nm/RIU, respectively (fig. 5.6h). As a result, R_{in} is updated to 113 nm.

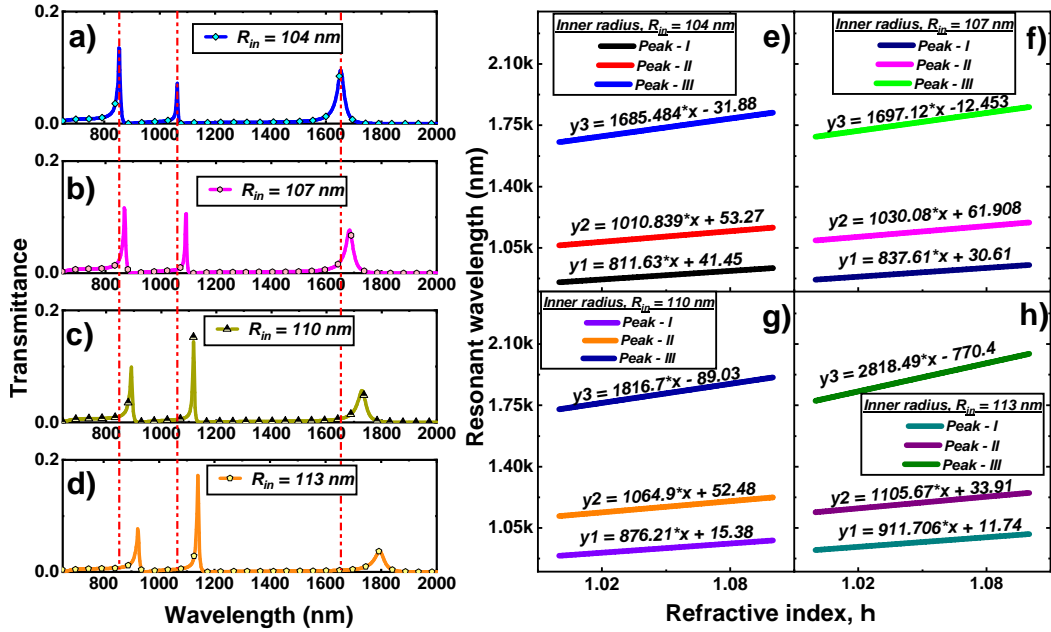


Figure 5.6: a) – d) Transmittance spectra for varying R_{in} . e) – h) Resonant wavelength vs. Refractive index graphs for various values of R_{in} .

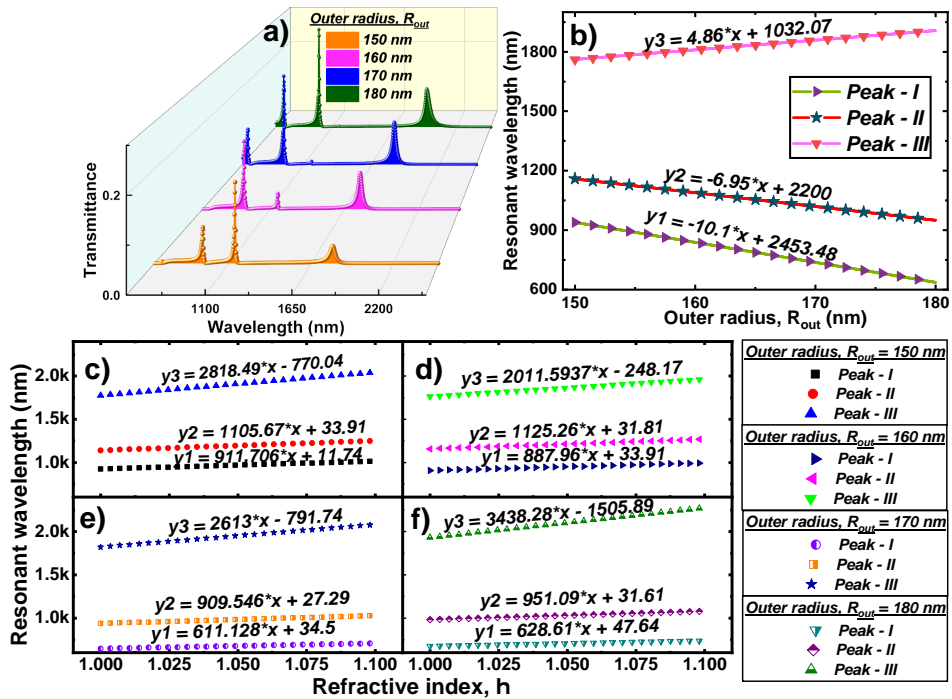


Figure 5.7: a) Transmittance spectra for varying R_{out} . b) Resonant wavelength vs. R_{out} graph. c) – f) Resonant wavelength vs. Refractive index graphs for different values of R_{out} .

Figure 5.7a illustrates the transmittance spectra for the outer radius R_{out} , ranging from 150 nm—180 nm with a step-size of 10 nm. With increasing R_{out} , *Peak-I* and *Peak-II* experience significant blueshift, while *Peak-III* experiences notable redshift. The statement mentioned above is further justified from the steep positive slope of *Peak-III* and steep negative slopes of *Peak-I* and *Peak-II* in fig. 5.7b. Therefore, R_{out}

is another sensitive parameter of the proposed nanosensor. The sensitivity of *Peak-I*, *Peak-II*, *Peak-III* are maximized for R_{out} being 150 nm (911.706 nm/RIU), 160 nm (1125.26 nm/RIU), and 180 nm (3438.28 nm/RIU), respectively (fig. 5.7c, d, f). The sensitivity of *Peak-III* increases noticeably from the previous step of the iteration among all the peaks. Thus, *Peak-III* is prioritized for enhancing the sensitivity of the presented RI sensor, and R_{out} is set to 180 nm. Consequently, *Peak-I* and *Peak-II* have a new sensitivity of 628.61 nm/RIU and 951.09 nm/RIU, respectively.

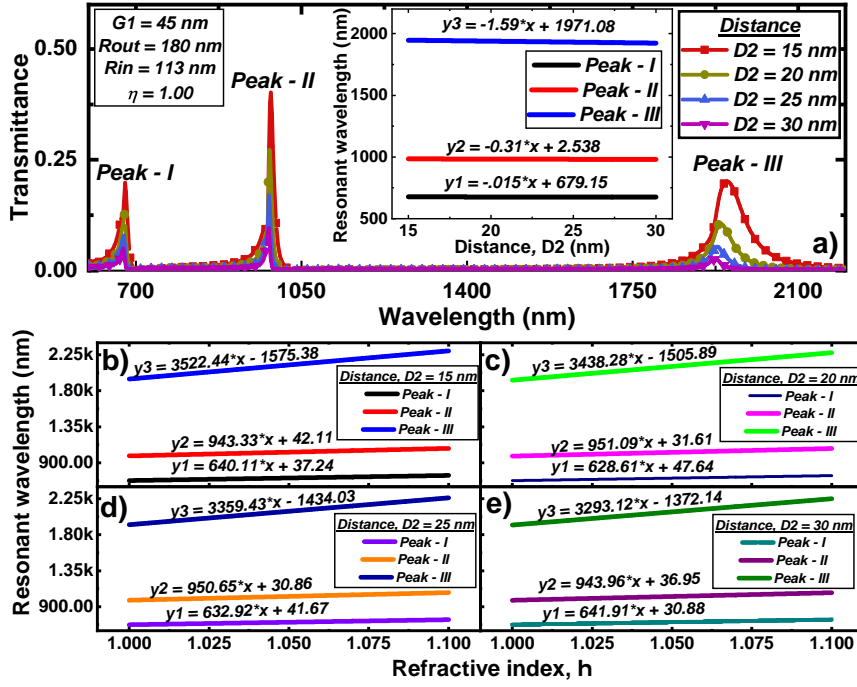


Figure 5.8: a) Transmittance spectra for varying D_2 . b) – e) Resonant wavelength vs. Refractive index graphs for different values of D_2 .

Figure 5.8a displays that when the distance between the outer ring and baffle D_2 is increased from 15 nm to 30 nm, with an interval of 5 nm, the peaks slightly shift towards shorter wavelengths (negative slopes in the inset). Since *Peak-III* is given preference in the previous step of optimization, when $D_2 = 15$ nm, *Peak-III* obtains the highest sensitivity of 3522.44 nm/RIU (fig. 5.8b). Therefore, the optimized value of D_2 is 15 nm. Moreover, *Peak-I* and *Peak-II* have the updated sensitivity of 640.11 nm/RIU and 943.33 nm/RIU, respectively.

Table 5.2 sums up the whole optimization process of the structural parameters and provides a sensitivity comparison of the peaks. From the tabular analysis, *Peak-III* had an initial sensitivity of 1804.23 nm/RIU. The sensitivity of *Peak-III* increases by $\approx 95.23\%$ after the optimization process. Therefore, *Peak-III* is the most suited peak for RI sensing, enabling the designed sensor to precisely detect the MUS. Additionally, the optimized model of the nanosensor outperforms the recent works of RI sensors [41–45].

Table 5.2: The synopsis of the optimization process.

Parameter	Initial value (nm)	Initial sensitivity (nm/RIU)			Optimized Value (nm)	Sensitivity after optimization (nm/RIU)		
		Peak-I	Peak-II	Peak-III		Peak-I	Peak-II	Peak-III
Baffle, $G1$	25	859.68	1053.73	1804.23	45	876.21	1064.9	1816.7
Inner radius, R_{in}	110	876.21	1064.9	1816.7	113	911.706	1105.67	2818.49
Outer radius, R_{out}	150	911.706	1105.67	2818.49	180	628.61	951.09	3438.28
Distance, $D2$	20	628.61	951.09	3438.28	15	640.11	943.33	3522.44

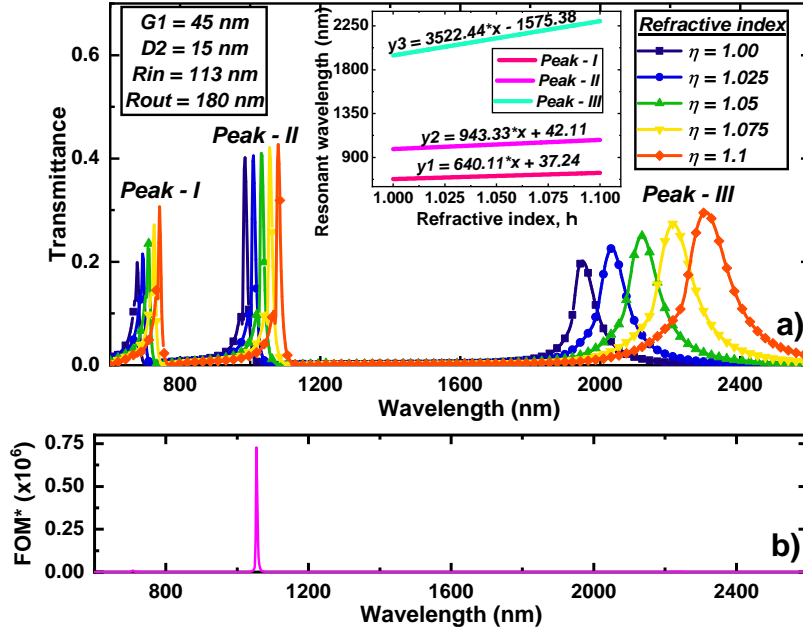


Figure 5.9: a) Transmittance spectra for optimized structural parameters. b) FOM^* of the proposed sensor.

Figure 5.9a plots the transmittance versus wavelength graph for the optimized structural parameters. The resonant peaks shift towards longer wavelengths as the refractive index, η , is varied from 1.00 to 1.1, with a step-size of 0.025. Inset of Figure 5.9a plots the resonant wavelength positions with increasing RI and generates steep, positive slopes as the sensitivity of the peaks. Furthermore, *Peak-I*, *Peak-II*, *Peak-III* have a FOM of 38.4, 80.07, and 51.01, respectively. The FOM^* of the optimized nanosensor is 0.73×10^6 (fig. 5.9b).

5.1.5 Fabrication

The fabrication of the proposed sensor is easily achieved using the nanoimprint lithography (NIL) technique. Figure 5.10 illustrates the whole fabrication process, considering silicon wafer as the substrate. At first, the imprinting is done by pressing a stamp over the resin. The residual layer of the resin is then removed by O_2 plasma etching. In the third step, electron beam evaporation deposits a layer of silver over the sili-

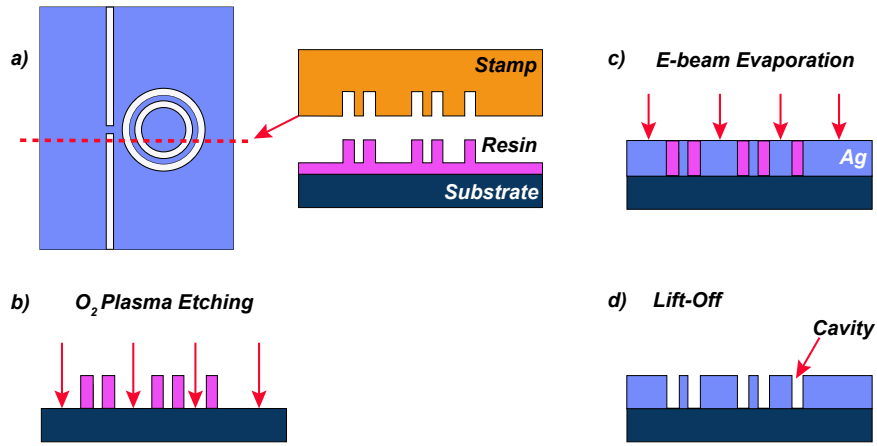


Figure 5.10: Fabrication of the suggested sensor using nanoimprint lithography.

con wafer. Finally, the pattern transfer is fully complete through the lift-off process, eliminating the resin imprints and forming the desired cavities [31]. The NIL fabrication process offers low-cost implementation with mass producibility, better throughput, and massive chip-scale integration, making it suitable for academic and industrial use. Though most literature on refractive index sensors employs the electron beam lithography (EBL) and the focused ion beam (FIB) techniques for fabricating the sensors, these procedures are expensive and have low-output, limiting their practical use [105].

5.1.6 Detection of Cancer Cells

The suggested optimized RI sensor can be used to detect cancer biomarkers in the early stages exploiting its high sensitivity. The abnormal value of the refractive index of the cytoplasm in the cell is one such critical biomarker. Healthy cells contain cytoplasm with an RI value of 1.36, whereas the RI range of the cancerous cytoplasm falls within 1.38 to 1.401. The presence of excess protein in cancerous cells causes such a high value of the cytoplasmic refractive index [107], [108], [109].

The cancer cells are usually in the μm range [107]. Thus, an entire cell cannot be inserted within the proposed nanosensor for cancer detection. However, different cell parts, such as nuclear and cytoplasm, can be extracted through standard centrifugation techniques. The extracted cytoplasmic fluid can then be poured into the cavities and waveguide-cores of the nanosensor and tested for cancer detection [108].

Figure 5.11a and fig. 5.11b demonstrate the transmittance spectra and the resonant wavelength versus refractive index graph among a normal cell and six types of cancer cells for the most sensitive peak of the optimized model, respectively. The distinct slopes in the inset of fig. 5.11b enable the designed structure to distinguish between the healthy and cancer cells accurately. Table 5.3 lists the sensitivity values for each cancerous sample. Such high sensitivity for each cancer cell makes the proposed de-

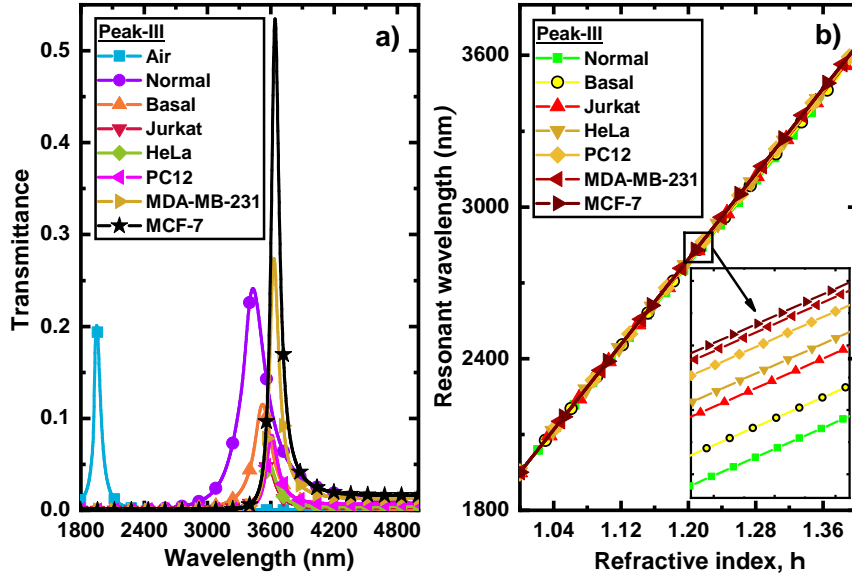


Figure 5.11: a) Transmittance spectra for cancer detection. b) Resonant wavelength vs. Refractive index graphs for different cancer cells.

Table 5.3: Performance of the proposed optimized sensor as a cancer cell detector [107], [108], [109].

Cell	Affected area	Refractive Index, η	Sensitivity (nm/RIU)
Normal	-	1.360	4116.94
Basal	Skin	1.380	4140.07
Jurkat	Blood	1.390	4169.25
HeLa	Cervix	1.392	4180.34
PC12	Adrenal Glands	1.395	4200.47
MDA-MB-231	Breast	1.399	4211.55
MCF-7	Breast	1.401	4217.61

sign a potential cancer nanosensor. From table 5.3, the modeled nanosensor can offer a minimum DL of 2.37×10^{-7} RIU.

5.1.7 Chemical Sensing

The various mixtures of glucose-ethanol-water can be represented with distinct refractive index values [110]. Thus, the RI sensor can be employed to sense the concentration of the solutes utilizing the linear association between the refractive index and the corresponding resonant wavelength shift.

The waveguide-cores and the cavities of the proposed optimized sensor are filled with different aqueous solutions of glucose-ethanol for chemical sensing. Figure 5.12a plots the transmittance vs. wavelength graph for four solutions considering *Peak-III*. From fig. 5.12b, sensitivity of the solutions are calculated and then listed in table 5.4. The tabular analysis demonstrates that the designed sensor offers a great sensitivity

ranging from 4087.44 nm/RIU to 4092.7 nm/RIU for the solutions. Thus, the presented schematic can effectively sense the concentrations of glucose and ethanol and determine the purity of the solution.

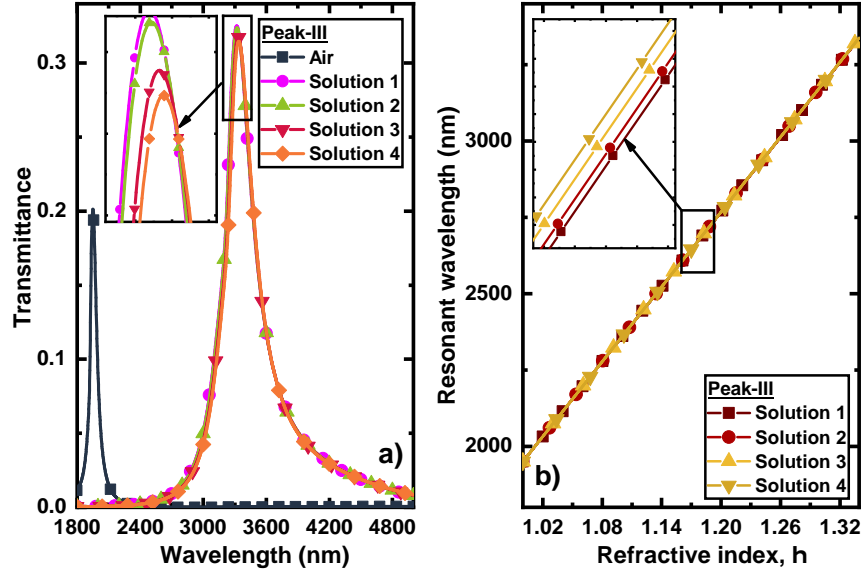


Figure 5.12: a) Transmittance spectra for chemical sensing. b) Resonant wavelength vs. Refractive index graphs for different solutions.

Table 5.4: Performance of the proposed optimized device as a chemical sensor [110].

Sample (100 mL)	Concentration		Refractive Index, η	Sensitivity (nm/RIU)
	Glucose (g/dL)	Ethanol (mL/dL)		
Solution 1	0.5	2.3	1.3351	4087.44
Solution 2	1.1	2.2	1.3357	4088.69
Solution 3	3	1.2	1.3381	4090.75
Solution 4	4.1	0.3	1.3393	4092.7

Unadulterated aqueous solutions of glucose-ethanol are used in many chemical processes, i.e., fermentation, preservation of fruit, extraction of liquid-solid, and many more [111]. Hence, the proposed RI sensor can be implemented in the chemical reactions mentioned above and determine the level of adulteration in glucose-ethanol-water mixtures by sensing the solute concentrations.

5.1.8 Bandpass filter

The Q -factor for *Peak-I*, *Peak-II*, *Peak-III* at optimized structural parameters are 40.63, 83.65, and 28.24, respectively. Since all the peaks display high Q -factor, the modeled sensor can be deployed as a nanoplasmonic triple-channel bandpass filter.

5.2 Sensor Design with Multiple Rings

5.2.1 Sensor Geometry and Theoretical Background

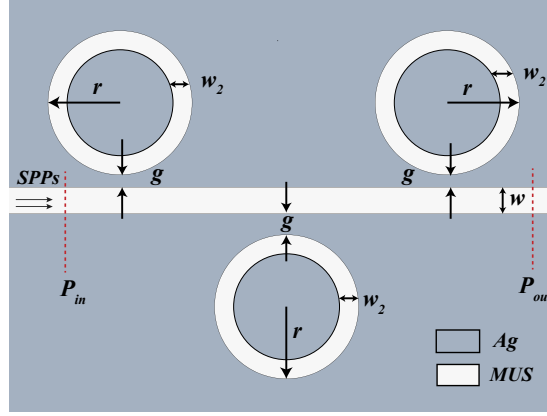


Figure 5.13: Schematic diagram of the proposed nanosensor.

The proposed structure consists of three circular rings, coupled with a straight MIM waveguide, as illustrated in fig. 5.13. The model employs a two-dimensional design, where the grey and white regions represent silver (Ag) and the material under sensing (MUS), respectively. Silver is chosen since it has the smallest imaginary value of relative permittivity, within the near-infrared (NIR) region [112]. The 2D structure is simulated in COMSOL Multiphysics Software utilizing the finite element method (FEM). The scattering boundary conditions are set at the boundaries of the sensor to absorb the eluding EM-field energy. The initial simulation parameters are shown in table 5.5.

Table 5.5: Initial simulation parameters.

Dimensions	Symbol	Value (nm)
Width of straight waveguide	w	55
Distance between ring and straight waveguide	g	20
Outer radius	r	240
Width of rings	w_2	45

The fundamental transverse magnetic (TM_0) mode, maintained in the MIM waveguides, can be expressed as [113],

$$\tanh(kw) = \frac{-2kp\alpha_c}{(k^2 + p^2 + \alpha_c^2)}, \quad (5.8)$$

where, $k = 2\pi/\lambda$ is the wave vector in the waveguide, w is the width of the waveguides, $p = \varepsilon_i/\varepsilon_m$ (ε_i and ε_m are the permittivity of the insulator and metal, respectively), and $\alpha_c = \sqrt{[k_0^2(\varepsilon_i - \varepsilon_m) + k^2]}$.

The transmittance (T) is established as $T = (S_{21})^2$, where S_{21} is the transmission coefficient from input port P_{in} to output port P_{out} . According to standing wave theory, the resonant wavelength can be defined as [114],

$$\lambda_{res} = \frac{2Re(n_{eff})L}{m - \Psi/2\pi}, \quad (5.9)$$

$$Re(n_{eff}) = \sqrt{\varepsilon_m + \left(\frac{k}{k_0}\right)^2}, \quad (5.10)$$

where, L is the perimeter of the ring, $Re(n_{eff})$ represents the real part of the effective refractive index of the MUS, k_0 is the wave vector in free space, m is the positive mode integer ($m = 1, 2, \dots$), and Ψ is the phase shift due to reflection from the rings, respectively.

5.2.2 Simulation Results and Discussion

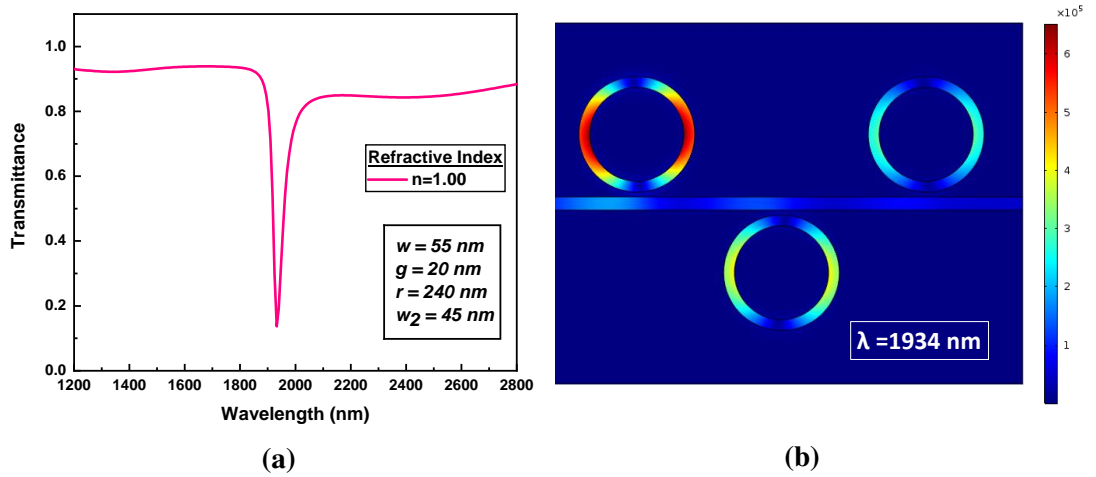


Figure 5.14: (a) Transmission spectrum at $n = 1.00$. (b) The E-field distribution at the corresponding resonant wavelength.

Figure 5.14a shows the transmittance profile of the sensor over the wavelength range of 1200 nm to 2800 nm at refractive index (n) of 1.00. Considering the initial device specifications in table 5.5, the transmittance curve exhibits a fano dip at a resonant wavelength of $\lambda = 1934 \text{ nm}$, with a narrow FWHM of 44.5 nm. Furthermore, the electric field (E-field) distribution along the propagation direction at $\lambda = 1934 \text{ nm}$ is provided in fig. 5.14b.

To get a clear perception of the significance of different RI media on the transmission spectra, the refractive index (n) of the insulator is varied from 1.00 to 1.10, with a step size of 0.025. A redshift is observed with increasing the value of n (fig. 5.15a). Moreover, the refractive index and resonant wavelength demonstrate a linear relation-

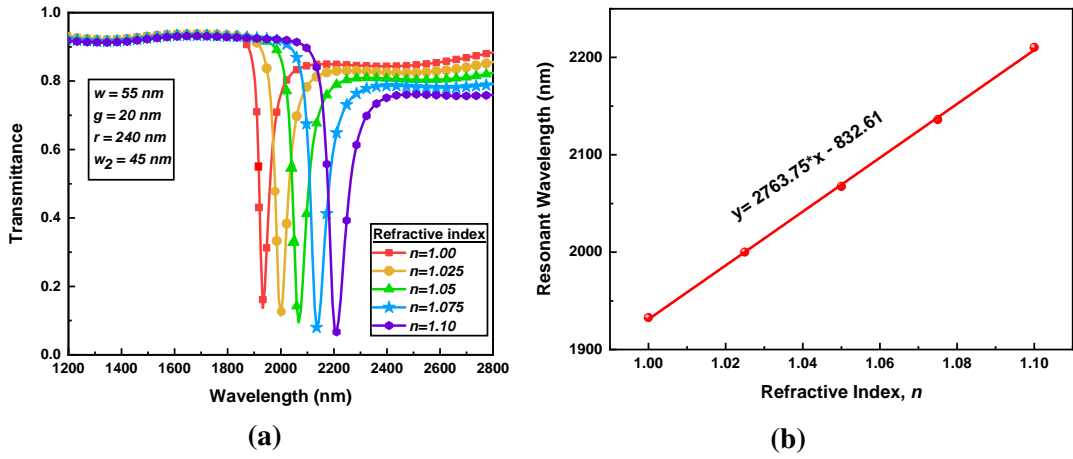


Figure 5.15: (a) Transmission spectra at varying refractive index (n). (b) Relationship between resonant wavelength and refractive index.

ship as shown in fig. 5.15b, where the positive slope implies a sensitivity of 2763.75 nm/RIU. Furthermore, FOM of 62.1 is obtained.

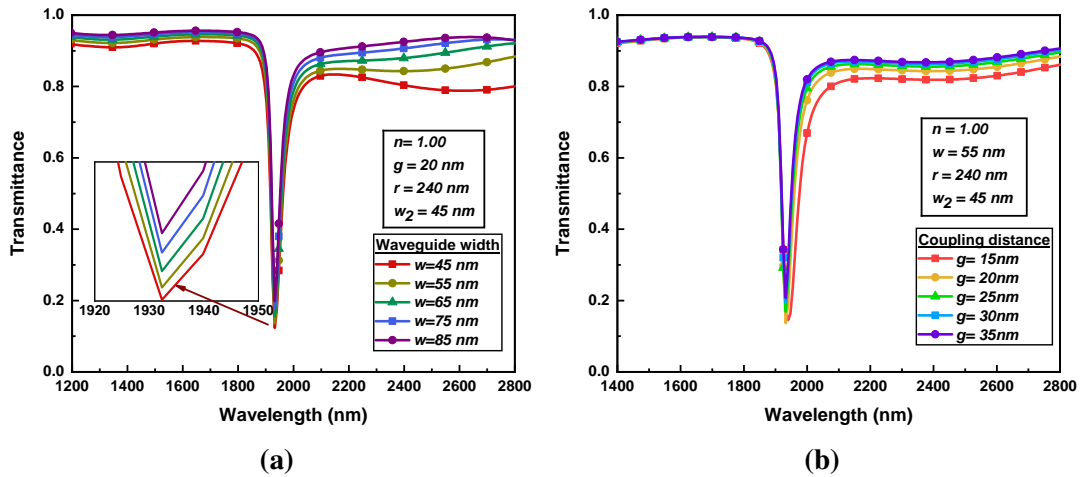


Figure 5.16: (a) Transmission spectra of the waveguide with changing width of the waveguide (w). (b) Transmission spectra at varying coupling distance (g).

Diverse structural parameters have a fundamental effect on the Fano resonances. At first, the width of the straight waveguide w is varied, to assess any significant change on the spectrum. Keeping the other parameters fixed, w is increased from 45 nm to 85 nm, with a stepsize of 10 nm. A slight blueshift occurs in the resonant wavelength as depicted in the inset of fig. 5.16a, which has a negligible effect on the performance of the sensor.

The effects of coupling distance g between the straight waveguide and the rings are then studied. The coupling distance is increased from 15 nm to 35 nm, with an interval of 5 nm. From fig. 5.16b, an insignificant change is observed in the resonant wavelengths as they are overlapping.

Subsequently, the outer radius of the rings r is increased from 160 nm to 240 nm

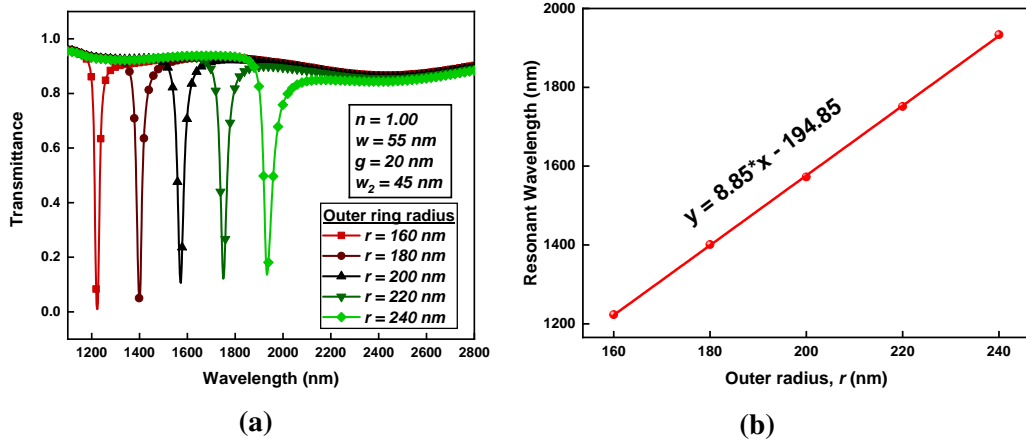


Figure 5.17: (a) Transmission spectra of the waveguide with changing outer radius (r). (b) Relationship between resonant wavelength and outer radius of the rings.

with a 20 nm stepsize, and the transmittance profile in fig. 5.17a displays a noticeable redshift. The linear correlation between the resonant wavelength and r is presented in fig. 5.17b, which states a 8.85 nm shift in resonant wavelength for per unit change in the outer radius.

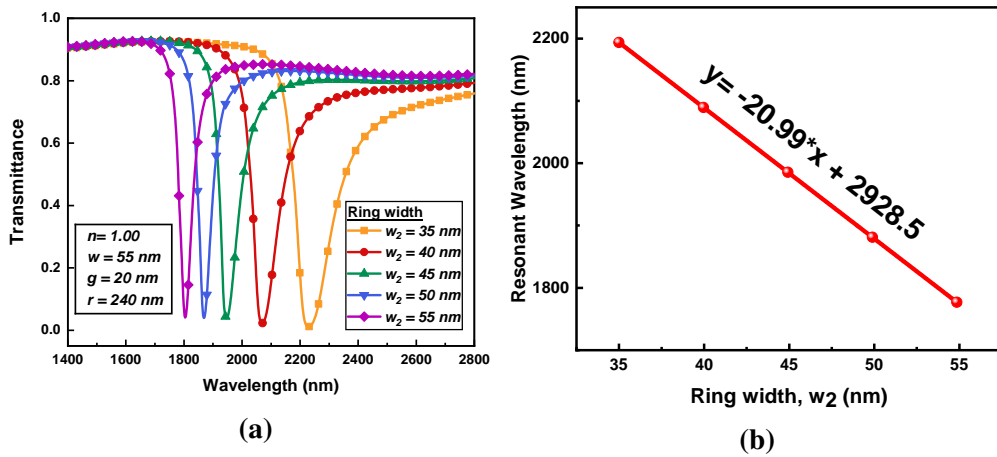


Figure 5.18: (a) Transmission spectra of the waveguide with changing width of the ring (w_2). (b) Relationship between resonant wavelength and width of the rings.

In fig. 5.18a, the width of the ring waveguide w_2 is changed from 35 nm to 55 nm, with a 5 nm stepsize. The transmittance dip demonstrates a substantial blueshift. Figure 5.18b plots the linear relation between resonant wavelength and ring width with a 20.99 nm change in resonant wavelength for per unit change in ring width. Hence, w_2 is a vital tuning parameter for the proposed structure.

After extensive simulations, the measurement of the proposed structure that employs the best possible result is summarized in table 5.6. The sensor had an initial sensitivity of 2763.75 nm/RIU. Figure 5.19a plots the transmittance profile of the optimised schematic, where RI changes from 1.00 to 1.10, with a stepsize of 0.025.

Table 5.6: The most sensitive structural parameters of the proposed sensor.

Dimensions	Initial value (nm)	Initial sensitivity (nm/RIU)	Final value (nm)	Final sensitivity (nm/RIU)
w	55		45	
g	20	2763.75	15	3573.3
r	240		240	
w_2	45		35	

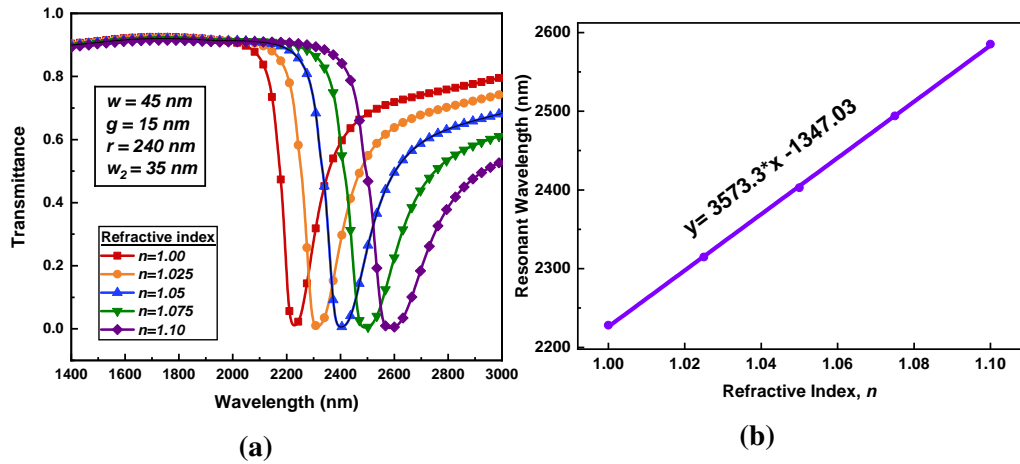


Figure 5.19: (a) Transmittance profile of the structure with final parameters. (b) Relationship between resonant wavelength and refractive index.

The resonant wavelength exhibits a redshift with the change in refractive index. Figure 5.19b plots a positive, linear relationship between the resonant wavelength and refractive index. Tuning the parameters enhances the sensitivity by 29.3%. Thus, the designed sensor achieves a final sensitivity of 3573.3 nm/RIU and FOM of the design is 21.9. Moreover, $Q\text{-factor} = \lambda_{\text{resonant}}/\text{FWHM}$ of the proposed sensor is calculated as 13.6.

5.2.3 Fabrication

The proposed schematic encompasses the nanoimprint lithography (NIL) technique (fig. 5.20), in which the silicon stamp imprints the multi-ring pattern on the resin. O_2 plasma etching extracts resin residues from the silicon substrate, followed by electron beam evaporation that effectively deposits the silver layer on the substrate. Lastly, the lift-off technique eliminates the resin imprint and successfully transfers the stamp pattern [115]. The NIL is a low-cost popular technique exploited in the fabrication of high-precision nanostructures.

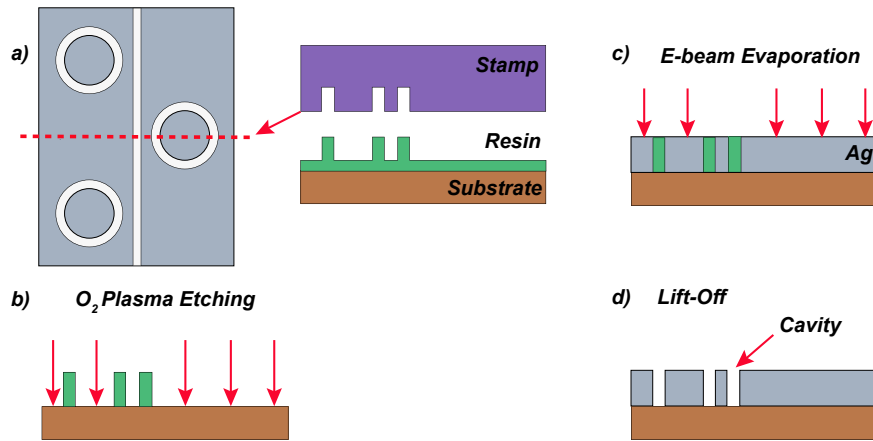


Figure 5.20: NIL fabrication process of the proposed structure.

5.2.4 Fabrication Error Tolerance

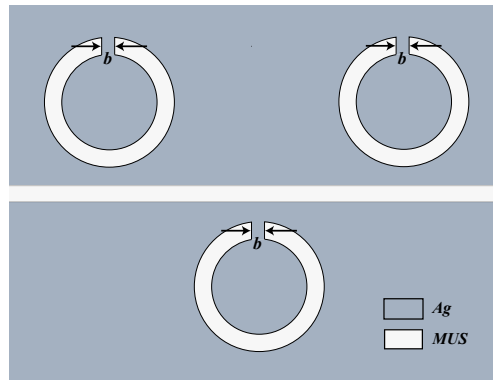


Figure 5.21: Proposed nanosensor with slits on the rings.

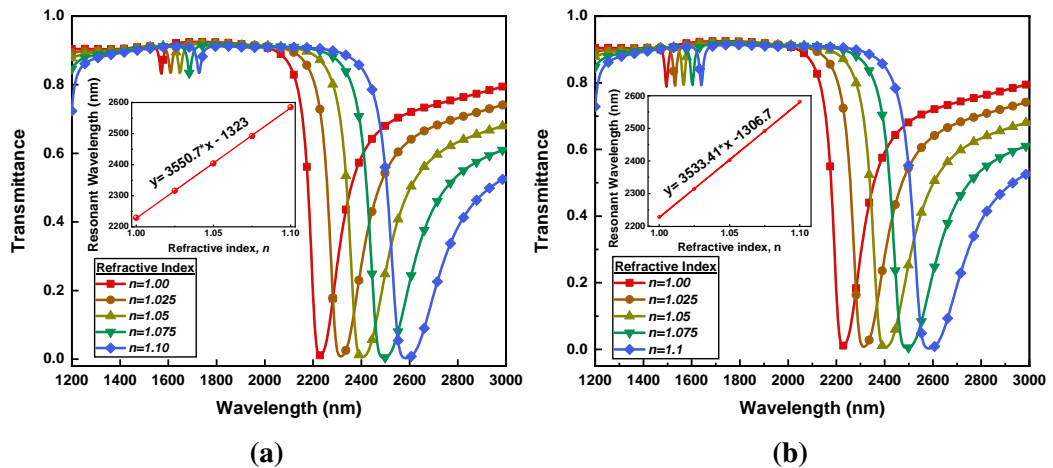


Figure 5.22: Transmission spectra at slit width of (a) 5 nm and (b) 10 nm.

During the fabrication of plasmonic structures in nanoscale, there is a probability of some defects occurring within the sensor. Thus, to analyze the tolerance of the

sensor, three slits of equal width b is introduced on each ring, as depicted in fig. 5.21.

Figure 5.22a and fig. 5.22b show the transmittance versus wavelength graph of the sensor for a slit width of 5 nm and 10 nm, respectively. Both graphs demonstrate a resonant peak shift from left to right with an increasing refractive index. The inset graphs show the linear relation between resonant wavelength and the refractive index of the sensor. The highest sensitivity of 3550.7 nm/RIU and 3533.41 nm/RIU are achieved for 5 nm and 10 nm slits, respectively.

Table 5.7: Sensitivity analysis for slit width b .

Slit Width b (nm)	Sensitivity (nm/RIU)	Reduced Sensitivity (%)
5	3550.7	0.63
10	3533.41	1.12

Table 5.7 analyzes the percentage reduction in sensitivity of the sensor for different slit widths. A reduction of 0.63% and 1.12% of sensitivity is observed for 5 nm and 10 nm slits, respectively. This result establishes a remarkable tolerance limit to the performance of the device.

5.2.5 Detection of Biomolecules

Innovations in biomedical devices are a flourishing new field in science and technologies. Biosensors will be pervasive in the near future since they are needed for anticipated practical approaches, such as detection of ambiguities in the human body and fast diagnosis of diseases. Low-cost plasmonic biosensors are ideally poised to be at the forefront of a future healthcare revolution. Therefore, the suggested RI sensor is employed to detect distinct biomolecules and DNA strands, exploiting its most sensitive parameters.

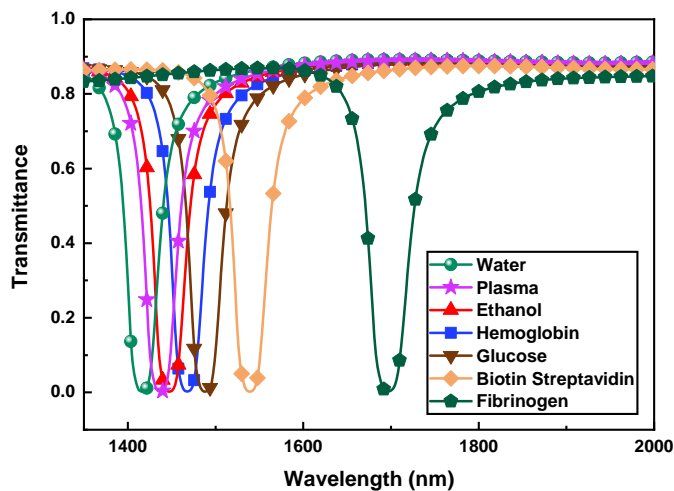


Figure 5.23: Transmission spectra for different blood components.

Blood is the fundamental fluid in the human body consisting of copious materials such as glucose, hemoglobin, ethanol, water, platelets, plasma, mineral, and proteins. The refractive index of the MUS is altered when it is filled with these different materials to assess variation in the resonant wavelengths, shown in fig. 5.23.

Water is one of the most frequently used solvents in bio-sensing applications. Therefore, the relative sensitivity of each component is evaluated with respect to the refractive index of water and represented in table 5.8. For a minimal change in the refractive index, there is a significant displacement in the resonant wavelength.

Table 5.8: Sensitivity analysis for different blood components.

Components	Refractive Index, n	Resonant Wavelength (nm)	Sensitivity (nm/RIU)
Water	1.33	1416.30	-
Blood Plasma	1.35	1437.38	1054
Ethanol	1.36	1446.93	1021
Hemoglobin	1.38	1468.02	1034
Glucose	1.40	1487.77	1021
Biotin Streptavidin	1.45	1538.90	1022
Fibrinogen	1.60	1696.80	1039

5.2.6 DNA Hybridization

When single-strand DNA (ssDNA) is transformed into double-strand DNA (dsDNA), the refractive index of the DNA layer increases from 1.456 to 1.53. This process is known as hybridization.

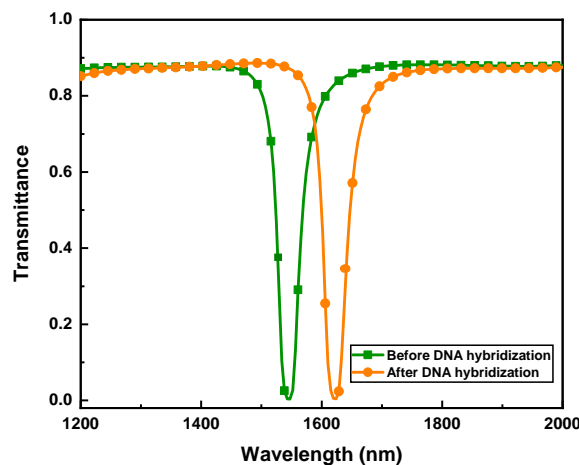


Figure 5.24: Transmission spectra for DNA hybridization.

The circular rings of the proposed sensor contain the DNA strands and the straight waveguide is filled with water during hybridization. After hybridization, the resonant

wavelength shifts from 1545 nm to 1624 nm, as depicted in fig. 5.24. Advanced optical spectrum analyzer (OSA) can detect wavelength shifts as small as 0.1 nm [116]. Thus, by equipping the proposed sensor with an OSA, it can effortlessly detect the hybridization process.

5.3 Sensor Design with Rectangular Cavities

5.3.1 Schematic Design and Methodological Study

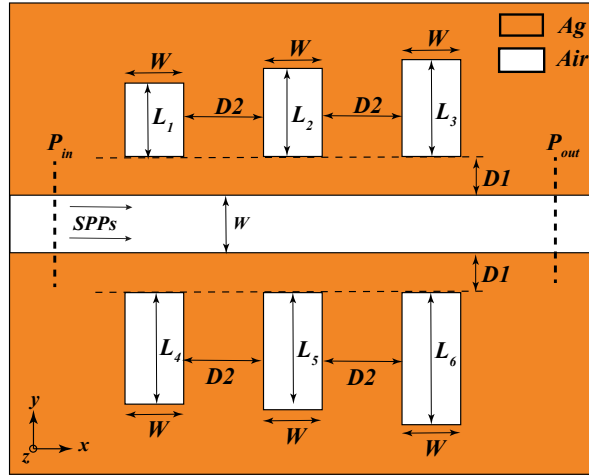


Figure 5.25: Two-dimensional schematic design of the proposed sensor.

The schematic design of the proposed sensor is presented in fig. 5.25, where the orange color represents silver, and the white color denotes air. The suggested MIM refractive index (RI) sensor incorporates six rectangular cavities of different lengths. Three cavities of length L_1 , L_2 , and L_3 are placed on the upper side of the waveguide, whereas the other three cavities of length L_4 , L_5 , L_6 are placed on the lower side. The cavities are placed at a similar distance $D1$ from the waveguide, where the distance between each cavity is $D2$. The value of the structural parameters are stated in table 5.9.

Table 5.9: Values of each schematic parameter of the proposed structure.

Parameters	Symbol	Unit (nm)
Length of the cavity to detect violet color	$L1$	125
Length of the cavity to detect blue color	$L2$	150
Length of the cavity to detect green color	$L3$	165
Length of the cavity to detect yellow color	$L4$	190
Length of the cavity to detect orange color	$L5$	210
Length of the cavity to detect red color	$L6$	225
Width of the waveguide and the cavities	W	100
Distance between the waveguide and the cavities	$D1$	40
Distance between two cavities	$D2$	300

In this paper, silver is chosen as the plasmonic material to provide an electromagnetic response within the near-infrared range due to possessing the smallest imaginary part of relative permittivity [52]. This permittivity is frequency-dependent and is characterized by Debye-Drude Model through an equation defined as [117],

$$\hat{\varepsilon}(\omega) = \varepsilon_{infnite} + \frac{\varepsilon_{static} - \varepsilon_{infnite}}{1 + i\omega\tau} + \frac{\sigma}{i\omega\varepsilon_0} = \varepsilon' - i\varepsilon'', \quad (5.11)$$

where, $\hat{\varepsilon}(\omega)$ denotes the complex relative permittivity having the real part ε' and the imaginary part ε'' at the angular frequency ω , σ designates the conductivity, i denotes the imaginary unit, and τ designates the relaxation time. Furthermore, $\varepsilon_{infnite}$, ε_{static} , and ε_0 represent the infinite-frequency relative permittivity, the zero-frequency relative permittivity, and the permittivity of free space, respectively. Gai *et al.* [118] optimized the values of $\varepsilon_{infnite}$, ε_{static} , σ , and τ at 3.8344, -9530.5, 1.1486×10^7 S/m, and 7.35×10^{-15} second for silver, respectively.

Furthermore, parts of incident waves are coupled into cavities to reach the output port due to the excitation of fundamental mode at the input port. This dispersion relation is expressed as [119],

$$\tanh\left(-\frac{ik_{c1}}{2}w\right) = -\frac{\varepsilon_{silver}k_{c2}}{\varepsilon_{air}k_{c1}}, \quad (5.12)$$

where, k_{c1} , and k_{c2} are momentum conservations defined as,

$$\begin{cases} k_{c1}^2 = \varepsilon_{air}k_0^2 - \beta^2, \\ k_{c2}^2 = \varepsilon_{silver}k_0^2 - \beta^2, \end{cases} \quad (5.13)$$

where, the dielectric constant of silver and air are represented as ε_{silver} , and ε_{air} , respectively. Furthermore, the resonance wavelength, λ_{res} is derived as [120],

$$\lambda_{res} = \frac{4\text{Re}(\eta_{eff})L}{M}, M = 1, 2, 3, \dots, \quad (5.14)$$

where, L is the effective resonance length, M is the mode integer, and η_{eff} is the effective refractive index. The real part of η_{eff} can be calculated from,

$$\text{Re}(\eta_{eff}) = \sqrt{\left[\varepsilon_{silver} + \left(\frac{k}{k_0}\right)^2\right]}, \quad (5.15)$$

where, k_0 is the wavenumber.

5.3.2 Sensing Procedure

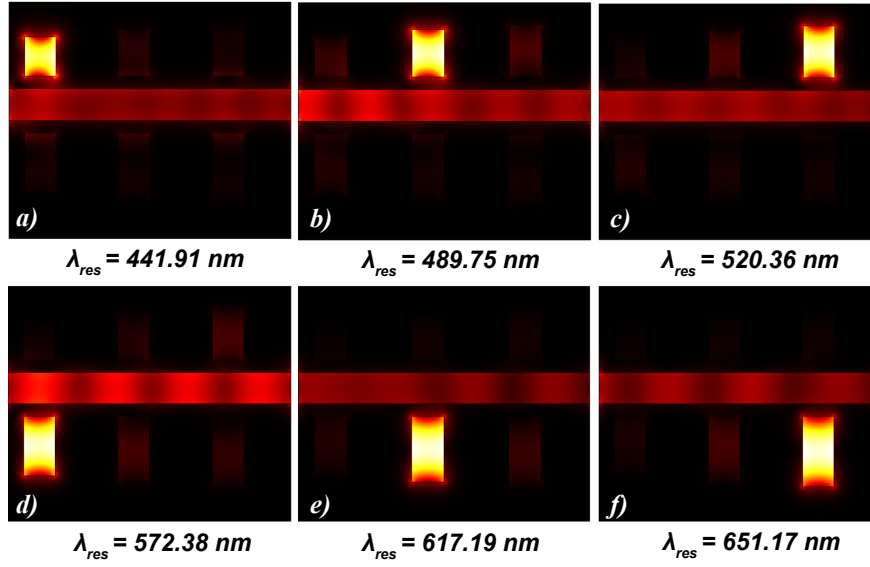


Figure 5.26: *E*-field confinement in rectangular cavities of length (a) L_1 , (b) L_2 , (c) L_3 , (d) L_4 , (e) L_5 , and (f) L_6 at initial parameters.

From eq. (5.14), $\lambda_{res} \propto L$ while effective refractive index and mode are fixed. Different wavelengths of light in the visible color range produce different colors. Colors can easily be detected if the resonance wavelength is known. Therefore, the proposed sensor contains six different-length cavities to detect six basic colors – violet, blue, green, yellow, orange, and red. Different resonance wavelengths confine in the specific cavity. The *E*-field confinement of those resonance wavelengths has been depicted in fig. 5.26. The transmittance curve (shown in fig. 5.27) exhibits six sharp resonance dips at six different resonance wavelengths at refractive index, $\eta = 1$. Table 5.10 provides a comparison between these resonance wavelengths of six colors and their typical wavelength range [52]. Therefore, the detection of those specific colors is established.

The performance of a RI sensor can be measured through two significant factors - sensitivity and figure of merit which are determined as,

$$\text{Sensitivity}(S) = \frac{\text{Change in Wavelength } (\Delta\lambda)}{\text{Change in Refractive Index } (\Delta\eta)}, \quad (5.16)$$

and,

$$\text{Figure of Merit } (FOM) = \frac{\text{Sensitivity } (S)}{\text{Full Width at Half Maximum } (FWHM)}. \quad (5.17)$$

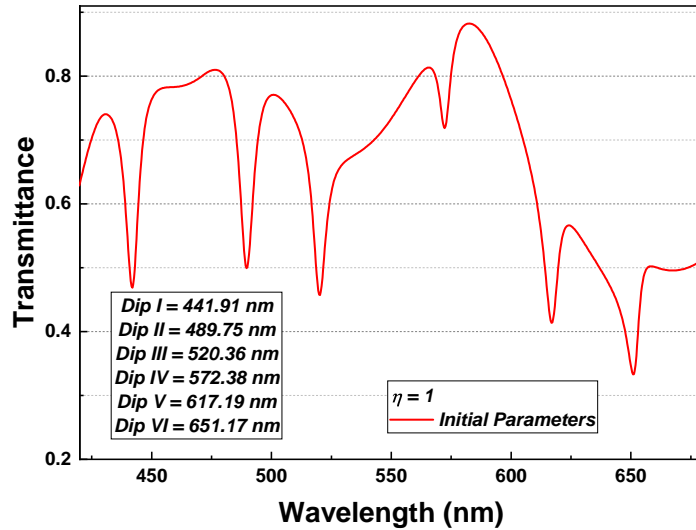


Figure 5.27: Transmittance spectrum of the proposed sensor at initial parameters.

Table 5.10: The wavelength range for six visible basic colors.

Color	Violet	Blue	Green	Yellow	Orange	Red
Wavelength range of color (nm) [52]	380 - 450	450 - 495	495 - 570	570 - 590	590 - 620	620 - 750
Resonance wavelength of proposed sensor (nm)	441.91	489.75	520.36	572.38	617.19	651.17

5.3.3 Result Analysis for Initial Framework

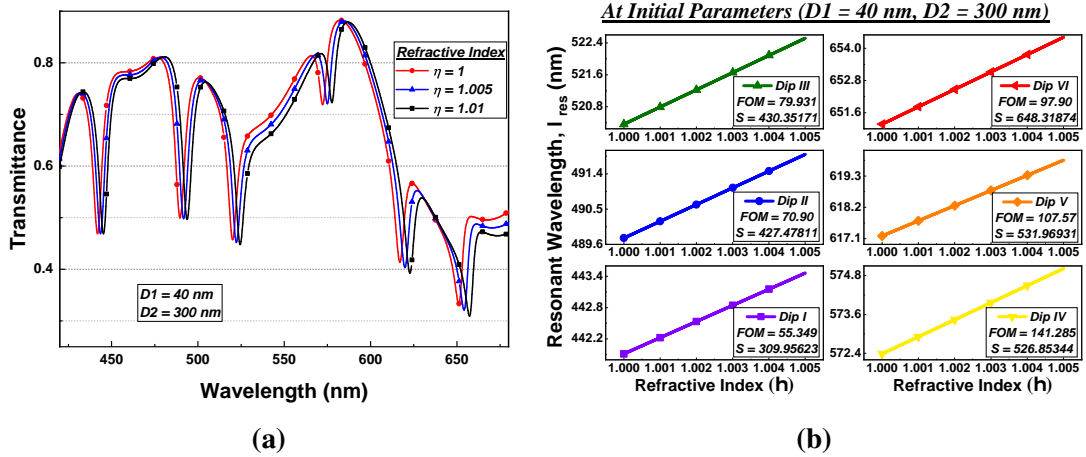


Figure 5.28: (a) Transmittance vs. wavelength curve for different values of refractive index, η . (b) Resonance wavelength vs. refractive index curve for initial framework.

To calculate the sensitivity of the proposed structure, the refractive index is varied from 1 to 1.01, with an interval of .005, and redshift is observed at resonance dips (fig. 5.28a). Furthermore, the sensitivity and FOM have been calculated, and the existence of positive slopes in fig. 5.28b substantiates the redshift. The highest sensitivity

and FOM are found as 648.41 nm/RIU and 141.29 at $\eta = 1$. The proposed structure is optimized in terms of FOM in the later section to obtain superior filter performance.

5.3.4 Optimization of Parameter $D2$ and $D1$

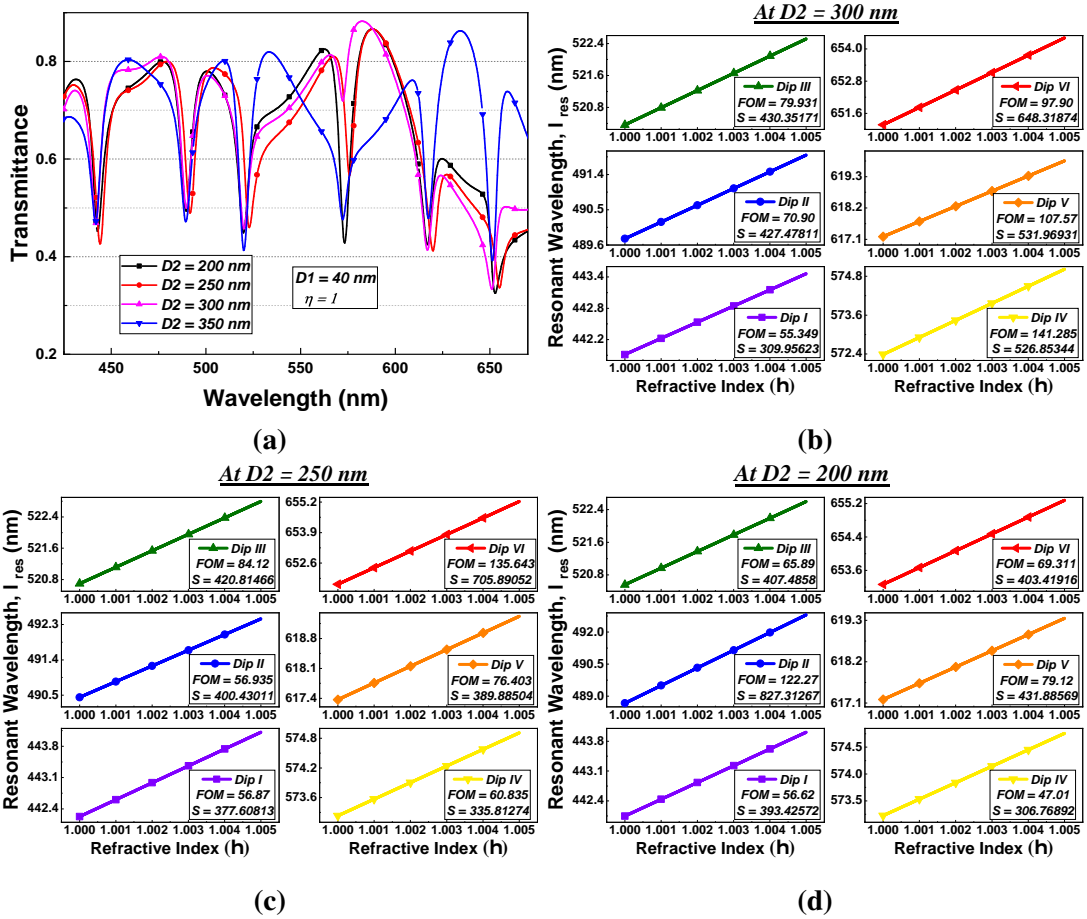


Figure 5.29: (a) Transmittance vs. wavelength curve for different values of $D2$. Resonance wavelength vs. refractive index curve for (b) $D2 = 300$ nm. (c) $D2 = 250$ nm, and (d) $D2 = 200$ nm.

The optimization of the proposed sensor starts by varying $D2$ from 200 nm to 350 nm, with an interval of 50 nm, while keeping $D1$ constant at 40 nm. The parametric value of $D2$ more than 300 nm shifts the resonance dip from desired visible color range and distorts the transmittance curve (fig. 5.29a). Redshift is observed for the remaining values of $D2$, which is indisputable from positive slope for each resonance dip demonstrated in fig. 5.29b – fig. 5.29d.

Comparing the FOM, $D2 = 200$ nm is not a suitable option as the FOM of each dip is decreased (fig. 5.29d). Furthermore, for $D2 = 250$ nm, FOM of *Dip I*, *Dip III*, *Dip VI* increase while others decrease. Nonetheless, $D2 = 250$ nm is chosen as it provides higher FOM to detect violet light using *Dip I*. Violet light is prioritized in this

particular scenario as recent works explored the use of the violet light in various cases such as fungal study [122], dental bleaching [123], forensic science [124], surgical management [125].

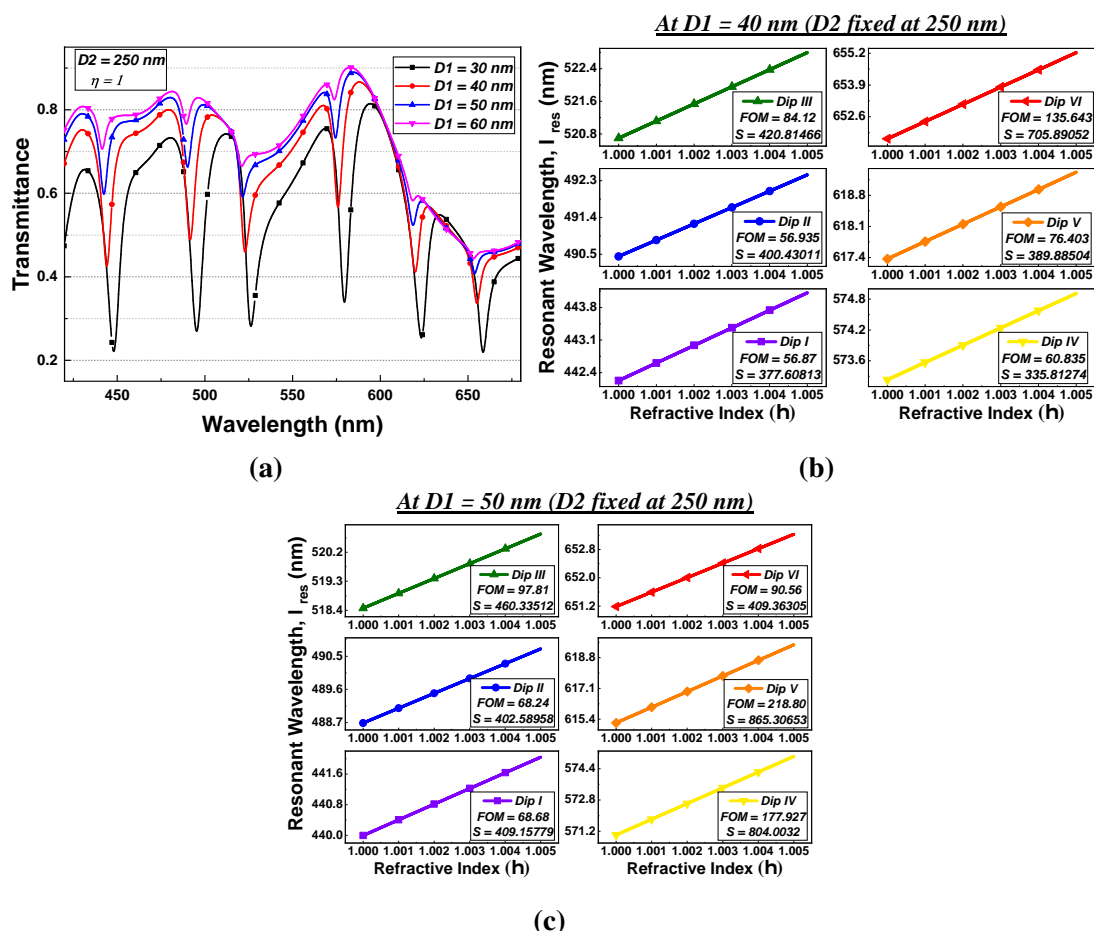


Figure 5.30: (a) Transmittance vs. wavelength curve for different values of D_1 . Resonance wavelength vs. refractive index curve for (b) $D_1 = 40$ nm and (c) $D_1 = 50$ nm.

Figure 5.30a resembles the transmittance vs. wavelength curve for different values of D_1 ranging from 30 nm to 60 nm, with an interval of 10 nm. For $D_1 = 30$ nm, the resonance dip for orange color (621.37 nm) shift from the desired wavelength range (table 5.10). Furthermore, when $D_1 \geq 60$ nm, the resonance dips are not so sharp and almost diminishing. Hence, $D_1 = 30$ nm and $D_1 = 60$ nm cannot be taken as optimized values. Figure 5.30b and fig. 5.30c illustrate the resonance wavelength vs. refractive index curves for $D_1 = 40$ nm and $D_1 = 50$ nm, respectively. It is observed that $D_1 = 50$ nm provides higher FOM along with higher sensitivity compared to $D_1 = 40$ nm. Hence, the optimized value for D_1 is settled as 50 nm.

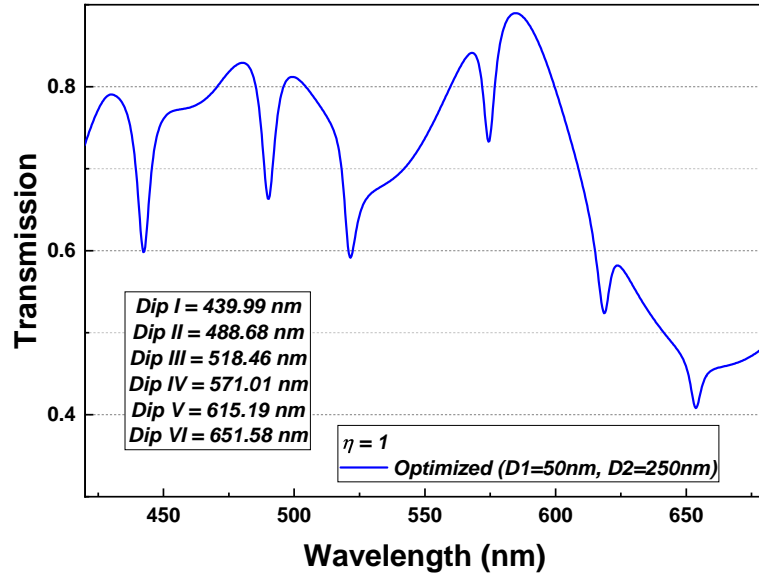


Figure 5.31: Transmittance spectrum of the proposed sensor at optimized parameters.

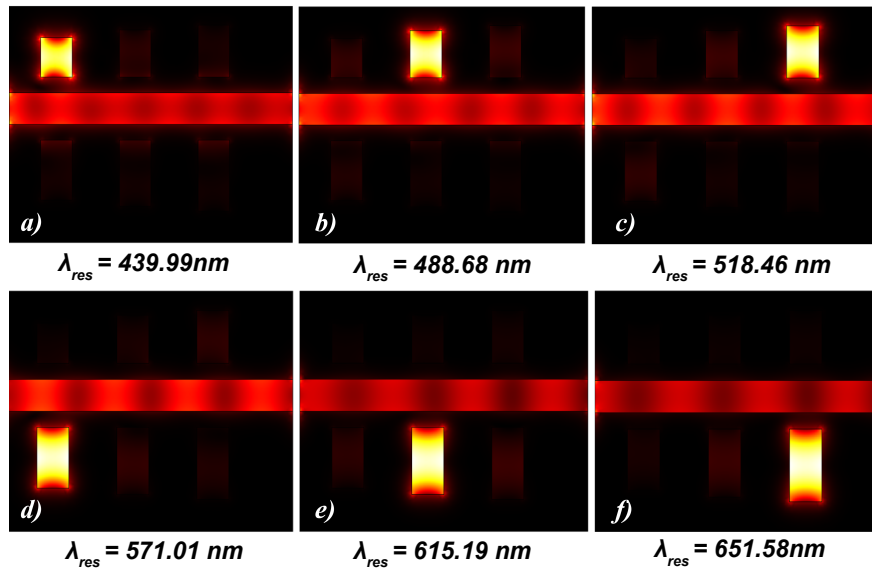


Figure 5.32: *E*-field confinement in rectangular cavities of length (a) L_1 , (b) L_2 , (c) L_3 , (d) L_4 , (e) L_5 , and (f) L_6 at optimized parameters.

Finally, fig. 5.31 displays the transmittance vs. wavelength curve for the optimized parameters, where the legend indicates the resonance wavelengths. Furthermore, fig. 5.32 portrays the *E*-field confinement in the cavities for those resonance wavelengths. Moreover, table 5.11 epitomizes the change of sensitivity and FOM before and after the optimization process. Therefore, the highest sensitivity and FOM offered by the proposed sensor are 865.31 nm/RIU and 218.80, respectively.

Table 5.11: Summary of the optimization process.

Dip	Sensitivity (nm/RIU)		FOM	
	D2 = 300 nm D1 = 40 nm	D2 = 250 nm D1 = 50 nm	D2 = 300 nm D1 = 40 nm	D2 = 250 nm D1 = 50 nm
	(Initial Value)	(Optimized Value)	(Initial Value)	(Optimized Value)
<i>Dip I</i>	309.95623	409.15779	55.349	68.68
<i>Dip II</i>	427.47811	402.58958	70.90	68.24
<i>Dip III</i>	430.35171	460.33512	79.931	97.81
<i>Dip IV</i>	526.85344	804.0032	141.285	177.927
<i>Dip V</i>	531.96931	865.30653	107.57	218.80
<i>Dip VI</i>	648.31874	409.36305	97.90	90.56

In different literature, another performance metric FOM* is measured at a defined wavelength as [126],

$$FOM^* = \frac{\Delta R}{R\Delta\eta} = \frac{|R_{\eta=1.005} - R_{\eta=1}|}{.005 \times R_{\eta=1}}. \quad (5.18)$$

where, ΔR stands for variation in reflection intensity caused by variation in refractive index ($\Delta\eta$) and R is the reflection rate in the sensor.

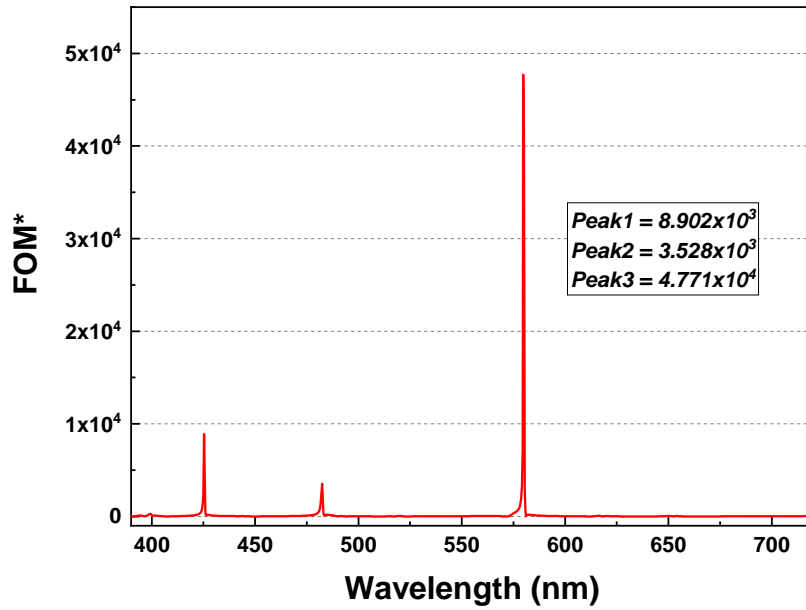


Figure 5.33: FOM* at optimized parameters.

The measured FOM* is plotted in the fig. 5.33, where three FOM* peaks are observed. The highest FOM* is found as 4.771×10^4 .

5.3.5 Fabrication

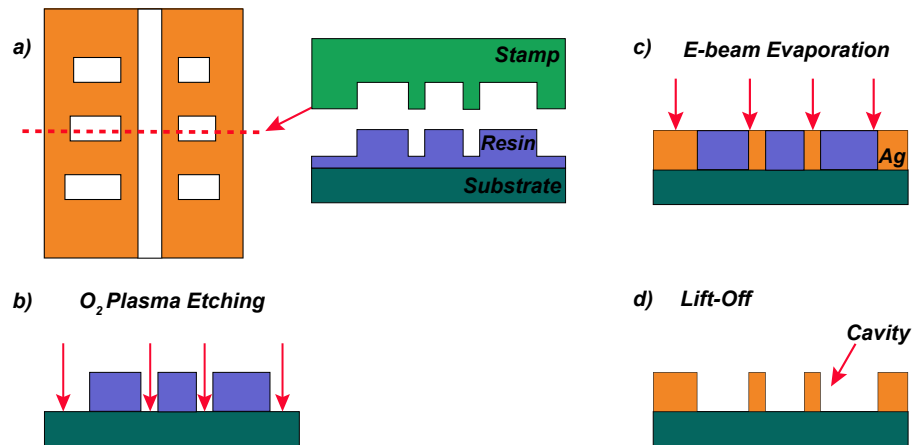


Figure 5.34: Fabrication technique of the proposed sensor.

The structural parameters have been fixed considering vertically smooth sidewalls and nearly 90° corners offered by the nanoimprint lithography fabrication process [121]. The whole procedure is illustrated in fig. 5.34, where the silicon wafer is considered as the substrate. The first step is imprinting the blueprint of the sensor over the resin using a stamp (fig. 5.34a). The undesired resin is then removed from the compressed area through O₂ plasma etching (fig. 5.34b). Subsequently, electron beam evaporation (fig. 5.34c) deposits the silver on the substrate, followed by eliminating residual resin through the lift-off technique (fig. 5.34d).

Chapter 6

Conclusion and Future Work

6.1 Conclusion

In this paper, three RI sensors employing the MIM waveguide arrangement are investigated. The numerical computation of the proposed structures is done utilizing the 2D-Finite Element Method (FEM) of the COMSOL Multiphysics with scattering boundary conditions. Different segments of the proposed paper explain theoretical and mathematical relations along with fabrication and optimization procedures.

The proposed first structure has a baffle in between and vertically couples a CDRR. After optimization, the proposed device attains a maximum sensitivity of 3522.44 nm/RIU. The sensor then performs two tasks to exploit its high sensitivity: detecting the cancer cells and sensing the concentration of solutes for different water-ethanol-glucose solutions. The suggested sensor offers a maximum sensitivity of 4217.61 nm/RIU and 4092.7 nm/RIU for the cancerous and aqueous samples, respectively. Thus, the optimized design can be a promising nanoscale solution in the fields of biology and chemistry. Moreover, additional analyses report a maximum FOM , FOM^* , and Q -factor of 80.07, 0.73×10^6 , and 83.65, respectively.

The proposed second structure consists of multiple rings and a straight waveguide. Extensive simulations display that the transmission spectrum shows notable shifts in resonant wavelengths due to alterations in geometrical parameters, and a maximum sensitivity of 3573.3 nm/RIU is obtained. Moreover, FOM and Q -factor of the sensor are 21.9 and 13.6, respectively. The tolerance capability of the structure is also studied by introducing nano slits on the rings and demonstrates satisfactory performance. Furthermore, the sensor proves to be highly sensitive for the label-free detection of blood components and DNA hybridization.

The proposed third structure encompasses six rectangular cavities. The resonance dips

achieved through simulation can detect six basic colors used in various medical, photonics, industrial applications. Alternatively, this color detection-focused optimized structure can also be used as an RI sensor with maximum sensitivity, FOM , and FOM^* of 218.80, and 4.771×10^4 , respectively.

Table 6.1: Performance comparison of the proposed works with recent literature.

Reference	Max. Sensitivity (nm/RIU)	Max. FOM	Max. FOM^*
[41]	718	-	4354
[42]	986	-	3.2×10^5
[43]	1100	-	1.08×10^5
[44]	1380	104	-
[45]	1562.5	38.6	-
[46]	680	8.68	-
[47]	1060	203.8	-
[48]	1367	25	-
[49]	1550	43.05	-
[50]	1600	193	-
[52]	700	-	191.6
[127]	1100	-	2.73×10^4
[128]	1450	-	3.51×10^4
[129]	2000	-	4.05×10^4
[120]	1320	16.7	-
[53]	608	105.02	-
[130]	1295	159.6	-
Proposed first work	3522.44	80.07	0.73×10^6
Proposed second work	3573.3	21.9	-
Proposed third work	865.31	218.8	4.771×10^4

Table 6.1 compares the performance of the proposed works with recent literature. The tabular analysis displays that the suggested nanosensors outperform the recent works in terms of sensitivity, FOM and FOM^* . Therefore, these sensors can be an effective solution for on-chip sensing applications.

6.2 Future Work

The following steps can be taken in the future to further enhance the performance of MIM-based plasmonic RI sensors:

- Alternative materials can be explored instead of conventional noble plasmonic materials.
- Integration of deep neural networks and machine learning algorithms can be implemented in the optimization process to reduce computational time.
- Inclusion of defects, for example, nanodots, and their effects on the transmittance profile can be studied.

REFERENCES

- [1] M. L. Brongersma and V. M. Shalaev, “The case for plasmonics,” *science*, vol. 328, no. 5977, pp. 440–441, 2010.
- [2] W. L. Barnes, A. Dereux, and T. W. Ebbesen, “Surface plasmon subwavelength optics,” *Nature*, vol. 424, no. 6950, pp. 824–830, 2003.
- [3] G. V. Naik, V. M. Shalaev, and A. Boltasseva, “Alternative plasmonic materials: Beyond gold and silver,” *Advanced Materials*, vol. 25, no. 24, pp. 3264–3294, 2013.
- [4] A. V. Zayats, I. I. Smolyaninov, and A. A. Maradudin, “Nano-optics of surface plasmon polaritons,” *Physics reports*, vol. 408, no. 3-4, pp. 131–314, 2005.
- [5] P. K. Maharana, T. Srivastava, and R. Jha, “Low index dielectric mediated surface plasmon resonance sensor based on graphene for near infrared measurements,” *Journal of Physics D: Applied Physics*, vol. 47, no. 38, 2014.
- [6] J. Homola, S. S. Yee, and G. Gauglitz, “Surface plasmon resonance sensors,” *Sensors and actuators B: Chemical*, vol. 54, no. 1-2, pp. 3–15, 1999.
- [7] M. A. Butt, S. N. Khonina, and N. L. Kazanskiy, “Ultra-short lossless plasmonic power splitter design based on metal-insulator-metal waveguide,” *Laser Physics*, vol. 30, no. 1, p. ab5577, 2020.
- [8] Y. Guo, L. Yan, W. Pan, B. Luo, K. Wen, Z. Guo, H. Li, and X. Luo, “A plasmonic splitter based on slot cavity,” *Optics Express*, vol. 19, no. 15, p. 13831, 2011.
- [9] X. Gao, L. Zhou, X. Y. Yu, W. P. Cao, H. O. Li, H. F. Ma, and T. J. Cui, “Ultra-wideband surface plasmonic Y-splitter,” *Optics Express*, vol. 23, no. 18, p. 23270, 2015.
- [10] L. Shirafkan Dizaj, K. Abbasian, and T. Nurmohammadi, “A Three-Core Hybrid Plasmonic Polarization Splitter Designing Based on the Hybrid Plasmonic

- Waveguide for Utilizing in Optical Integrated Circuits,” *Plasmonics*, vol. 15, no. 6, pp. 2213–2221, 2020.
- [11] R. H. Sagor, M. S. I. Sumon, and M. Tazwar, “Design and Analysis of a Novel Air Gap–Based Semi-elliptical Nanoplasmonic Coupler,” *Plasmonics*, vol. 14, no. 6, pp. 1993–2001, 2019.
- [12] R. A. Wahsheh, Z. Lu, and M. A. Abushagur, “Nanoplasmonic couplers and splitters,” *Optics Express*, vol. 17, no. 21, pp. 19033–19040, 2009.
- [13] C. Yeh, T. Ootoshi, and F. Shimabukuro, “Thin-ribbon tapered coupler for dielectric waveguides,” *In its The Telecommunications and Data Acquisition Report*, vol. 1, pp. 42–48, 1994.
- [14] M. Lamponi, S. Keyvaninia, C. Jany, F. Poingt, F. Lelarge, G. De Valicourt, G. Roelkens, D. Van Thourhout, S. Messaoudene, J. M. Fedeli, and G. H. Duan, “Low-threshold heterogeneously integrated InP/SOI lasers with a double adiabatic taper coupler,” *IEEE Photonics Technology Letters*, vol. 24, no. 1, pp. 76–78, 2012.
- [15] D. F. Pile and D. K. Gramotnev, “Adiabatic and nonadiabatic nanofocusing of plasmons by tapered gap plasmon waveguides,” *Applied Physics Letters*, vol. 89, no. 4, 2006.
- [16] P. Ginzburg and M. Orenstein, “Plasmonic transmission lines: from micro to nano scale with $\lambda/4$ impedance matching,” *Optics Express*, vol. 15, no. 11, p. 6762, 2007.
- [17] G. Veronis, W. Shin, and S. Fan, “Compact couplers between dielectric and metal-dielectric-metal plasmonic waveguides,” *Optics InfoBase Conference Papers*, vol. 15, no. 3, pp. 1158–1160, 2007.
- [18] D. K. Lau, S. P. Marsh, L. E. Davis, and R. Sloan, “Simplified design technique for high-performance microstrip multisection couplers,” *IEEE transactions on microwave theory and techniques*, vol. 46, no. 12, pp. 2507–2513, 1998.
- [19] J. Tao, X. G. Huang, X. Lin, Q. Zhang, and X. Jin, “A narrow-band subwavelength plasmonic waveguide filter with asymmetrical multiple-teeth-shaped structure,” *Optics Express*, vol. 17, no. 16, p. 13989, 2009.
- [20] X.-S. Lin and X.-G. Huang, “Tooth-shaped plasmonic waveguide filters with nanometric sizes,” *Optics Letters*, vol. 33, no. 23, p. 2874, 2008.

- [21] H. Lu, X. Liu, D. Mao, L. Wang, and Y. Gong, "Tunable band-pass plasmonic waveguide filters with nanodisk resonators," *Optics Express*, vol. 18, no. 17, p. 17922, 2010.
- [22] P. Tetiana and O. Trubin, "Novel dual-band rectangular dielectric resonator filter," *BIHTEL 2014 - 10th International Symposium on Telecommunications, Proceedings*, pp. 2–6, 2014.
- [23] M. Matsuo, H. Yabuki, and M. Makimoto, "Dual-mode stepped-impedance ring resonator for bandpass filter applications," *IEEE Transactions on Microwave Theory and Techniques*, vol. 49, no. 7, pp. 1235–1240, 2001.
- [24] R. H. Sagor, M. F. Hassan, S. Sharmin, T. Z. Adry, and M. A. R. Emon, "Numerical investigation of an optimized plasmonic on-chip refractive index sensor for temperature and blood group detection," *Results in Physics*, vol. 19, p. 103611, 2020.
- [25] M. F. O. Hameed and S. Obayya, *Computational photonic sensors*. Springer International Publishing, 2018.
- [26] M. S. Luchansky, A. L. Washburn, T. A. Martin, M. Iqbal, L. C. Gunn, and R. C. Bailey, "Characterization of the evanescent field profile and bound mass sensitivity of a label-free silicon photonic microring resonator biosensing platform," *Biosensors and Bioelectronics*, vol. 26, no. 4, pp. 1283–1291, 2010.
- [27] M. R. Rakhshani and M. A. Mansouri-Birjandi, "Engineering Hexagonal Array of Nanoholes for High Sensitivity Biosensor and Application for Human Blood Group Detection," *IEEE Transactions on Nanotechnology*, vol. 17, no. 3, pp. 475–481, 2018.
- [28] E. Economou, "Surface plasmons in thin films," *Physical review*, vol. 182, no. 2, p. 539, 1969.
- [29] J. Dionne, L. Sweatlock, H. Atwater, and A. Polman, "Plasmon slot waveguides: Towards chip-scale propagation with subwavelength-scale localization," *Physical Review B*, vol. 73, no. 3, p. 035407, 2006.
- [30] D. Sarid, "Long-range surface-plasma waves on very thin metal films," *Physical Review Letters*, vol. 47, no. 26, p. 1927, 1981.
- [31] M. F. Hassan, R. H. Sagor, I. Tathfif, K. S. Rashid, and M. Radoan, "An optimized dielectric-metal-dielectric refractive index nanosensor," *IEEE Sensors Journal*, vol. 21, no. 2, pp. 1461–1469, 2020.

- [32] M. Alam, J. Meier, J. Aitchison, and M. Mojahedi, "Super mode propagation in low index medium," in *Quantum Electronics and Laser Science Conference*, p. JThD112, Optical Society of America, 2007.
- [33] M. Butt, N. Kazanskiy, and S. Khonina, "Hybrid plasmonic waveguide race-track μ -ring resonator: Analysis of dielectric and hybrid mode for refractive index sensing applications," *Laser Physics*, vol. 30, no. 1, p. 016202, 2019.
- [34] M. Butt, S. Khonina, and N. Kazanskiy, "Hybrid plasmonic waveguide-assisted metal-insulator-metal ring resonator for refractive index sensing," *Journal of Modern Optics*, vol. 65, no. 9, pp. 1135–1140, 2018.
- [35] H. H. Goldstine and A. Goldstine, "The electronic numerical integrator and computer (eniac)," *Mathematical Tables and Other Aids to Computation*, vol. 2, no. 15, pp. 97–110, 1946.
- [36] T. Haigh, P. M. Priestley, M. Priestley, and C. Rope, *ENIAC in action: Making and remaking the modern computer*. MIT press, 2016.
- [37] D. A. B. Miller and H. M. Ozaktas, "Limit to the bit-rate capacity of electrical interconnects from the aspect ratio of the system architecture," *Journal of parallel and distributed computing*, vol. 41, no. 1, pp. 42–52, 1997.
- [38] M. Horowitz, C.-K. K. Yang, and S. Sidiropoulos, "High-speed electrical signaling: Overview and limitations," *IEEE Micro*, vol. 18, no. 1, pp. 12–24, 1998.
- [39] S. C. Esener, "Implementation and prospects for chip-to-chip free-space optical interconnects," in *International Electron Devices Meeting. Technical Digest (Cat. No. 01CH37224)*, pp. 23–5, IEEE, 2001.
- [40] B. Hecht, H. Bielefeldt, L. Novotny, Y. Inouye, and D. Pohl, "Local excitation, scattering, and interference of surface plasmons," *Physical review letters*, vol. 77, no. 9, p. 1889, 1996.
- [41] X. Zhao, Z. Zhang, and S. Yan, "Tunable fano resonance in asymmetric mim waveguide structure," *Sensors*, vol. 17, no. 7, p. 1494, 2017.
- [42] N. Jankovic and N. Cselyuszka, "Multiple fano-like mim plasmonic structure based on triangular resonator for refractive index sensing," *Sensors*, vol. 18, no. 1, p. 287, 2018.
- [43] Q. Yang, X. Liu, F. Guo, H. Bai, B. Zhang, X. Li, Y. Tan, and Z. Zhang, "Multiple fano resonance in mim waveguide system with cross-shaped cavity," *Optik*, vol. 220, p. 165163, 2020.

- [44] M. R. Rakhshani, "Optical refractive index sensor with two plasmonic double-square resonators for simultaneous sensing of human blood groups," *Photonics and Nanostructures - Fundamentals and Applications*, vol. 39, no. October 2019, p. 100768, 2020.
- [45] Y.-Y. Xie, Y.-X. Huang, W.-L. Zhao, W.-H. Xu, and C. He, "A novel plasmonic sensor based on metal-insulator-metal waveguide with side-coupled hexagonal cavity," *IEEE Photonics Journal*, vol. 7, no. 2, pp. 1–12, 2015.
- [46] Y. Wang, M. Zheng, Q. Ruan, Y. Zhou, Y. Chen, P. Dai, Z. Yang, Z. Lin, Y. Long, Y. Li, N. Liu, C. W. Qiu, J. K. Yang, and H. Duan, "Stepwise-nanocavity-assisted transmissive color filter array microprints," *Research*, vol. 2018, pp. 10–14, 2018.
- [47] Y. Zhang and M. Cui, "Refractive index sensor based on the symmetric mim waveguide structure," *Journal of Electronic Materials*, vol. 48, no. 2, pp. 1005–1010, 2019.
- [48] M. A. Butt, S. N. Khonina, and N. L. Kazanskiy, "Metal-insulator-metal nano square ring resonator for gas sensing applications," *Waves in Random and Complex Media*, vol. 0, no. 0, pp. 1–11, 2019.
- [49] H. Su, S. Yan, X. Yang, J. Guo, J. Wang, and E. Hua, "Sensing features of the fano resonance in an MIM waveguide coupled with an elliptical ring resonant cavity," *Applied Sciences (Switzerland)*, vol. 10, no. 15, 2020.
- [50] Y.-P. Qi, L.-Y. Wang, Y. Zhang, T. Zhang, B.-H. Zhang, X.-Y. Deng, and X.-X. Wang, "Multiple fano resonances in metal-insulator-metal waveguide with umbrella resonator coupled with metal baffle for refractive index sensing," *Chinese Physics B*, vol. 29, no. 6, p. 067303, 2020.
- [51] K. Diest, J. A. Dionne, M. Spain, and H. A. Atwater, "Tunable color filters based on metal-insulator-metal resonators," *Nano Letters*, vol. 9, no. 7, pp. 2579–2583, 2009.
- [52] M. A. Butt, S. N. Khonina, and N. L. Kazanskiy, "A plasmonic colour filter and refractive index sensor applications based on metal-insulator-metal square μ -ring cavities," *Laser Physics*, vol. 30, no. 1, 2020.
- [53] Z. Zhang, J. Yang, H. Xu, S. Xu, Y. Han, X. He, J. Zhang, J. Huang, D. Chen, and W. Xie, "A plasmonic ellipse resonator possessing hybrid modes for ultracompact chipscale application," *Physica Scripta*, vol. 94, no. 12, p. 125511, 2019.

- [54] A. Akhavan, H. Ghafoorifard, S. Abdolhosseini, and H. Habibiyan, "Metal-insulator-metal waveguide-coupled asymmetric resonators for sensing and slow light applications," *IET Optoelectronics*, vol. 12, no. 5, pp. 220–227, 2018.
- [55] S. Ghorbani, M. A. Dashti, and M. Jabbari, "Plasmonic nano-sensor based on metal-dielectric-metal waveguide with the octagonal cavity ring," *Laser Physics*, vol. 28, no. 6, p. 066208, 2018.
- [56] A. Rashed, B. Gudulluoglu, H. Yun, M. Habib, I. Boyaci, S. Hong, E. Ozbay, and H. Caglayan, "Highly-sensitive refractive index sensing by near-infrared metatronic nanocircuits," *Scientific reports*, vol. 8, no. 1, pp. 1–9, 2018.
- [57] X. Yi, J. Tian, and R. Yang, "Tunable fano resonance in plasmonic mdm waveguide with a square type split-ring resonator," *Optik*, vol. 171, pp. 139–148, 2018.
- [58] M. J. Al Mahmod, R. Hyder, and M. Z. Islam, "A highly sensitive metal-insulator-metal ring resonator-based nanophotonic structure for biosensing applications," *IEEE Sensors Journal*, vol. 18, no. 16, pp. 6563–6568, 2018.
- [59] X. Ren, K. Ren, and C. Ming, "Self-reference refractive index sensor based on independently controlled double resonances in side-coupled u-shaped resonators," *Sensors*, vol. 18, no. 5, p. 1376, 2018.
- [60] R. Zafar, S. Nawaz, G. Singh, A. d'Alessandro, and M. Salim, "Plasmonics-based refractive index sensor for detection of hemoglobin concentration," *IEEE Sensors Journal*, vol. 18, no. 11, pp. 4372–4377, 2018.
- [61] S. Asgari and N. Granpayeh, "Tunable mid-infrared refractive index sensor composed of asymmetric double graphene layers," *IEEE Sensors Journal*, vol. 19, no. 14, pp. 5686–5691, 2019.
- [62] X. Wang, J. Zhu, X. Wen, X. Wu, Y. Wu, Y. Su, H. Tong, Y. Qi, and H. Yang, "Wide range refractive index sensor based on a coupled structure of au nanocubes and au film," *Optical Materials Express*, vol. 9, no. 7, pp. 3079–3088, 2019.
- [63] Y. Qi, Y. Wang, X. Zhang, C. Liu, B. Hu, Y. Bai, and X. Wang, "A theoretical study of optically enhanced transmission characteristics of subwavelength metal y-shaped arrays and its application on refractive index sensor," *Results in Physics*, vol. 15, p. 102495, 2019.
- [64] Y. Wen, Y. Sun, C. Deng, L. Huang, G. Hu, B. Yun, R. Zhang, and Y. Cui, "High sensitivity and fom refractive index sensing based on fano resonance in

- all-grating racetrack resonators,” *Optics Communications*, vol. 446, pp. 141–146, 2019.
- [65] Z. Li, K. Wen, L. Chen, L. Lei, J. Zhou, D. Zhou, Y. Fang, and B. Wu, “Control of multiple fano resonances based on a subwavelength mim coupled cavities system,” *IEEE Access*, vol. 7, pp. 59369–59375, 2019.
- [66] X. Yang, E. Hua, M. Wang, Y. Wang, F. Wen, and S. Yan, “Fano resonance in a mim waveguide with two triangle stubs coupled with a split-ring nanocavity for sensing application,” *Sensors*, vol. 19, no. 22, p. 4972, 2019.
- [67] Y. Zhang, Y. Kuang, Z. Zhang, Y. Tang, J. Han, R. Wang, J. Cui, Y. Hou, and W. Liu, “High-sensitivity refractive index sensors based on fano resonance in the plasmonic system of splitting ring cavity-coupled mim waveguide with tooth cavity,” *Applied Physics A*, vol. 125, no. 1, pp. 1–5, 2019.
- [68] J. Zhu, X. Wang, X. Wu, Y. Su, Y. Xu, Y. Qi, L. Zhang, and H. Yang, “Ultra wide sensing range plasmonic refractive index sensor based on nano-array with rhombus particles,” *Chinese Physics B*, vol. 29, no. 11, p. 114204, 2020.
- [69] X. Li, D. Wang, S. Wang, L. Yuan, J. Lei, and X. Li, “Enhanced plasmonic-induced absorption using a cascade scheme and its application as refractive-index sensor,” *Photonic Sensors*, vol. 10, no. 2, pp. 162–170, 2020.
- [70] R. El Haffar, A. Farkhsi, and O. Mahboub, “Optical properties of mim plasmonic waveguide with an elliptical cavity resonator,” *Applied Physics A*, vol. 126, pp. 1–10, 2020.
- [71] M. A. A. Butt and N. Kazanskiy, “Enhancing the sensitivity of a standard plasmonic mim square ring resonator by incorporating the nano-dots in the cavity,” *Photonics Letters of Poland*, vol. 12, no. 1, pp. 1–3, 2020.
- [72] A. Alipour, A. Mir, and A. Farmani, “Ultra high-sensitivity and tunable dual-band perfect absorber as a plasmonic sensor,” *Optics & Laser Technology*, vol. 127, p. 106201, 2020.
- [73] M. Butt, S. Khonina, and N. Kazanskiy, “An array of nano-dots loaded mim square ring resonator with enhanced sensitivity at nir wavelength range,” *Optik*, vol. 202, p. 163655, 2020.
- [74] J. Zhu and N. Li, “Mim waveguide structure consisting of a semicircular resonant cavity coupled with a key-shaped resonant cavity,” *Optics Express*, vol. 28, no. 14, pp. 19978–19987, 2020.

- [75] N. Amoosoltani, N. Yasrebi, A. Farmani, and A. Zarifkar, "A plasmonic nano-biosensor based on two consecutive disk resonators and unidirectional reflectionless propagation effect," *IEEE Sensors Journal*, vol. 20, no. 16, pp. 9097–9104, 2020.
- [76] Y. Fang, K. Wen, Z. Li, B. Wu, and Z. Guo, "Plasmonic refractive index sensor with multi-channel fano resonances based on mim waveguides," *Modern Physics Letters B*, vol. 34, no. 16, p. 2050173, 2020.
- [77] S. Asgari, S. Pooretamad, and N. Granpayeh, "Plasmonic refractive index sensor based on a double concentric square ring resonator and stubs," *Photonics and Nanostructures-Fundamentals and Applications*, vol. 42, p. 100857, 2020.
- [78] R. Al Mahmud, M. O. Faruque, and R. H. Sagor, "A highly sensitive plasmonic refractive index sensor based on triangular resonator," *Optics Communications*, vol. 483, p. 126634, 2021.
- [79] X. Wang, J. Zhu, Y. Xu, Y. Qi, L. Zhang, H. Yang, and Z. Yi, "A novel plasmonic refractive index sensor based on gold/silicon complementary grating structure," *Chinese Physics B*, vol. 30, no. 2, p. 024207, 2021.
- [80] J. Zhu and C. Wu, "Optical refractive index sensor with fano resonance based on original mim waveguide structure," *Results in Physics*, vol. 21, p. 103858, 2021.
- [81] R. H. Sagor, M. F. Hassan, A. A. Yaseer, E. Surid, and M. I. Ahmed, "Highly sensitive refractive index sensor optimized for blood group sensing utilizing the fano resonance," *Applied Nanoscience*, vol. 11, no. 2, pp. 521–534, 2021.
- [82] T. Xu, Z. Geng, and Y. Su, "A potential plasmonic biosensor based asymmetric metal ring cavity with extremely narrow linewidth and high sensitivity," *Sensors*, vol. 21, no. 3, p. 752, 2021.
- [83] R. Al Mahmud, M. O. Faruque, and R. H. Sagor, "Plasmonic refractive index sensor based on ring-type pentagonal resonator with high sensitivity," *Plasmonics*, pp. 1–8, 2021.
- [84] K. Yee, "Numerical solution of initial boundary value problems involving maxwell's equations in isotropic media," *IEEE Transactions on antennas and propagation*, vol. 14, no. 3, pp. 302–307, 1966.
- [85] A. Taflove and S. C. Hagness, *Computational electrodynamics: the finite-difference time-domain method*. Artech house, 2005.

- [86] J.-P. Berenger, "A perfectly matched layer for the absorption of electromagnetic waves," *Journal of computational physics*, vol. 114, no. 2, pp. 185–200, 1994.
- [87] T. Weiland, "A discretization method for the solution of maxwell's equations for six-component fields.-electronics and communication,(aeü), vol. 31," 1977.
- [88] T. Weiland, "Time domain electromagnetic field computation with finite difference methods," *International Journal of Numerical Modelling: Electronic Networks, Devices and Fields*, vol. 9, no. 4, pp. 295–319, 1996.
- [89] Z. Rahimi, "The finite integration technique (fit) and the application in lithography simulations," 2011.
- [90] C. S. Desai and J. F. Abel, *Introduction to the finite element method; a numerical method for engineering analysis*. Van Nostrand Reinhold, 1971.
- [91] M. N. Sadiku, *Numerical techniques in electromagnetics with MATLAB*. CRC press, 2018.
- [92] A. D. Rakić, A. B. Djurišić, J. M. Elazar, and M. L. Majewski, "Optical properties of metallic films for vertical-cavity optoelectronic devices," *Applied optics*, vol. 37, no. 22, pp. 5271–5283, 1998.
- [93] P. R. West, S. Ishii, G. V. Naik, N. K. Emani, V. M. Shalaev, and A. Boltasseva, "Searching for better plasmonic materials," *Laser & Photonics Reviews*, vol. 4, no. 6, pp. 795–808, 2010.
- [94] G. V. Naik, J. L. Schroeder, X. Ni, A. V. Kildishev, T. D. Sands, and A. Boltasseva, "Titanium nitride as a plasmonic material for visible and near-infrared wavelengths," *Optical Materials Express*, vol. 2, no. 4, pp. 478–489, 2012.
- [95] G. Wang, C. Wang, R. Yang, W. Liu, and S. Sun, "A sensitive and stable surface plasmon resonance sensor based on monolayer protected silver film," *Sensors*, vol. 17, no. 12, p. 2777, 2017.
- [96] A. Yariv, "Universal relations for coupling of optical power between microresonators and dielectric waveguides," *Electronics letters*, vol. 36, no. 4, pp. 321–322, 2000.
- [97] Z. Zhang, J. Yang, X. He, J. Zhang, J. Huang, D. Chen, and Y. Han, "Plasmonic refractive index sensor with high figure of merit based on concentric-rings resonator," *Sensors*, vol. 18, no. 1, p. 116, 2018.

- [98] H. Emami Nejad, A. Mir, and A. Farmani, "Supersensitive and Tunable Nano-Biosensor for Cancer Detection," *IEEE Sensors Journal*, vol. 19, no. 13, pp. 4874–4881, 2019.
- [99] N. L. Kazanskii, M. A. Butt, S. A. Degtyarev, and S. N. Khonina, "Achievements in the development of plasmonic waveguide sensors for measuring the refractive index," *Computer Optics*, vol. 44, no. 3, pp. 295–318, 2020.
- [100] I. M. White and X. Fan, "On the performance quantification of resonant refractive index sensors," *Optics express*, vol. 16, no. 2, pp. 1020–1028, 2008.
- [101] Z. Chen, L. Yu, L. Wang, G. Duan, Y. Zhao, and J. Xiao, "A Refractive Index Nanosensor Based on Fano Resonance in the Plasmonic Waveguide System," *IEEE Photonics Technology Letters*, vol. 27, no. 16, pp. 1695–1698, 2015.
- [102] C. Zhang, R. Bai, X. Gu, X. R. Jin, Y. Q. Zhang, and Y. Lee, "Unidirectional reflectionless propagation in plasmonic waveguide system based on phase coupling between two stub resonators," *IEEE Photonics Journal*, vol. 9, no. 6, pp. 1–9, 2017.
- [103] S. A. Maier, *Plasmonics: fundamentals and applications*. Springer Science & Business Media, 2007.
- [104] M. Yan and M. Qiu, "Analysis of surface plasmon polariton using anisotropic finite elements," *IEEE Photonics Technology Letters*, vol. 19, no. 22, pp. 1804–1806, 2007.
- [105] W. K. Jung and K. M. Byun, "Fabrication of nanoscale plasmonic structures and their applications to photonic devices and biosensors," *Biomedical Engineering Letters*, vol. 1, no. 3, pp. 153–162, 2011.
- [106] Q. Yang, X. Liu, F. Guo, H. Bai, B. Zhang, X. Li, Y. Tan, and Z. Zhang, "Multiple Fano resonance in MIM waveguide system with cross-shaped cavity," *Optik*, vol. 220, no. April, p. 165163, 2020.
- [107] X. J. Liang, A. Q. Liu, C. S. Lim, T. C. Ayi, and P. H. Yap, "Determining refractive index of single living cell using an integrated microchip," *Sensors and Actuators, A: Physical*, vol. 133, no. 2 SPEC. ISS., pp. 349–354, 2007.
- [108] D. Mohammad and K. Behnam, "Design of a label-free photonic crystal refractive index sensor for biomedical applications," *Photonics and Nanostructures - Fundamentals and Applications*, vol. 31, no. June, pp. 89–98, 2018.

- [109] N. Ayyanar, G. Thavasi Raja, M. Sharma, and D. Sriram Kumar, “Photonic Crystal Fiber-Based Refractive Index Sensor for Early Detection of Cancer,” *IEEE Sensors Journal*, vol. 18, no. 17, pp. 7093–7099, 2018.
- [110] H. Sobral and M. Peña-Gomar, “Determination of the refractive index of glucose-ethanol-water mixtures using spectroscopic refractometry near the critical angle,” *Applied Optics*, vol. 54, no. 28, p. 8453, 2015.
- [111] R. Moreira, F. Chenlo, and A. Saint-Olympe, “Kinematic viscosity of aqueous solutions of ethanol and glucose in the range of temperatures from 20 to 45 c,” *International Journal of Food Properties*, vol. 12, no. 4, pp. 834–843, 2009.
- [112] M. A. Butt, N. L. Kazanskiy, and S. N. Khonina, “Nanodots decorated asymmetric metal-insulator-metal waveguide resonator structure based on Fano resonances for refractive index sensing application,” *Laser Physics*, vol. 30, no. 7, 2020.
- [113] Y. Tang, Z. Zhang, R. Wang, Z. Hai, C. Xue, W. Zhang, and S. Yan, “Refractive index sensor based on fano resonances in metal-insulator-metal waveguides coupled with resonators,” *Sensors (Switzerland)*, vol. 17, no. 4, 2017.
- [114] C. T. C. Chao, Y. F. C. Chau, H. J. Huang, N. T. Kumara, M. R. R. Kooh, C. M. Lim, and H. P. Chiang, “Highly sensitive and tunable plasmonic sensor based on a nanoring resonator with silver nanorods,” *Nanomaterials*, vol. 10, no. 7, pp. 1–14, 2020.
- [115] S. W. Lee, K. S. Lee, J. Ahn, J. J. Lee, M. G. Kim, and Y. B. Shin, “Highly sensitive biosensing using arrays of plasmonic Au nanodisks realized by nanoimprint lithography,” *ACS Nano*, vol. 5, no. 2, pp. 897–904, 2011.
- [116] P. Li, Z. Jia, X. Lü, Y. Liu, X. Ning, J. Mo, and J. Wang, “Spectrometer-free biological detection method using porous silicon microcavity devices,” *Optics Express*, vol. 23, no. 19, p. 24626, 2015.
- [117] K. S. Kunz and R. J. Luebbers, *The Finite Difference Time Domain Method for Electromagnetics*. CRC Press, 1993.
- [118] H. Gai, J. Wang, and Q. Tian, “Modified debye model parameters of metals applicable for broadband calculations,” *Applied optics*, vol. 46, no. 12, pp. 2229–2233, 2007.
- [119] R. H. Sagor, M. F. Hassan, A. A. Yaseer, E. Surid, and M. I. Ahmed, “Highly sensitive refractive index sensor optimized for blood group sensing utilizing the

- Fano resonance,” *Applied Nanoscience (Switzerland)*, vol. 11, no. 2, pp. 521–534, 2021.
- [120] M. Butt, S. Khonina, and N. Kazanskiy, “Metal-insulator-metal nano square ring resonator for gas sensing applications,” *Waves in Random and complex media*, pp. 1–11, 2019.
- [121] S. Y. Chou, P. R. Krauss, and P. J. Renstrom, “Nanoimprint lithography,” *Journal of Vacuum Science & Technology B: Microelectronics and Nanometer Structures Processing, Measurement, and Phenomena*, vol. 14, no. 6, pp. 4129–4133, 1996.
- [122] L. E. Murdoch, K. McKenzie, M. Maclean, S. J. MacGregor, and J. G. Anderson, “Lethal effects of high-intensity violet 405-nm light on *Saccharomyces cerevisiae*, *Candida albicans*, and on dormant and germinating spores of *Aspergillus niger*,” *Fungal Biology*, vol. 117, no. 7-8, pp. 519–527, 2013.
- [123] A. D. N. Lago, W. D. R. Ferreira, and G. S. Furtado, “Dental bleaching with the use of violet light only: Reality or Future?,” *Photodiagnosis and Photodynamic Therapy*, vol. 17, pp. 124–126, 2017.
- [124] S. Mimasaka, T. Oshima, and M. Ohtani, “Visualization of old bruises in children: Use of violet light to record long-term bruises,” *Forensic Science International*, vol. 282, pp. 74–78, 2018.
- [125] C. Ballardin, C. L. Pereira-Stabile, and G. A. V. Stabile, “Use of a generic violet light in the surgical management of medication-related osteonecrosis of the jaws: a technical note,” *Oral and Maxillofacial Surgery*, vol. 22, no. 4, pp. 477–481, 2018.
- [126] M. A. Butt, N. L. Kazanskiy, and S. N. Khonina, “Highly Sensitive Refractive Index Sensor Based on Plasmonic Bow Tie Configuration,” *Photonic Sensors*, vol. 10, no. 3, pp. 223–232, 2020.
- [127] C. Li, S. Li, Y. Wang, R. Jiao, L. Wang, and L. Yu, “Multiple fano resonances based on plasmonic resonator system with end-coupled cavities for high-performance nanosensor,” *IEEE Photonics Journal*, vol. 9, no. 6, pp. 1–9, 2017.
- [128] Y. Wang, S. Li, Y. Zhang, and L. Yu, “Ultrasharp fano resonances based on the circular cavity optimized by a metallic nanodisk,” *IEEE Photonics Journal*, vol. 8, no. 6, pp. 1–8, 2016.

- [129] S. Yu, T. Zhao, J. Yu, and D. Pan, “Tuning multiple fano resonances for on-chip sensors in a plasmonic system,” *Sensors*, vol. 19, no. 7, p. 1559, 2019.
- [130] M. Rahmatiyar, M. Afsahi, and M. Danaie, “Design of a refractive index plasmonic sensor based on a ring resonator coupled to a mim waveguide containing tapered defects,” *Plasmonics*, vol. 15, no. 6, pp. 2169–2176, 2020.

List of Publications

Journal

1. Infiter Tathfif, Md. Farhad Hassan, Kazi Sharmeen Rashid, Ahmad Azuad Yaseer, and Rakibul Hasan Sagor, "**Hypersensitive and Optimized Plasmonic Refractive Index Sensor for Cancer Biomarker and Chemical Concentration Detection,**" in *The European Physical Journal Plus*, 2021.
[Under Review]
2. Kazi Sharmeen Rashid, Md. Farhad Hassan, Ahmad Azuad Yaseer, Infiter Tathfif, and Rakibul Hasan Sagor, "**Label-free Detection of Biomaterial Employing Multiple Rings Structured Plasmonic Nanosensor,**" in *Sensing and Bio-Sensing Research*, 2021.
[Under Review]
3. Ahmad Azuad Yaseer, Md. Farhad Hassan, Infiter Tathfif, Kazi Sharmeen Rashid, and Rakibul Hasan Sagor, "**Plasmonic Refractive Index Sensor Optimized for Color Detection,**" in *IEEE Sensors Journal*, 2021.
[Under Review]